# Surface spots on cool giant stars probed by spectro-astrometry

Dissertation
zur Erlangung des Doktorgrades
des Departments Physik
der Universität Hamburg

vorgelegt von
Boris Voigt
aus Neuwied

Hamburg
2009

# Abstract

Spectro-astrometry is a technique to obtain information about the structure of an astronomical source on sub-diffraction limited spatial scales down to milli- or micro-arcseconds. The method exploits the shift of the photocentre of a structured source over emission/absorption lines in its spectral energy distribution. Sub-diffraction limited resolution can be achieved because the method only uses wavelength-differential information of longslit spectra. Although spectro-astrometry has already been devised by Bailey (1998) and some studies have been performed to date on different astronomic targets, so far, no systematic analysis of the potential of this technique has been undertaken.

The aim of this work was to analyse the potential of the method, develop the tools to exploit this potential and write the software which is needed to perform the analysis procedure. To verify the practical feasibility, observations were done with the VLT/CRIRES facility to demonstrate the capabilities of the method with respect to detecting structures on giant star surfaces. All steps of data reduction were analysed with respect to their influence on the spectro-astrometric quantities and a new method for bad pixel detection was devised and implemented. A tool to simulate the spectro-astrometric signatures of arbitrary source configurations was created and coded and allows to deduce the source configuration from observed data. It was found that for real data instrumental artefacts are a major problem. These artefacts originate from asymmetric point-spread-functions which can be caused by instrumental characteristics and/or adaptive optics. Since the artefacts can exceed the target-induced signatures in amplitude and, hence, mask them, the removal of such artefacts turned out to be the most important step of this work. An algorithm to remove, or at least reduce, the artefacts was devised. It assumes that any instrumental effect can be condensed into an effective, asymmetric PSF. The choice of the correct parameterisation for the PSF proved to be the critical point in this procedure. When applied to real data, the removal process significantly reduces the artefacts. Observations of the two giant stars TW Oph and RS Vir were planned and executed. Upper limits on spot coverage were estimated for RS Vir: a cool spot covering $10\,\%$ of the visible disk with a temperature contrast of $500\,\mathrm{K}$ is right at the detection limit. In contrast, target-induced signatures were detected in the spectro-astrometric quantities of the TW Oph data. The best-fitting scenario is a single cool spot at mid-latitudes with a temperature contrast of $500\,\mathrm{K}$ covering $11\,\%$ of the visible disk. However, the principle of spectro-astrometry and observational constraints result in a degeneracy of the best-fitting scenario. This means that, to some degree, other spot parameters fit the observations equally. The process of finding the correct source structure to fit the observations was found to strongly depend on the availability of precise synthetic spectra. Uncertainties in such model spectra directly translate into the deduced source configuration. The technique of spectro-astrometry has a performance similar to interferometry but does not require as much telescope time as multiple-telescope interferometers. Spectro-astrometry will profit directly from larger telescopes and the next generation of adaptive optics, and hence will remain competitive to other techniques in the future.

# Zusammenfassung

Spektroastrometrie ermöglicht es, die Struktur von astronomischen Objekten auf Skalen unterhalb der Beugungsbegrenzung einer Teleskopoptik zu untersuchen. Es können mit dieser Methode und modernen Teleskopen räumliche Auflösungen von Milli- oder sogar Mikrobogensekunden erreicht werden. Spektroastrometrie nutzt die Tatsache, dass sich das räumliche Maximum der Helligkeitsverteilung einer strukturierten Quelle mit der Wellenlänge verschiebt, wenn das Spektrum der Quelle Emissions- oder Absorptionslinien aufweist. Eine Auflösung unterhalb der Beugungsbegrenzung kann erreicht werden, weil nur die relative räumliche Änderung des Helligkeitsmaximums eines Langspaltspektrums mit der Wellenlänge relevant ist, nicht aber die absolute Position. Obwohl diese Methode bereits von Beckers (1982) entwickelt wurde und es seitdem Veröffentlichungen über Studien verschiedener Objekte gab, existieren bisher noch keine systematischen Untersuchungen zu den Problemen und dem Potential der Methode.

Das Ziel dieser Arbeit ist eine grundlegende Analyse der Spektroastrometrie sowie ihre Anwendung zwecks Untersuchung von Riesensternen auf Oberflächenstrukturen mittels Beobachtungen mit VLT/CRIRES. Hierzu mussten die meisten Analyse-, Simulations- und Datenreduktionsmethoden entwickelt und programmiert werden. Sämtliche Schritte der Datenreduktion wurden auf ihren Einfluss auf die spektroastrometrischen Größen untersucht, um so ein optimales Reduktionsverfahren zu erstellen. Ein Algorithmus zur Simulation der spektroastrometrischen Signaturen von beliebigen Objektkonfigurationen wurde entwickelt und implementiert. Mit seiner Hilfe können die notwendigen Simulationen durchgeführt werden, um Objektstrukturen aus Beobachtungsdaten abzuleiten. Instrumentelle Artefakte in den spektroastrometrischen Größen stellen das Hauptproblem beim erreichen der theoretisch möglichen räumlichen Auflösung dar. Diese Artefakte werden durch das Instrument selbst und/oder durch eine eventuell benutzte adaptive Optik verursacht; sie können durch eine asymmetrische Punktverbreiterungsfunktion (PSF) beschrieben werden. Die Entfernung bzw. Reduzierung jener Artefakte ist notwendig, weil ihre Amplituden weit über denjenigen der objektinhärenten Signaturen liegen können. Ein Verfahren wurde entwickelt, um eine solche Reduzierung zu verwirklichen. Es basiert auf der Annahme, dass alle instrumentellen Einflüsse durch eine effektive, asymmetrische PSF beschrieben werden können. Es stellte sich heraus, dass eine optimale Parameterisierung der PSF entscheidend für den Erfolg des Verfahrens ist. Die Anwendung des Algorithmusses auf Beobachtungsdaten führte zu einer signifikanten Verringerung der Artefakte. Beobachtungen der Riesensterne TW Oph und RS Vir wurden geplant und durchgeführt. Während auf RS Vir keine Oberflächenstrukturen nachgewiesen werden konnten, zeigen die spektroastrometrischen Größen bei TW Oph eindeutige Signaturen. Letztere lassen sich am besten durch einem einzelnen, kühlen Fleck mit einem Temperaturkontrast von $500\,K$ und einem Bedeckungsfaktor von $11\,\%$ erklären. Sowohl die Methode der Spektroastrometrie selbst als auch Restriktionen bei den Beobachtungen führten dazu, dass mehrere Fleckenkonfigurationen gleichermaßen die Beobachtungen erklären können. Die Modellierung der Beobachtungsdaten mittels Fleckenmodellen hängt stark von den hierzu benutzten synthetischen Spektren ab, weshalb genaue Modellspektren unerlässlich sind. Spektroastrometrie kann im Infraroten Ergebnisse erzielen, welche vergleichbar sind mit denen der aktuellen Mehrteleskopinterferometer, mit dem Vorteil, dass weniger Gesamtbeobachtungszeit benötigt wird. Die Methode der Spektroastrometrie wird von zukünftigen Entwicklungen im Bereich der adaptiven Optik und von steigenden Teleskopdurchmessern direkt profitieren, und ist damit auch künftig konkurrenzfähig.

# Contents

# Chapter 1

# Introduction

Most astronomical objects in the universe have huge distances to the Earth. Even though many of these celestial bodies are large compared to the Earth, their apparent spatial scales are often tiny. Thus, astronomers ever seek to develop larger telescopes and to devise new techniques to resolve ever smaller spatial scales. High spatial resolution indeed yields new knowledge on subjects which are so far not, or only partly, understood. One of the numerous topics which will profit from increased spatial resolution is stellar structure and evolution. Conventional full-disk spectroscopy only allows to deduce information about the *vertical* temperature structure of a star. In cool, extended stellar atmospheres, dynamical processes take place which require the *horizontal* temperature structure to be known in order to be fully understood. These dynamical phenomena include giant convection cells, magnetically induced spots, mass loss and dust formation. The horizontal structure is very difficult to study as the spatial scales are of the order of few milli-arcseconds for the stars with the largest apparent diameters. This work studies in detail the method of spectro-astronomy which aims at sub-diffraction-limited spatial resolution. Using large telescopes, this corresponds to a spatial resolution of the order of one milli-arcsecond.

This work is structured as follows:

Chapter 1 gives an introduction to several topics which are of relevance for this thesis, see below. Because of its importance for this thesis, a detailed discussion of the technique of spectro-astrometry is presented in a separate chapter, namely Chapter 2. There, the basics are discussed as well as the method to simulate spectro-astrometric signatures of arbitrary object configurations and the method to remove instrumental artefacts in order to exploit the full potential of spectro-astrometry. Chapter 3 deals with the data reduction steps which are important for later spectro-astrometric analysis. Each of the reduction steps is analysed with respect to possible influences on the spectro-astrometric quantities. The spectro-astrometric analysis of the giant star data set on TW Oph and RS Vir and the data on $\alpha$ Centauri A is given in Chapter 4. A summary on the achievements of this work and an outlook on the future perspectives of spectro-astrometry follow in the last chapter 5.

This introduction is organised in several parts: diffraction and interference of light are fundamental to understanding spectroscopy and allow to deduce the spatial resolution limit of a telescope (Sect. 1.1). Adaptive optics are introduced in Sect. 1.2, as they achieve to reach the diffraction-limited resolution of ground-based telescopes and directly improve the spatial resolution attainable with spectro-astrometry. The data sets used in this thesis were obtained with the CRIRES spectrograph, which is, therefore, described in Sect. 1.3. The interior structure and energy generation of (giant) stars is summarised in Sect. 1.4, and molecular physics, which, e.g., explain the absorption levels of molecules,

is the subject of Sect. 1.5. Section 1.6 of this chapter deals with the stellar atmosphere code used to obtain the synthetic spectra used in this work. Interferometry and lunar occultations as alternative methods to perform high resolution observations are shortly discussed in Sects. 1.8 and 1.7.

## 1.1   Diffraction

In this section, a short explanation of the processes of interference and diffraction is given as both phenomena are fundamental to telescope optics and spectroscopy. Therefore, they are also important for spectro-astrometry. A more detailed treatment of these subjects can be found in many physics textbooks, e.g., Demtröder (1999). First, diffraction at a single slit is considered. Parallel light is assumed to fall onto a slit of width $w$. Every point inside the slit is the origin of a new spherical wave. These waves interfere with each other. If the slit is divided into $N$ equally spaced sources with distance $d$ (i.e., $N = w/d$), the intensity at an angle of $\Theta$ is to be evaluated in the following. The path difference between two neighbouring waves is $\Delta s = d \cdot \sin\Theta$, leading to a phase difference of

$$\Delta\phi = 2\pi/\lambda \cdot \Delta s, \tag{1.1}$$

where $\lambda$ is the wavelength of the light and $s$ the path length. The electric field vector of a plain light wave can be described by

$$\mathbf{E} = \mathbf{E_0} \cdot e^{i(\omega t + \phi)}, \tag{1.2}$$

where $\omega$ is the angular frequency and $\phi$ is the phase. The total amplitude of the $N$ interfering spherical waves of equal amplitude can be expressed by

$$E = A \cdot e^{i\omega t} \sum_{j=1}^{N} e^{i(j-1)\Delta\phi}, \tag{1.3}$$

if the phase of the first wave is set to zero. The geometrical series can be written as

$$\sum_{j=1}^{N} e^{i(j-1)\Delta\phi} = \frac{e^{iN\Delta\phi - 1}}{e^{i\Delta\phi - 1}}. \tag{1.4}$$

Performing a simple conversion and using the complex representation of the sine as well as the intensity $I = c\epsilon_0 |E|^2$ and Eq. (1.1), one obtains

$$I(\Theta) = \frac{I_0}{N^2} \cdot \frac{\sin^2\left(\pi(w/\lambda)\sin\Theta\right)}{\sin^2\left(\pi(d/\lambda)\sin\Theta\right)}. \tag{1.5}$$

Defining $x = \pi(w/\lambda) \cdot \sin\Theta$ yields

$$I(\Theta) = \frac{I_0}{N^2} \frac{\sin^2 x}{\sin^2(x/N)}. \tag{1.6}$$

To represent realistic circumstances, $N$ has to be considered to approach infinity which is equivalent to $d \to 0$. As, in this case, $\sin^2(x/N) \to x^2/N^2$, one obtains

$$\lim_{N \to \infty} I(\Theta) = I_0 \cdot \frac{\sin^2 x}{x^2}. \tag{1.7}$$

This intensity distribution is the commonly known diffraction pattern caused by a single slit. This kind of diffraction will turn out, see below, to be a special case of general diffraction theory for large distances from the slit. This special case is called Fraunhofer diffraction. If a plain wave in three dimensions falls orthogonally onto a circular aperture with radius $R$, a rotational-symmetric intensity distribution is observed. General diffraction theory, cf. Eq. (1.17), allows to evaluate this case and leads to an intensity distribution of

$$I(\Theta) = I_0 \cdot \left( \frac{2J_1(x)}{x} \right)^2, \tag{1.8}$$

with $x = 2\pi R/\lambda \cdot \sin \Theta$ and $J_1(x)$ being the first order Bessel function.

Now, a diffraction grating is considered. A grating can be imagined to consist of $M$ adjoining, parallel slits with spacing $a$. Thus, the intensity distribution behind this configuration is determined by two contributions; first, the interference of the light beams from each of the slits and second, the diffraction pattern caused by each individual slit:

$$I(\Theta) = I_0 \cdot \frac{\sin^2 \left( \pi(w/\lambda) \sin \Theta \right)}{(\pi(w/\lambda) \sin \Theta)^2} \cdot \frac{\sin^2 \left( M\pi(a/\lambda) \sin \Theta \right)}{\sin^2 \left( \pi(a/\lambda) \sin \Theta \right)}. \tag{1.9}$$

Figure 1.1 illustrates the intensity distribution for eight slits and $a = 2 \cdot w$. If the path
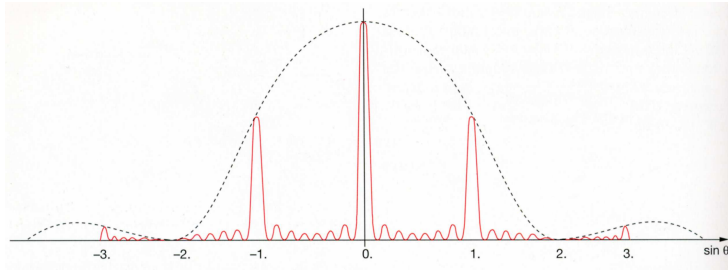


Figure 1.1: Intensity distribution for a grating consisting of eight slits with $a = 2 \cdot w$, according to Eq. 1.9; the interference orders are shown on the x-axis; the diffraction envelope is also plotted.

difference for light beams of adjacent slits is a multiple of the wavelength $\lambda$, the intensity distribution will have a local maximum. This is true for $\Delta s = a \cdot \sin \Theta = m\lambda$. As there are also gratings which have inclined grooves, the so-called *blazed* gratings, two new angles are introduced here which are measured versus the normal to the grating base. They denote the angle of incoming and reflected light, $\alpha$ and $\beta$, respectively. In contrast, $\Theta$ is the angle of incidence measured with respect to the normal to the groove. It is straightforward to see that constructive interference can only be achieved if the path difference satisfies

$$\Delta s = a(\sin \alpha + \sin \beta) = m\lambda, \tag{1.10}$$

where $m$ is the diffraction order. Equation (1.10) is called the (in-plane) grating equation. A spectrograph disperses incoming light spectrally and can be used to analyse the intensity distribution over wavelength. A typical setup for a grating spectrograph is shown in Fig. 1.2. In principle, the slit is imaged onto the detector. The light is dispersed by the grating and, hence, a spectrum can be observed in the detector plane. The spectrum consists of slit images for each wavelength. These images are detected at different coordinates depending on their wavelength because of the dispersion induced by the grating. The wavelength range which is imaged to the detector plane can be adjusted by rotating the grating. Observing at high diffraction orders requires blazed gratings because for normal

Figure 1.2: Setup of a grating spectrograph: the entrance slit $S_1$, the reflective grating and the photon detector are the most important elements.

gratings, the intensity steeply decreases with increasing diffraction order. The inclination of the grooves with respect to the grating normal shifts the maximum intensity to a higher diffraction order. These grating are also called *echelle* gratings.

Starting with the grating equation, Eq. (1.10), the angular dispersion of a grating is obtained as
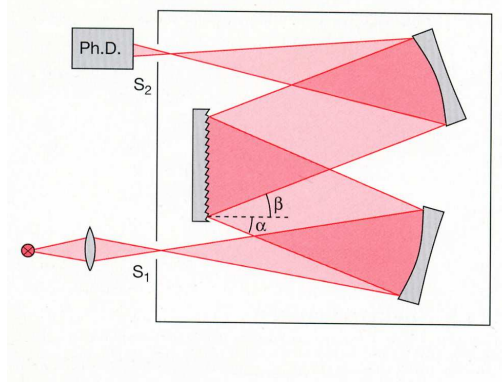
$$\frac{\mathrm{d}\beta}{\mathrm{d}\lambda} = \frac{m}{a \cdot \cos\beta} = \left( \frac{a^2 \cos^2\alpha}{m^2} + \frac{2a\lambda}{m}\sin\alpha - \lambda^2 \right)^{-1/2}. \tag{1.11}$$

The larger the angular dispersion, the larger the spatial distance of two wavelengths $\lambda_1$ and $\lambda_2$. The angular dispersion is determined by the grating constant, the wavelength, the angle of incidence and the order of diffraction. Depending on the effective width of the entering light beam, a number of grating grooves $M' \leq M$ is illuminated. The exit pupil then is $e = M' \cdot a \cdot \cos\beta$. According to the Rayleigh criterion, cf. Sect. 1.1.1, the difference angle $\Delta\beta$ between the propagation directions of the two diffracted waves with $\lambda_1$ and $\lambda_2 = \lambda_1 + \Delta\lambda$ has to be larger than half the angular width $\Delta\beta_{\min} = \lambda/e$. Using Eq. (1.11) yields

$$\Delta\lambda = \frac{d \cdot \cos\beta}{m}\Delta\beta \geq \frac{d \cdot \cos\beta}{m}\Delta\beta_{\min} \geq \frac{\lambda}{m \cdot M}. \tag{1.12}$$

Hence, the spectral resolution is

$$R = \frac{\lambda}{\Delta\lambda} \leq m \cdot M. \tag{1.13}$$

If the spectrograph is attached to a telescope, the parameters $m$ and $M$ cannot be varied independently. If the telescope diameter is denoted with $D$ and the minimum distance of two resolvable point sources $\phi$, one can show that the spectral resolution limit of the telescope-spectrograph system is

$$R = \frac{\lambda}{\Delta\lambda} \leq m \cdot M \cdot \frac{\lambda}{D\phi}. \tag{1.14}$$

Coming back to diffraction, an arbitrary two-dimensional aperture is now assumed at a coordinate of $z = 0$, i.e., within the x-y-plane. A point light source is placed at $(0, 0, -z_l)$. Then, the field amplitude in the plane $z = 0$ is

$$E_P = \frac{A}{R} \cdot e^{\mathrm{i}(\omega t - kR)}. \tag{1.15}$$

where $A$ is the initial amplitude and $R$ is the distance of a point within the plane to the light source. Each infinitesimal area $\mathrm{d}\sigma(x, y)$ in the plane is a source of a secondary

spherical wave. At the point Q$(x', y')$, the field strength contribution of this element of area can be shown to be

$$\mathrm{d}E_Q = \cos \Theta / (\mathrm{i}\lambda) \cdot \frac{E_P \cdot \mathrm{d}\sigma}{r} \, e^{-\mathrm{i}kr}. \tag{1.16}$$

This leads to a total field amplitude at Q of

$$E_Q = \int \int \frac{\cos \Theta}{\mathrm{i}\lambda} \cdot E_P \frac{e^{\mathrm{i}kr}}{r} \, \mathrm{d}x \, \mathrm{d}y. \tag{1.17}$$

The area integral is done over all elements of area covering the aperture. The integral in Eq. (1.17) is called the Fresnel-Kirchhoff diffraction integral. If Q is close to the aperture, the diffraction pattern will closely resemble those of Fresnel-diffraction. If Q is far away from the aperture, Fraunhofer-diffraction results. With Eq. (1.17), in principle, diffraction can be calculated for arbitrary configurations. However, in most cases, these calculations can only be done numerically. One example of the Fresnel-Kirchhoff diffraction is now shown: diffraction at a straight edge, which will be useful for lunar occultation theory, cf. Sect. 1.7. It shall be assumed that parallel light falls orthogonally onto a straight edge which resides in the x-y-plane at $x < 0$, $z = 0$. The corresponding intensity distribution is depicted in Fig. 1.3. Because of diffraction, the light intensity is larger than zero for
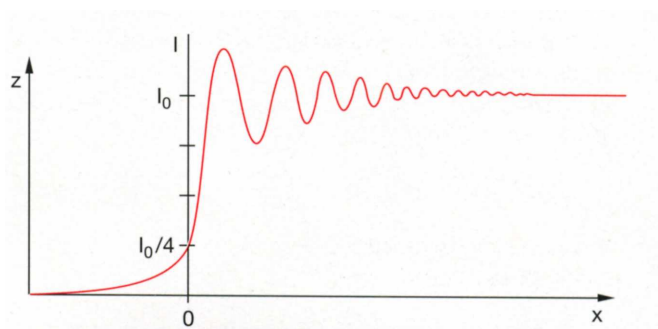


Figure 1.3: Diffraction pattern observed behind a straight edge for orthogonally incoming, parallel light.

$x < 0$ and oscillates for $x > 0$ with $x' \ll z_0$ if the observer is at Q$(x', z_0)$. This situation can be explained with the general diffraction integral which now is

$$E(Q) = \frac{\cos \Theta}{\mathrm{i}\lambda} \cdot E_P \int_0^\infty \frac{e^{\mathrm{i}k\sqrt{(x-x')^2+z_0^2}}}{\sqrt{(x - x')^2 + z_0^2}} \, \mathrm{d}x, \tag{1.18}$$

which can be approximated by a series expansion of the square root for $x' \ll z_0$. The lengthy calculation is not given here. However, it is interesting to note that the wavelength of the incoming light $\lambda$, the distance from the edge to the observer $z_0$ and the distance $x'$ are related by

$$x_\mathrm{f} = \sqrt{\lambda \cdot z_0}. \tag{1.19}$$

Here, $x_\mathrm{f}$ is the spacing of the fringes of the diffraction pattern observed in Q$(x', z_0)$.

### 1.1.1   Spatial resolution limits of telescopes

As the distance of any star, save the Sun to the Earth, is very large, stars can be assumed to be point sources for the discussion of the spatial resolution limit of telescopes[1]. The

---

[1] Of course, if the spatial resolution limit is comparable or even better than the apparent diameter of a star, this is no longer justified, as e.g., in the case of spectro-astrometry.

light of a distant point source can be described by a plane wave. Because of the diffraction of the telescope lens/mirror, the image of such a source in the focal plane is not point-like but obeys the intensity distribution of Eq. (1.8) for any one-dimensional, central cut through the light pattern. Figure 1.4 illustrates the intensity distribution of two close-by point sources in the focal plane. The diameter of the central diffraction maximum $d_{\mathrm{diff}}$ is
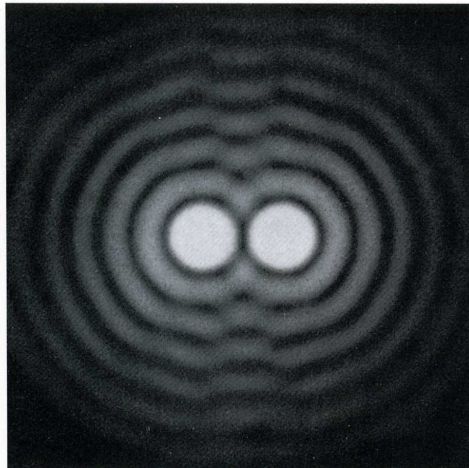


Figure 1.4: Intensity distribution of the light of two close-by point sources after passing a circular aperture.

equal to two times the position of the first null of the Bessel function

$$d_{\mathrm{diff}} = 2f_1 \cdot \sin \alpha_B \approx 2.44 \cdot f_1 \lambda/D, \qquad (1.20)$$

where $f_1$ is the focal length of the telescope. The Rayleigh criterion defines two point sources to be resolvable if the central intensity maximum of one source is at least as far away from the central maximum of the other source as the first minimum. As the first minimum is at an angular separation of

$$\delta_{min} = 1.22 \cdot \lambda/D, \qquad (1.21)$$

this is also the spatial resolution limit of the telescope according to the Rayleigh criterion. For the VLT (8.2 m diameter), this translates into a diffraction-limited resolution of 69 milli-arcseconds (mas) for a wavelength of $2.3\,\mu$m. However, fluctuations of the refractory index of the atmosphere of the Earth limit the actual spatial resolution for ground-based observations to about one arc-second. This limiting effect on spatial resolution is called *seeing* whereas the varying intensity due to the fluctuations is called *scintillation*. The seeing varies on short time scales of seconds and is different on average for different observing sites. On average, the higher the altitude of an observing site, the better is the seeing. For point sources, the wavefront of the incoming light is plain before it reaches the atmosphere. The atmospheric fluctuations deform the wavefront irregularly. As the shape of the deformed wavefront changes on very short time scales, quickly varying images are caused in the focal plane of the telescope. If an exposure is taken with integration times much longer than the atmospheric coherence time, a seeing-broadened disk is observed. The average seeing at the VLT-Paranal site is about $0.8''$. The time scale of atmospheric fluctuations is about one milli-second (ms) but can strongly vary. The place on Earth with the potentially best observing conditions which is accessible at reasonable effort is Dome C in Antarctica with an average seeing of $0.27''$ and a coherence time of $7.9\,$ms,

cf. Lawrence et al. (2004). Hence, exposures obtained at integration times of less than this time scale do yield diffraction-limited resolution. This is indeed the idea of the novel observing technique which is called *Lucky imaging*. It has recently been demonstrated to yield excellent results, cf. Law et al. (2006).

## 1.2 Adaptive Optics

As the atmospheric seeing dramatically reduces the spatial resolution attainable with modern large telescopes, various techniques have been devised to circumvent this problem. One of these methods is adaptive optics. The advantage of this technique is that directly reduces the width of the point spread function of the light and, thus, other techniques profit from this increased resolution. Spectro-astrometry also directly profits from this. The basic idea behind adaptive optics is that if the shape of the deformed wavefronts of the incoming light were known one could try to correct them to restore the diffraction-limited spatial resolution. Probably the first scientist who published this idea was Babcock (1953). Because the technical requirements could not be met at that time, it took many years before the first adaptive optics system actually worked. The first system working at an ESO telescope was the *Come-On* at the 3.6 m telescope on La Silla, see ESO press releases 06/89 and 05/90.

Part of the light beam coming from the telescope is directed onto the *wavefront sensor*. This device detects the shape of the wavefront. One kind of wavefront sensor is the Hartmann-Shack sensor, Shack and Platt (1971). It consists of multiple lenslets which map the light beam onto several detector pixels. The wavefront deformation is calculated by the spatial deviation of the light spots from reference points. Other types of wavefront sensors determine the curvature of the wavefront: for each lenslet or equivalent sub-unit of the light beam, the intra- and extra-focal intensity is determined. From the change of these intensities over the sub-units, the wavefront curvature can be deduced. The detection and correction of the actual shape of the wavefront has to be performed in realtime, i.e., in time intervals shorter than the atmospheric coherence time scale. The next step then is to correct the wavefront with the information from the sensor. The correction is often performed using a deformable mirror. The computer calculates how this mirror needs to be deformed in order to compensate for the atmospheric influence. Wavefront correction can only work if a sufficiently bright light source is present in the field of view. The quality of wavefront correction is best at the position of this reference light source and decreases steeply with increasing distance to the reference source. Thus, it is optimal if the target is bright enough to serve as wavefront sensing source. If the target is too weak, another bright source which is close to the target may be used as a wavefront sensing source. The closer this source is to the target, the better the wavefront correction at the position of the target. When observing extended sources, the quality of correction changes over the area of the source. In order to guarantee a wavefront correction even if no bright reference star is present in the field of view, a Laser guide star can be used with some modern adaptive optics systems. There are two kinds of Lasers used for this: a sodium Laser is pointed to the desired sky area and excites sodium atoms in the mesosphere at about an altitude of 80–90 km. The sodium atoms re-emit at the same 589.2 nm wavelength and create an artificial star. Alternatively, other Lasers may be used to exploit Rayleigh scattering in the lower atmosphere at heights of about 15–25 km. The scattered light is then used as a reference source. However, because of the larger altitude, sodium Laser guide stars allow for a better wavefront correction but are more expensive. The next generation of adaptive optics, i.e., multi-conjugated adaptive optics, will increase the field of view which has optimal correction. This will be achieved by using multiple systems of

deformable mirrors, wavefront sensors and Laser guide stars. A typical number to quantify the performance of an optical system is the *Strehl* number. It is the ratio of the measured peak intensity in the focal plane to the theoretically expected peak intensity. Hence, a Strehl number of one would indicate a perfect performance.

The VLT/CRIRES instrument has been used to obtain the data sets presented in this thesis. The adaptive optics system MACAO[2] performs the wave front correction before the light beam enters the spectrograph, cf. Paufique et al. (2004) for details. MACAO uses a deformable mirror with 60 actuators. An actuator is a mechanical device which allows to change the shape of the mirror. Wavefront sensing is performed in the R-band, independently from the wavelength range of observations. The sensor is of the wavefront curvature type. No laser guide star is available for MACAO. The Strehl ratio states the fraction of the total light which passes through the slit and depends on the atmospheric seeing conditions. The Strehl ratio has been simulated by Paufique et al. (2004) for the instrument in relation to the seeing conditions and the V-band magnitude of the wavefront reference star, cf. Fig. 1.5. The graph shows that a seeing of better than 1.1″ is required
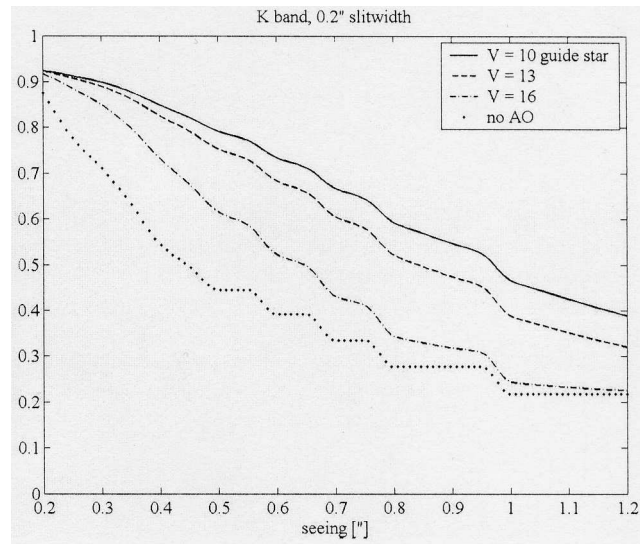


Figure 1.5: Simulated Strehl ratio for the CRIRES instrument in the K-band. The graph shows the Strehl ratio over the seeing width for different V-band source brightness. Figure from Paufique et al. (2004).

for adaptive optics to improve spatial resolution. For the giant data set used in this work, the targets are very bright. Hence, the performance is expected to be optimal if the seeing is good. The average seeing over the whole data set is 0.87″, cf. Chap. 3. Another way to measure the performance of the adaptive optics is to consider the width of the spatial profile of a point source in the longslit spectrum. The width directly yields the effective width of the PSF after correction. The spatial profile widths are reported in the data reduction chapter. The average profile width turns out to be 0.28 mas, which is far better than the average seeing value. The latter is determined via the atmospheric seeing monitor. Thus, adaptive optics significantly improved the spatial resolution.

Under very good atmospheric conditions, the adaptive optics system at the VLT almost reaches the diffraction limit, compare, e.g., Laverny and Mékarnia (2004) who achieved 70 mas spatial resolution with VLT/NACO at 2.0 μm. This resolution by far does not

---

[2]Multi-Applications Curvature Adaptive Optics

suffice to directly detect surface structure on giant stars. However, the advantage of adaptive optics is that it directly increases the spatial resolution attainable with spectro-astrometry, cf. Sect. 2.4.

Under optimal conditions, the use of adaptive optics at a large telescope allows to resolve the largest supergiants in the ultra-violet. Because of the wavelength dependence of the diffraction limit, cf. Eq. (1.21), the spatial resolution limit of a VLT at 350 nm is about 10 mas. As the apparent size of supergiants can be larger in the UV compared to the IR, at least a partial resolution would be possible. For instance, Betelgeuse has been found to have an UV-diameter of about 100 mas and could be resolved with the Hubble Space Telescope (Gilliland and Dupree, 1996) which has a primary mirror with a diameter of only 2.4 m. The advantage of a space-based telescope of course is that the diffraction-limited resolution is always guaranteed and that wavelengths shorter than 300 nm are accessible[3]. However, direct imaging of the largest supergiants with next generation telescopes and adaptive optics should be possible.

## 1.3 The CRIRES instrument

CRIRES is the cryogenic high-resolution IR echelle spectrograph. It has been used to obtain the data presented in this thesis. Detailed information about this instrument can be found in the ESO CRIRES user manual, Siebenmorgen and Smette (2008). Here, a short summary is given. CRIRES is a longslit ($31''$) spectrograph which operates in the near-infrared and covers a large wavelength range of $0.95\mu$m $- 5.4\mu$m. The sampling of the spatial direction is 86 mas per detector pixel. A spectral resolution of $R = 100,000$ can be achieved using a slit width of $0.2''$. The instrument is located at the Nasmyth A focus of VLT/UT1. It can be operated in combination with the MACAO adaptive optics system. The optical setup is illustrated in Fig. 1.6. The instrument setup consists of a warm part which operates at ambient temperatures and of a cold part which is cooled down to 65 K. The latter is marked in the figure by a light grey shading. The light coming from the telescope first enters a calibration unit which is not shown in the figure. In this unit, a Halogen lamp may be placed for creating flatfield images, or gas-cells can be placed within the light beam for precise wavelength calibration and precise determination of the instrumental profile. The derotator enables the observer to determine the orientation of the field of view in relation to the spectrograph. This is particularly important for spectro-astrometry. Before the light enters the cool part of CRIRES, it passes the adaptive optics system, i.e., the 60-actuator deformable mirror and the wavefront sensor. The sensor is equipped with an array of 60 lenslets. The light is imaged through 60 fibre optics from the lenslets onto 60 avalanche photo-diodes (APD). This is guaranteed by optionally inserting neutral density filters into the light beam. The APD saturation-limit also restricts the maximum brightness of any target in case adaptive optics is to be used in combination with CRIRES. In order to avoid thermal influences, the spectrograph itself is placed in an evacuated box and is cooled down to 70 K. The detectors are kept at 25 K with temperature stabilisation at a level of 0.1 K. After entering the cryogenic part, the light is pre-dispersed by a prism in order to increase the separation of different diffraction orders. An intermediate slit is placed in the light path after the prism to select a single order which then enters into the high-resolution spectrograph. An echelle grating measuring 40 times 20 cm with 31.6 lines/mm and a blaze angle of $63.5°$ performs the light dispersion. The light is finally focused onto the four-CMOS-detector array. The focal plane is covered

---

[3]The Earth's atmosphere absorbs any light with $\lambda < 290$ nm.
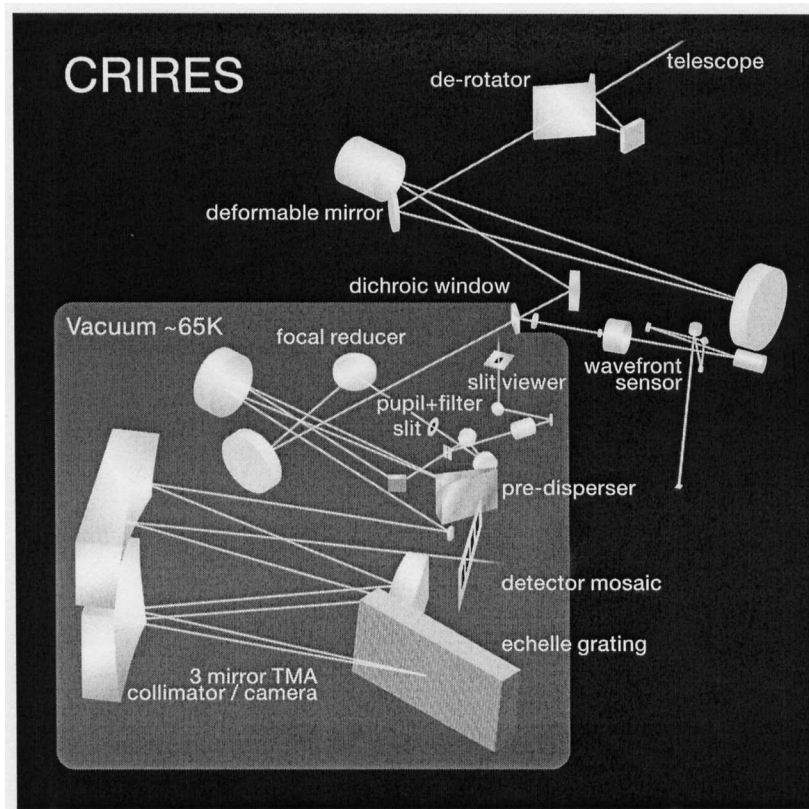
Figure 1.6: Setup of the CRIRES instrument, see text for details. Figure from Siebenmorgen and Smette (2008).

by four $512 \times 1024$ pixel InSb Aladdin III detectors[4]. There is a spacing between two adjacent detectors which is equivalent to approximately 280 pixels. A summary of the performance of the MACAO system was already shown in Fig. 1.5. The quality of the wavefront correction depends on the brightness of the AO-reference star, its distance to the target and on the seeing. The distance should not exceed $10''$ in order to achieve a significant improvement in spatial resolution. The optimal brightness of the reference star is $R = 11 \, \mathrm{mag}$ as this defines the saturation limit of the APDs. For brighter stars, neutral density filters have to be used to dim the light. Under average seeing conditions, stars as faint as $R = 14 \, \mathrm{mag}$ can be used as reference. Under very good seeing conditions, stars as faint as $R = 16 \, \mathrm{mag}$ will result in at least a mild improvement.

## 1.4   Stars

Detecting surface structure on giant stars is the scientific application of spectro-astrometry in this thesis. Various phenomena which take place in giant stars are related to the interior energy generation by nuclear fusion, as e.g., giant convection cells which are thought to be responsible for surface structure or the ejection of carbon-rich material which can form circum-stellar dust shells. Therefore, a very brief summary of the interior structure and evolution of stars is given here. A much deeper investigation on these topics can be found in various textbooks, e.g., in Böhm-Vitense (1992). The inner structure of a

---

[4]Actually, the detectors have $1024 \times 1024$ pixels but only half of the area is used

star is determined almost only by the hydrostatic equilibrium. The gravitational force is balanced by the gas pressure alone for most stars. Only in very massive and luminous stars, the radiation pressure contributes significantly. Even fast rotation does not impact strongly on the overall structure of a star. However, magnetic fields need to be considered if they are strong. This is the case for magnetic peculiar stars or white dwarfs and neutron stars. Only deviations from a pure dipole field result in a net magnetic force. Hydrostatic equilibrium can be expressed as
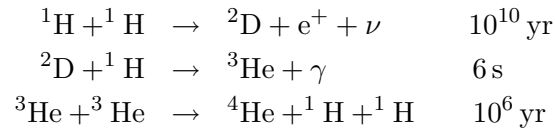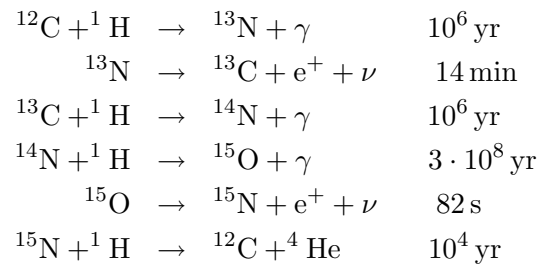
$$\mathrm{d}P/\mathrm{d}h = -\rho g, \tag{1.22}$$

where $h$ is the height within the star, $\rho$ is the density and $g$ the gravitational acceleration. Hydrostatic equilibrium is fulfilled to a very high degree in stars which do not pulsate. A deviation from the hydrostatic equilibrium leads to an expansion or contraction of the star.
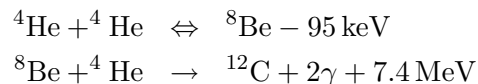
Thermal equilibrium also has to be satisfied in a star. This means that the energy loss caused by radiation has to be compensated by some inner energy source. For stars, this source is thermo-nuclear fusion. The type of nuclear fusion reaction that dominates the energy generation depends on the temperature. The lowest temperature is required by the proton-proton chain:

$$
\begin{aligned}
^{1}\mathrm{H} +\,^{1}\mathrm{H} &\;\rightarrow\; ^{2}\mathrm{D} + \mathrm{e}^{+} + \nu && 10^{10}\,\mathrm{yr} \\
^{2}\mathrm{D} +\,^{1}\mathrm{H} &\;\rightarrow\; ^{3}\mathrm{He} + \gamma && 6\,\mathrm{s} \\
^{3}\mathrm{He} +\,^{3}\mathrm{He} &\;\rightarrow\; ^{4}\mathrm{He} +\,^{1}\mathrm{H} +\,^{1}\mathrm{H} && 10^{6}\,\mathrm{yr}
\end{aligned}
$$

The reaction times are given for solar interior conditions of $T = 1.4 \cdot 10^{7}\,\mathrm{K}$, $\rho = 100\,\mathrm{g\,cm^{-3}}$ and a solar metallicity. There are two possible, additional PP-chain endings, involving Beryllium, Boron and Lithium as catalysts. These chains replace the third step of the first PP-chain under the presumption that there is already $^{4}\mathrm{He}$ or $^{7}\mathrm{Be}$ available. At higher temperatures, the CNO-cycle starts to work:

$$
\begin{aligned}
^{12}\mathrm{C} +\,^{1}\mathrm{H} &\;\rightarrow\; ^{13}\mathrm{N} + \gamma && 10^{6}\,\mathrm{yr} \\
^{13}\mathrm{N} &\;\rightarrow\; ^{13}\mathrm{C} + \mathrm{e}^{+} + \nu && 14\,\mathrm{min} \\
^{13}\mathrm{C} +\,^{1}\mathrm{H} &\;\rightarrow\; ^{14}\mathrm{N} + \gamma && 10^{6}\,\mathrm{yr} \\
^{14}\mathrm{N} +\,^{1}\mathrm{H} &\;\rightarrow\; ^{15}\mathrm{O} + \gamma && 3 \cdot 10^{8}\,\mathrm{yr} \\
^{15}\mathrm{O} &\;\rightarrow\; ^{15}\mathrm{N} + \mathrm{e}^{+} + \nu && 82\,\mathrm{s} \\
^{15}\mathrm{N} +\,^{1}\mathrm{H} &\;\rightarrow\; ^{12}\mathrm{C} +\,^{4}\mathrm{He} && 10^{4}\,\mathrm{yr}
\end{aligned}
$$

As for the PP-chain, other reaction cycle endings are possible. In total, one $^{4}\mathrm{He}$ is formed from four $^{1}\mathrm{H}$ while the total number of C, N and O nuclei stays constant. The importance of the alternative cycle endings is a change in the isotope ratio of the catalyst. At even higher temperatures of about $10^{8}\,\mathrm{K}$, the triple-alpha reaction is allowed:

$$
\begin{aligned}
^{4}\mathrm{He} +\,^{4}\mathrm{He} &\;\Leftrightarrow\; ^{8}\mathrm{Be} - 95\,\mathrm{keV} \\
^{8}\mathrm{Be} +\,^{4}\mathrm{He} &\;\rightarrow\; ^{12}\mathrm{C} + 2\gamma + 7.4\,\mathrm{MeV}
\end{aligned}
$$

In total, one $^{12}\mathrm{C}$ is formed from three $^{4}\mathrm{He}$. At very high temperatures, more massive elements can be created by nuclear fusion up to $^{56}\mathrm{Fe}$. Any element more massive than iron has to be created via supernova explosions. For very low mass stars, mainly the PP-chain occurs whereas in stars that have the mass of the Sun, the PP-chain and the CNO-cycle contribute to energy generation. In stars of spectral type A0 and hotter, the CNO-cycle dominates. The triple alpha reactions are not important for main sequence stars. Because

of the different reaction time scales of the different reaction steps, the relative abundances
of the elements involved in the CNO-cycle change. An increase in the nitrogen abundance
and a decrease in the carbon abundance is expected. This comes along with an increase
in the $^{13}C/^{12}C$ ratio. Thus, if these unusual abundances are observed, the operation of
CNO-cycle is proven.

In the outer regions of a solar-like stellar interior, energy transport is mainly done by convection whereas further inside, radiation is the most effective mechanism. Heat conduction
is ineffective in stellar interiors but plays the dominant role in stellar coronae because of
the low gas density and high temperature. Depending on the mass of a star, the relative
extents of the convection and radiation zones differ significantly.

The evolution of stars is also quite different depending on their initial mass and chemical
composition. Because of the temperature structure of a star, hydrogen fusion mainly takes
place in the centre and Helium is enriched there. As consequence, the core shrinks and has
to heat up. The hydrogen fusion via the CNO-cycle then takes place in the shell surrounding the core, if the temperature has sufficiently increased. At some point, the temperature
and pressure become too high for the hydrogen around the Helium core to stay stable.
The star starts to expand to reestablish hydrostatic equilibrium. While expanding, the
effective temperature of the star decreases and the convection zone increases its relative
extension. At about $5000\,K$, the convection zone reaches layers with nuclear processed
material and brings this material to the surface layers. At this point, the luminosity of
the star increases and the star moves upwards in the Hertzsprung-Russell diagram. In this
phase the star is called an asymptotic giant branch (AGB) star. When the temperature
is high enough to induce the triple alpha reactions, carbon is produced in the stellar centre. In the regions around the core, helium is produced simultaneously. During the triple
alpha phase, thermal irregularities result in the ejection of stellar material from the very
extended stellar atmosphere. If convection enriches the outer stellar layers with carbon
which can then be observed in the stellar spectrum, the object is called a carbon star.
Multiple material ejections may lead to a dust shell that surrounds the star. Depending
on the amount of ejected material, a strong veiling of the star in the optical and near-
infrared may take place, in particular in the very late stages of stellar evolution. For low
and intermediate mass stars, the temperature in the core does not suffice for further nuclear fusion processes after all helium has been burned to carbon. These stars finally expel
most of the remaining outer layers leaving an expanding shell[5] with a white dwarf in the
centre. Stars which are more massive than about eight solar masses reach temperatures
high enough to produce heavier elements up to iron which build up an onion-like shell
system. High mass stars will finally collapse to form a neutron star or black hole.

## 1.5   Molecular physics

The observations used in this thesis were performed in the range of the first overtone
transitions of carbon monoxide at $2.3\,\mu m$. To give some background on how these molecule-
transitions can be described, this section presents a short introduction to the physics and
nomenclature of ro-vibrational transitions of diatomic molecules The following section
partly follows Demtröder (2000).

Because of the non-zero total energy of a molecule, the two atomic nuclei rotate around
their centre of mass and/or vibrate. A diatomic molecule with the quantum numbers

---

[5]which may turn into a planetary nebula

$k = (n, L, \Lambda)$ can be described by the Schrödinger equation

$$\left(\frac{-\hbar^2}{2M}\nabla^2 + E_{\text{pot}}(R, k)\right)\chi(\mathbf{R}) = E \cdot \chi(\mathbf{R}). \tag{1.23}$$

Here, $R$ is the distance between the nuclei and $\chi$ is the wave function. The above equation is valid for the centre of mass system using the reduced mass. The wave function can be separated in spherical coordinates

$$\chi(R, \theta, \phi) = S(R) \cdot Y(\theta, \phi). \tag{1.24}$$

If the separation ansatz is plugged into Eq. (1.23), one obtains the following equation for the radial function $S(R)$

$$\frac{1}{R^2}\frac{\mathrm{d}}{\mathrm{d}R}\left(R^2\frac{\mathrm{d}S}{\mathrm{d}R}\right) + \frac{2M}{\hbar^2}\left[E - E_{\text{pot}}(R) - \frac{J(J+1)\hbar^2}{2MR^2}\right]S = 0 \tag{1.25}$$

and

$$\frac{1}{\sin\theta}\frac{\partial}{\partial\theta}\left(\sin\theta\frac{\partial Y}{\partial\theta}\right) + \frac{1}{\sin^2\theta}\frac{\partial^2 Y}{\partial\phi^2} + J(J+1)Y = 0 \tag{1.26}$$

for the angular function $Y(\theta, \phi)$.
The rotational energy of the molecule is

$$E_{\text{rot}} = \frac{1}{2}I \cdot \omega^2 = \frac{\mathbf{J}^2}{2I}. \tag{1.27}$$

Here, $\omega$ is the angular velocity, $I$ is the moment of inertia

$$I = M_1 R_1^2 + M_2 R_2^2 = MR^2, \quad \text{with} \quad M = \frac{M_1 \cdot M_2}{M_1 + M_2}, \tag{1.28}$$

and $\mathbf{J}$ is the angular momentum. $M$ is the reduced mass of the two nuclei. Quantum mechanics dictate that the square of the angular momentum can only take values of $\mathbf{J}^2 = J(J+1)\hbar^2$ which are characterised by the quantum number $J = 0, 1, 2, \dots$. The equilibrium distance shall be denoted as $R_e$, yielding

$$E_{\text{rot}} = \frac{J(J+1)\hbar^2}{2MR_e}. \tag{1.29}$$

for the rotational energy. Absorption of electro-magnetic waves by the molecule take place at frequencies of

$$\nu_{\text{rot}}(J) = (E(J+1) - E(J))/\hbar \tag{1.30}$$

for a transition between the levels $J \to (J+1)$. It can be shown that only molecules with a permanent dipole moment are able to absorb at purely rotational transitions. Those transitions have wavelengths in the microwave region. The above energy levels are only valid for a rigid rotator. In reality, the centrifugal force increases the moment of inertia, and reduces the rotational energy for constant angular momentum. This influence can be accounted for by a correction to the energy levels: for distances close to the equilibrium distance, the potential of the centrifugal force can be approximated by a parabola. Thus, a linear restoring force results which can be characterised by the constant $k$. It is straightforward to show that the corrected rotational energy levels are

$$E_{\text{rot}} = \frac{J(J+1)\hbar^2}{2MR_e} - \frac{J^2(J+1)^2\hbar^4}{2M^2kR_e^6} + \frac{3J^3(J+1)^3\hbar^6}{2M^3k^2R_e^{10}} \pm \dots. \tag{1.31}$$

Assuming a non-rotating molecule, the rotational quantum number is $J = 0$. The radial wave function S(R) only depends on the form of the potential energy. A parabolic potential would lead to the energy values of the harmonic oscillator $E(\nu) = (\nu + 1/2)\hbar\omega$. However, the parabolic potential is only a good approximation for $R \approx R_e$. A better approach is the *Morse* potential

$$E_{\text{pot}}(R) = E_D \cdot \left(1 - e^{-a(R-R_e)}\right)^2, \tag{1.32}$$

where $E_D$ is the dissociation energy of the molecule. In contrast to the parabolic potential, the Morse potential does converge to $E_D$ for $R \to \infty$, but does not describe the true potential well for $R \ll R_e$ as the latter diverges for $R \to 0$ and the Morse potential does not. The corresponding energy levels for the Morse potential are

$$E_{\text{vib}}(\nu) = \hbar\omega(\nu + 1/2) - \frac{\hbar^2\omega^2}{4E_D} \cdot (\nu + 1/2)^2. \tag{1.33}$$

A general Taylor-series approximation to the potential energy can even yield better results, e.g., the Lennard-Jones-potential $E_{\text{pot}}(R) = a/R^{12} - b/R^6$. However, the Morse potential has the advantage that the Schrödinger equation may be solved analytically whereas numerical methods are necessary for more complex potentials. The vibrational frequencies are typically one to two orders of magnitude larger than those of rotation. Therefore, vibrational transitions are found in the infrared.

Now, the interaction of rotation and vibration shall be considered. As the frequency of vibration is much higher than the one of rotation, $R$ changes during one rotation period. This induces variations of the moment of inertia. Because the angular momentum of the molecule stays constant, the rotation frequency changes, too. The total energy $E = E_{\text{rot}} + E_{\text{vib}} + E_{\text{pot}}$ also is conserved which explains why there is a continuous energy redistribution between rotation, vibration and potential energy. The mean rotational energy can be written as the quantum-mechanical expectation value of $1/R^2$

$$< E_{\text{rot}} > = \frac{J(J+1)\hbar^2}{2M} \int \psi_{\text{vib}}^* \frac{1}{R} \psi_{\text{vib}} \, \mathrm{d}R, \tag{1.34}$$

with $\psi_{\text{vib}}$ being the vibration wave function, i.e., $S(R)$.

A molecule may absorb or emit light when passing from one level to another. The probability for such a transition is proportional to the square of the dipole matrix element. Thus, the relative intensities of the spectral lines can be obtained if the corresponding matrix elements are calculable. It can be shown that the matrix element for hetero-nuclear diatomic molecules can be expressed by

$$\mathbf{M}_{ik} = e \cdot \int S_{\nu_i}(R) \cdot S_{\nu_k}(R) \cdot R^3 \, \mathrm{d}R \cdot \int Y_{J_i}^{M_i} Y_{J_k}^{M_k} \cdot \mathbf{p} \cdot \sin\theta \, \mathrm{d}\theta \, \mathrm{d}\phi. \tag{1.35}$$

Here, $e$ is the electron charge, $S$ and $Y$ are the vibration- and rotation- wave functions, respectively, $J$ and $M$ the rotational angular momentum and its projection to a given direction; $\mathbf{p}$ is the unity vector in the direction of the dipole moment. For the first integral, the selection rule $\Delta\nu = \nu_i - \nu_k = \pm 1$ is valid for the harmonic oscillator. In the case of asymmetric potentials as, e.g., the Morse potential, transitions of $\Delta\nu = 2, 3, 4, \ldots$ are also allowed, but at much lower probabilities and intensities. The second integral is always zero, except for $\Delta J = \pm 1$. It is common practice to denote the upper level by $(\nu', J')$ and the lower level by $(\nu'', J'')$. The transitions

$$\Delta J = J' - J'' = +1 \quad \text{are called R lines,} \tag{1.36}$$

$$\Delta J = J' - J'' = -1 \quad \text{are called P lines.} \tag{1.37}$$

In addition, electron transitions are possible with $\Delta J = 0$ if the projection of the electron orbital angular momentum changes by $\pm 1$. The corresponding spectral lines are called Q lines. Figure 1.7 depicts the wavenumbers and $J$-values for the P-, Q- and R- lines. Such
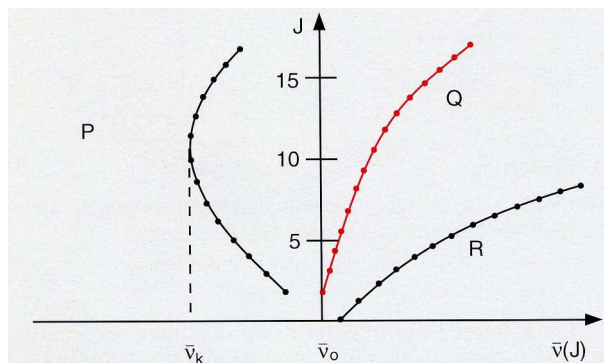


Figure 1.7: Exemplary Fortrat diagram showing the P-, Q- and R- branch lines. In this specific case, the P-branch lines form a bandhead at a wavenumber of $\bar{\nu}_k$.

a plot is called a Fortrat-diagram. Obviously, they form branches; for some molecules, among those carbon monoxide, one of the branches reverses the sign of the slope at some point. In the spectrum, one sees a band head at the corresponding wavenumber, i.e., an accumulation of lines with no lines to higher (lower) wavenumbers and lines at increasing spacing at lower (higher) wavenumbers. The band heads of carbon monoxide were chosen as the wavelength region of choice for the observations in this thesis. At about $2.3\,\mu$m are the $\Delta\nu = 2$ R-branch lines of $^{12}C^{16}O$ and $^{13}C^{16}O$.

## 1.6 The `PHOENIX` atmospheric code

The modelling of spectro-astrometric signatures in order to deduce the most likely source configuration requires the availability of precise synthetic spectra for the target, cf. Sect. 2.7. This work uses the `PHOENIX` code:
`PHOENIX` is a general-purpose stellar atmosphere code which allows to study the structure of stellar atmospheres and to calculate model spectra for comparison with observations. Details on the code are given, e.g., in Hauschildt and Baron (1999). Stellar atmospheres can be fully described by energy conservation and the hydrostatic equation. For the calculation of the spectra used in this thesis, both equations are time-independent but interdependent. Hence, the atmosphere is static and is furthermore assumed to be spherically symmetric. Stellar rotation and outflows, i.e., stellar winds, are neglected. The latter could be critical for giants and supergiants which are studied in this work. However, present data suggests that the targets considered here do not feature strong winds, see Chap. 3. In order to obtain a synthetic spectrum, first, a self-consistent atmosphere model has to be found. With this model, the determination of the spectrum is then possible.
The radiative transfer equation can be formulated in spherical polar coordinates as

$$\frac{\mu}{\chi_\nu}\frac{\partial I_\nu}{\partial r} + \frac{1-\mu^2}{\chi_\nu r}\frac{\partial}{\partial \mu}I_\nu = S_\nu - I_\nu. \tag{1.38}$$

Here, $I_\nu(r,\nu,\mu)$ is the monochromatic specific intensity, $\nu$ is the frequency and $\mu = \cos\Theta$ is the angle of a beam of light. $S_\nu = j_\nu/\chi_\nu$ is the source function which is the ratio of the monochromatic emissivity and the monochromatic extinction coefficient. Although a

formal solution to the radiative transfer equation (1.38) can be found, this solution can only be calculated iteratively as the source function $S_\nu$ and the intensity $I_\nu$ depend on each other. As can be seen from Eq. (1.38), the extinction coefficient, which is also called opacity, is important for the calculation of the atmospheric model and the spectrum. The stellar atmosphere may be described by the effective temperature $T_{eff}$, the acceleration due to surface gravity $g$[6], the luminosity $L$ and the abundances. The surface gravity appears in the hydrostatic equation

$$\frac{\mathrm{d}P}{\mathrm{d}\tau_\nu} = \frac{\mathrm{d}P_{gas}}{\mathrm{d}\tau_\nu} + \frac{\mathrm{d}P_{rad}}{\mathrm{d}\tau_\nu} + \frac{\mathrm{d}P_{mic}}{\mathrm{d}\tau_\nu} = \frac{g}{\chi_\nu}, \tag{1.39}$$

where $P$ is the pressure which consists of contributions by the gas pressure $P_{gas}$, the radiative pressure $P_{rad}$ and the pressure caused by micro-turbulence $P_{mic}$. The optical depth is denoted by $\tau$ and gravitation leads to $g = GM/R^2$, with $G$ being the constant of gravitation, $M$ being the stellar mass and $R$ being the radius of the star. Conservation of energy can be written as

$$F_{rad} + F_{conv} = C = \sigma T_{eff}^4, \tag{1.40}$$

with $F_{rad}$ and $F_{conv}$ being the radiative and convective flux, respectively. The former is defined as

$$F_{rad} = \int_0^\infty F_\nu \, \mathrm{d}\nu, \tag{1.41}$$

where the flux $F_\nu$ is given by

$$F_\nu = \int I_\nu \cos\Theta \, \mathrm{d}\Omega, \tag{1.42}$$

with $\mathrm{d}\Omega$ being the solid angle. $\sigma$ is the Stefan-Boltzmann constant and $T_{eff}$ is an effective temperature, i.e., only a characteristic temperature which does not necessarily happen to exist within the atmosphere. Energy transport within an atmosphere happens mostly via radiation and/or convection. Convection is modelled in PHOENIX with the mixing-length theory: convection cells ascend and descend in the atmosphere depending on whether they have higher or lower temperature than the surrounding gas. After a certain distance, the mixing-length, the convection cells dissolve and the energy difference to the surroundings vanishes. This leads to a net energy transport. The models used in this work make the assumption of local thermal equilibrium (LTE). As a consequence, quantities that are determined by occupation numbers, i.e., opacity and total pressure, only depend on the gas temperature and the electron density.

The calculation of an atmosphere model works as follows: First, a temperature and density structure is supplied as initial guesses. Using the hydrostatic equation, a new atmospheric structure is determined. With this structure, new opacities can be calculated and with these, the radiative transfer equation can be solved and the corresponding spectrum is determined. With this solution, the conservation of energy can be verified. If the conservation is satisfied at the desired accuracy, the final model is found. Otherwise, a temperature correction is applied and the whole procedure is repeated.

## 1.7   Lunar occultations

As the Moon orbits the Earth, it passes over various celestial objects causing so-called lunar occultations. This method on the one hand allows to study several astrophysical phenomena on milli- and microarcsecond scales, and on the other hand is the foundation

---

[6]which is often given in terms of $\log(g)$

of the CHARM2-catalogue (Richichi et al., 2005) which was used in this work to compile the target-list. For these reasons, the method is described in the following.

If the Moon occults a star, the star light will vanish almost immediately. However, as the diameter of the star is non-zero, the light curve will decrease to zero in a non-zero but very small time interval. Typically, the time scale of the disappearing of a star is of the order of 10 ms. The exact value of the duration depends on the stellar diameter, and the point on the disk of the Moon where the occultation takes place. If the star is about to vanish behind the Moon for an observer on Earth, the star light will be diffracted by the surface of the Moon and a diffraction pattern will be visible at the site of the observer. The configuration is identical to the case of diffraction at a straight edge, cf. Sect. 1.1 and Fig. 1.3. If the relation (1.19) is applied to this case with, e.g., $\lambda = 600$ nm and $z_0 = 384,000$ km, a fringe spacing of about 15 m results. For polychromatic light, the fringes are blurred to some degree as the fringes corresponding to light of different wavelengths have different spacings. A structured source leads to a modified fringe pattern. To extract information about a source, various models are compared to the observed fringe pattern. The best-fitting model yields the desired parameters, e.g., the apparent diameter of a star. The detection of the fringe pattern is done with a single telescope. To achieve this, the movement of the Moon on the sky is exploited. It takes some tens of milli-seconds for the fringe pattern to cross the telescope. Hence, instrumentation is needed which allows for integration times of the order of just a few milli-seconds. Much progress has been made in the past decades on this observing technique as well as on the instrumentation. Today, even the VLT/ISAAC instrument has been tested to be suitable for lunar occultation observations. Thus, it is possible to reach targets as faint as $K = 12.5$ mag, cf. Richichi et al. (2007). High S/N can easily be achieved even for medium-bright targets ($K = 7 - 10$ mag) with the 8.4 m telescope. Lunar occultation was the first observing technique to reach spatial resolutions of 1–2 mas, see, e.g., Richichi (1989). Diverse occultation programs were carried out over many years and yielded apparent diameters for many stars. If the absolute luminosity of a star is known, occultation observations can yield an independent estimate of the effective temperature of a star. The apparent diameter measurements were compiled into catalogues. These are today the largest database for stellar apparent diameters, the CHARM2 and CADARS catalogues, Richichi et al. (2005); Pasinetti Fracassini et al. (2001), respectively. However, these catalogues also contain diameter estimates of other observing methods like interferometry or indirect methods. They were used in this thesis to obtain a list of possible targets during the planning of the observations.

## 1.8 Interferometry

As interferometry is an observing technique which has been proven to routinely achieve spatial resolutions of milli-arcseconds, and thus, has similar or identical applications as spectro-astrometry, it is presented here briefly.

The wave property of light allows for interference as it can, e.g., be observed with the double-slit experiment. A comprehensive review on interferometry is Monnier (2003). Parts of the following section were guided by this review and references therein. Instead of two slits, two telescopes can be used to collect light at different spatial coordinates. Both light beams are then brought to interference in order to detect the fringe pattern. The separation of the telescopes is called *baseline* ($b$) and is the equivalent to the slit separation. The fringe spacing can easily be determined to be $\Delta\Theta = \lambda/b$ rad, which yields a fringe spatial frequency of $u = b/\lambda$ rad$^{-1}$. Figure 1.8 shows the interference patterns which result from a single point source and from a binary point source in one dimension, respectively. The distance of the two point sources has been chosen to be exactly one half
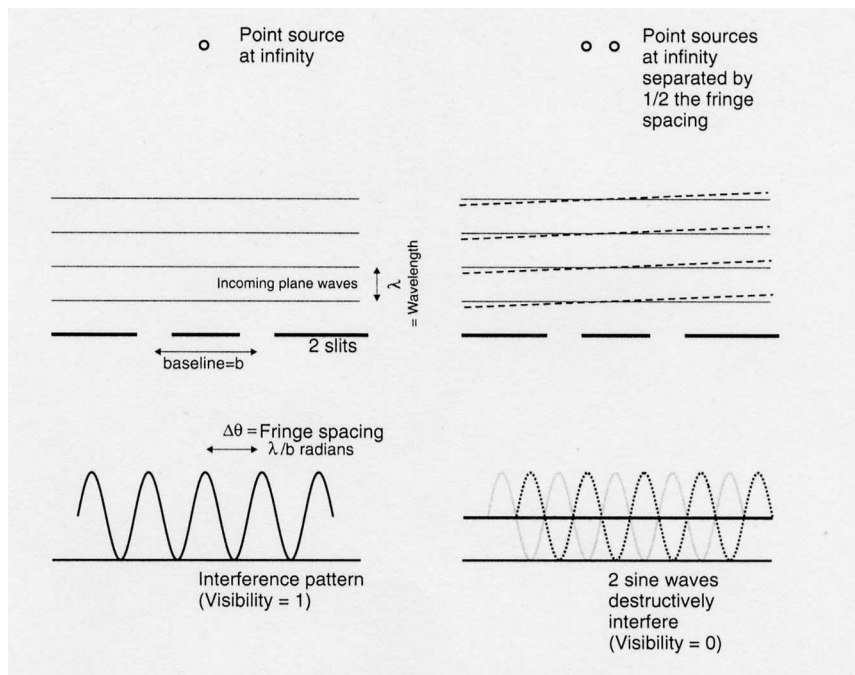
Figure 1.8: The interference patterns are shown which are caused by a single point source (left) and a binary point source (right). In the latter case, the separation of the binary is half the fringe spacing causing the fringes to disappear completely.

the fringe spacing. Thus, the fringes disappear completely, leaving the intensity constant at $1/2$. For the two-slit case, the visibility can be expressed more generally by

$$V = \frac{I_{\max} - I_{\min}}{I_{\max} + I_{\min}}, \tag{1.43}$$

which is equivalent to the ratio of the fringe amplitude and the average intensity. The two examples shown in Fig. 1.8, therefore, have visibilities of one and zero, respectively. Similar to the Rayleigh criterion, cf. Sect. 1.1.1, a spatial resolution can be defined for interferometry: if the visibility of a binary is zero for the longest baseline, this binary is defined to be resolved. In mathematical terms, this corresponds to $\Delta\Theta = \lambda/2b$ rad. It can be proven that the contrast of the fringes is directly related to a Fourier component of the incoming brightness distribution. The visibility is proportional to the Fourier component corresponding to the fringe spatial frequency and the phase of the fringe pattern is equal to the Fourier phase. This is described by the Van Cittert-Zernike theorem which is discussed and proven in, e.g., Thompson et al. (2001). A target shall be observed to emit light of frequency $\nu$ at an intensity of $I_\nu(\Theta, \phi)$ and the extent of the source on the sky is very small. The covered coordinates $[\Theta_0, \Theta_0 + \delta\Theta]$ and $[\phi_0, \phi + \delta\phi]$ can be approximated by Cartesian coordinates $x_\Omega, y_\Omega$. Then, a complex visibility $\mathcal{V}_\nu(u, v)$ can be defined to be the Fourier transform of the brightness distribution $I_\nu(\mathbf{r}_\Omega)$ as

$$\left| \mathcal{V}_\nu \left( \frac{\mathbf{D}}{\lambda} \right) \right| \cdot e^{-\mathrm{i}\phi_{\mathcal{V}_\nu}} = \frac{\int_{\delta\Omega} \mathrm{d}x_\Omega \, \mathrm{d}y_\Omega I_\nu(\mathbf{r}_\Omega) \, e^{-2\pi\mathrm{i}((\mathbf{D}/\lambda)\cdot\mathbf{r}_\Omega)}}{\int_{\delta\Omega} \mathrm{d}x_\Omega \, \mathrm{d}y_\Omega I_\nu(\mathbf{r}_\Omega)}. \tag{1.44}$$

Here, $\mathbf{r}_\Omega = (x_\Omega, y_\Omega)$ and the complex visibility is normalised such that $\mathcal{V}(\mathbf{D}/\lambda = 0) = 1$. The baseline vector projected onto the sky plane in units of the wavelength is defined to be the $(u, v)$-plane, i.e., $\mathbf{D}/\lambda = (u, v)$. Theoretically, the brightness distribution (i.e.

the image) can be reconstructed by the inverse Fourier transform if all Fourier components and phases were known. One obstacle in achieving this is atmospheric turbulence. These turbulences are responsible for a reduction of the spatial resolution attainable by a telescope. More important for interferometry is the fact that as the turbulences vary with time and location, their effect on the incoming light is different for two telescopes constituting an interferometer. A phase shift, $\Delta\phi$, between the wavefronts registered at the two telescopes is the result. This translates into a shift of the fringe pattern. The shift, in turn, violates the requirements for the Van Cittert-Zernike theorem, and, hence, image reconstruction cannot be performed. One possibility to deal with this problem is to use the concept of *closure phases*: if three telescopes are used, three different phases are measured. These phases each consist of the target-intrinsic phase and the atmospheric phase shift:

$$\Phi_{obs}(1-2) = \Phi_{\text{int}}(1-2) + (\phi(2) - \phi(1)) \tag{1.45}$$

$$\Phi_{obs}(2-3) = \Phi_{\text{int}}(2-3) + (\phi(3) - \phi(2)) \tag{1.46}$$

$$\Phi_{obs}(3-1) = \Phi_{\text{int}}(3-1) + (\phi(1) - \phi(3)) \tag{1.47}$$

The closure phase now is defined to be $\Phi_{\text{clo}}(1,2,3) = \Phi_{\text{int}}(1-2) + \Phi_{\text{int}}(2-3) + \Phi_{\text{int}}(3-1)$ and is independent from the atmospheric phase shifts as they cancel out during summation. Although a quantity is found which is independent from atmospheric influence, the closure phase cannot deliver as much information on the fringe phase as is needed for a complete reconstruction. The number of independent closure phases is always less than the number of Fourier phases. However, with increasing number of telescopes used, the number of closure phases converges to the number of Fourier phases: for three telescopes, the level of completeness is only $33\%$, but for 21 telescopes it is already $90\%$. Various image reconstruction algorithms allow to calculate the brightness distribution which causes the measured Fourier amplitudes and phases. Often, there is no unique solution to the image reconstruction problem because of the possible incompleteness of the measurements. Independently from the reconstruction process, observed visibility curves can be compared to model predictions in order to constrain the real target configuration. This procedure, e.g., allows to determine the diameter of a star with interferometry well below the diffraction limit of the individual telescopes which constitute the interferometer. The better the coverage of the $(u,v)$-plane, the more reliable is the image reconstruction procedure. Depending on the expected complexity of the source, more or less $(u,v)$-coverage is needed. Increasing the number of telescopes, of course, increases the number of $(u,v)$-points. However, obtaining exposures over several hours also leads to a better coverage as the Earth rotates. Moving the telescopes of the interferometer between exposures is another way to increase the coverage.

Interferometry has become available for wavelengths from the radio region up to the optical. The technical requirements increase with decreasing wavelength of the light as the interfering light beams need to be joined at an accuracy of better than a fraction of the wavelength. Thus, the beam combiner is a very critical part of the instrument. It also needs to compensate for the rotation of the Earth which results in slightly different positions of a target for any two (or more) telescopes. Most interferometers which operate in the optical or infrared use small telescopes because of the seeing limitations. No advantage results from using larger telescopes. For example, the NPOI and IOTA operate in the optical and near-infrared, respectively, and consist of telescopes of $14\,\mathrm{cm}$ and $45\,\mathrm{cm}$, respectively. The maximum number of telescopes which have successfully been combined is six for such wavelengths. In the last ten years, interferometers have successfully been installed and then operated at large telescopes like KECK and VLT, exploiting the benefits of adaptive optics. Modern instruments also allow for a spectral dispersion of the fringes,

e.g., with the AMBER instrument at the VLT. Interferometry is also possible using a single telescope with aperture masking: a mask with two or more apertures is placed in front of the telescope aperture. Interference then takes place between the light beams of the different apertures of the mask.

Various giant and supergiant stars have been observed with interferometry in the past years. Image reconstruction has not been very reliable because of the small number of telescopes that constitute the optical and infrared interferometers. Nevertheless, asymmetries have been detected for some targets by either fitting visibility curves and/or by aperture synthesis imaging. Examples are Betelgeuse and Arcturus, see Young et al. (2000); Lacour et al. (2008).

# Chapter 2

# Spectro-astrometry

Despite the enormous progress that has been made in building larger telescopes and introducing new techniques such as adaptive optics, there are many astronomical phenomena on spatial scales well below the diffraction limit of modern telescopes. Using interferometry is one way to obtain information on sub-diffraction-limited scales, cf. Chap. 1. A different approach is described in detail in this chapter: the method of spectro-astrometry. This thesis presents a systematic analysis of the method and its potential to achieve sub-diffraction-limited spatial resolution. The chapter begins with the basic concept of spectro-astrometry in Sect. 2.1. Then, ways to simulate spectro-astrometric signatures for arbitrary object configurations are presented as well as how to remove instrumental artefacts. The influences of bad pixels, image distortions and tilted longslit spectra are discussed in Chap. 3. The mapping of light from the slit plane of the spectrograph to the detector is important for the understanding of spectro-astrometry signatures and is described in Sect. 2.2. The position spectrum and the width spectrum as the two fundamental spectro-astrometry quantities are introduced in Sect. 2.3 and their properties are analysed. Different methods to extract the spectro-astrometric quantities from the longslit spectrum as well as the associated formal errors are discussed in Sect. 2.4. An algorithm for the simulation of the position and width spectra for arbitrary PSF- and object configurations is mandatory for further analysis of the data. This procedure is described in Sect. 2.5. The role of instrumental artefacts and ways to removal those from the data is explored in Sect. 2.6. The procedure of deducing the source configuration from measured spectro-astrometric quantities follows in Sect. 2.7 and in Sect. 2.8, computational issues of the code are discussed. Simulations on stellar disks containing spots in various configurations were performed and the results hereof are given in Sect. 2.9. The final section of this chapter, Sect. 2.10, summarises important publications of other authors on the topic of spectro-astrometry.

## 2.1  Basics

Structured astronomical sources consist of regions with different spectral energy distributions (SEDs). If the apparent dimensions of such a source are below the diffraction limit of the telescope, imaging only shows a featureless disk with the size of the disk being determined by diffraction and atmospheric seeing. However, the location of the photocentre of the object varies between images taken in different band passes if different regions of the source contribute differently at individual wavelengths. In principle, the position of the photocentre can be determined to sub-diffraction-limited accuracy, depending only on the signal-to-noise ratio (S/N) and on the width of the PSF. The latter originates from

the seeing and the performance of adaptive optics. The idea to measure the wavelength-dependancy of the photocentre was introduced by Beckers (1982). The method has, in principle, great potential but is difficult to implement: the centroid measurements have to be performed simultaneously in different wavebands and through the same optical path in order to guarantee precise results. Thus, special instrumentation needs to be constructed. Depending on the energy distribution of the target, special waveband filters need to be used which is impracticable. Because of these problems, no significant scientific results were obtained at that time. The crucial idea to use a longslit spectrograph equipped with a CCD-detector, instead, was first conceived by Bailey (1998). He also coined the term "spectro-astrometry". Taking a longslit spectrum, the centroid position of the source can be determined independently for each wavelength bin. The centroid position changes over any spectral feature in the *difference* SED of the source. For a two-component source the difference SED simply is the difference of the two components' SEDs. For the difference SED of more complex sources see Sect. 2.5. Because of the usage of a CCD-detector the centroid can be determined reliably to subpixel accuracy. Usually, this corresponds to spatial scales well below the diffraction limit of the telescope. Such resolution can be achieved because spectro-astrometry is a wavelength-differential method, i.e., only relative centroid variations between adjoining wavelength bins are considered. Since each spectral feature leads to a centroid variation, cross-correlation with the difference SED strongly improves the detectability of weak spectro-astrometric signatures.

## 2.2   Object mapping

A longslit spectrograph is a 1D-imager which maps the brightness distribution in the slit plane onto the detector plane. The mapping can be described by the (plane) grating equation

$$m\lambda = a \cdot (\sin\alpha \pm \sin\beta).$$

Here, $a$ is the grating constant, $m$ the order of interference, $\lambda$ the wavelength, $\alpha$ the angle of the incident light with respect to the normal onto the grating and $\beta$ the angle of the diffracted light with respect to the normal. The sign in the grating equation depends on whether incoming and diffracted light lie on the same side of the normal to the grating. The direction along the slit is the spatial axis, here denoted with $x$. The direction orthogonal to the slit is the dispersion axis, here $y$. Any point in the slit plane with identical $x = x_0$ is mapped onto the same spatial coordinate in the detector plane $x^{'} = x_0^{'}$. Thus, the mapping $x \leftrightarrow x^{'}$ is bijective. However, the mapping $\lambda \leftrightarrow \lambda^{'}$ is not bijective, with $\lambda$ being the wavelength of the incident light and $\lambda^{'}$ the wavelength bin on the detector. This can easily be seen: a light source in the centre of the slit is mapped onto the detector plane as $(x_0, \lambda_0, y_0) \rightarrow \left(x_0^{'}, \lambda_0^{'}\right)$. An off-centre light source (oc) leads to a slightly different angle of incidence onto the grating ($\alpha_{\mathrm{oc}} = \alpha_{\mathrm{centre}} + \mathrm{d}\alpha$). According to the grating equation, this results in a deviation in $\beta$, i.e. $\beta_{\mathrm{oc}} = \beta_{\mathrm{centre}} + \mathrm{d}\beta$. This translates into a shift in wavelength $\mathrm{d}\lambda$. The latter is proportional to the distance of the light source from the centre of the slit ($\mathrm{d}y$)

$$\mathrm{d}\lambda = K \cdot \mathrm{d}y. \tag{2.1}$$

Here, $\mathrm{d}\lambda$ is measured in Ångström (Å) and $\mathrm{d}y$ in arcseconds. The constant of proportionality $K$ can be derived if the characteristics of the spectrograph are known.
Thus, a monochromatic light source with non-zero extent in the slit plane will be mapped onto an area on the detector corresponding to a non-zero wavelength span $\Delta\lambda$. The larger the extent of the source and/or the larger the slit width the lower the spectral resolution

of the longslit spectrum will be. The object mapping is the basis for calculating and understanding spectro-astrometric signatures and artefacts which will be discussed in the next sections.

## 2.3    Properties of spectro-astrometry

In this section I will analyse the different spectro-astrometric signatures with the example of a binary source. The signatures of interest are the centroid position over wavelength and the width of the spatial profile on the detector over wavelength, henceforth denoted by $\mathcal{C}(\lambda)$ and $\mathcal{W}(\lambda)$, respectively. Since a longslit spectrograph only probes a one-dimensional cut through the light source along the slit various slit orientations need to be applied to study the source. The binary is assumed to be placed along the slit axis. The two components
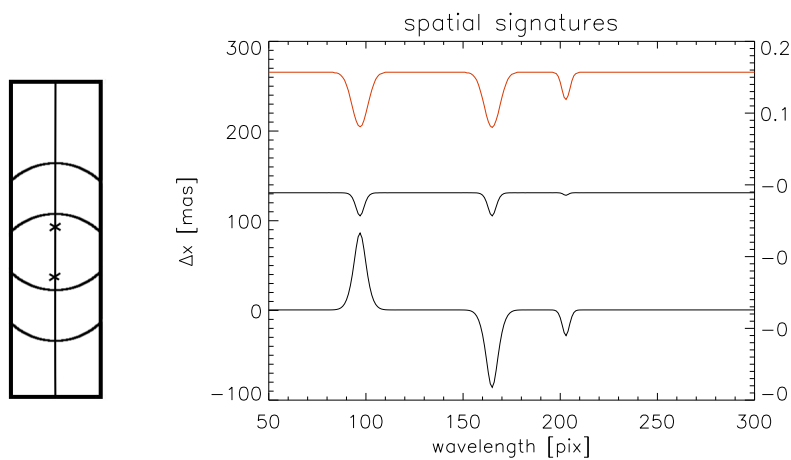


Figure 2.1: On the left the spectrograph slit is shown. The two "x" indicate the position of the binary components and the circles around them the actually used (circular) PSF. The right panel presents the results of the simulations: the upper curve is the SED of the system, the lower curve is $\mathcal{C}(\lambda)$ and the middle one is $\mathcal{W}(\lambda)$. The latter is offset by 130 mas. The signatures are only due to the spatial separation of the components, no velocity field has been used. The SED of one component consists of the left spectral line, the SED of the other component has the two lines at larger wavelengths.

are assumed to have different SEDs but identical continuum brightness. The configuration, the SEDs as well as the centroid and width spectra are shown in Fig. 2.1. The centroid is exactly in the middle of the binary in the continuum, because of the equal brightness, and moves towards the brighter component in the absorption lines. The width of the profile also stays constant in the continuum and gets smaller in the line as the contribution of one component vanishes. The amplitudes of the signatures depend on the spatial separation of the components and on the ratio of the components' brightness to the total brightness of the target. This means that for the amplitude one has $A \propto d \cdot I_R$, where $d$ is the apparent separation of the components on the sky and $I_R$ is the ratio just mentioned. During the entire thesis, the term *spatial resolution* denotes the effective spatial resolution $A_{\min}$ which is related to the real spatial resolution $d_{\min}$ by the above relation. Here, $A_{\min}$ is the smallest amplitude which can be detected in the spectro-astrometric quantities and $d_{\min}$ is the smallest spatial separation of two sources on the sky. Theoretically, $A_{\min}$ is given by Eq. (2.6). If the binary is placed orthogonally to the slit axis no features appear in $\mathcal{C}(\lambda)$ and $\mathcal{W}(\lambda)$. Naturally, the features in both spectro-astrometric spectra

directly correlate with the source's difference spectrum (for a binary, the latter simply
is the difference of the components' SED). This correlation allows for the application of
cross-correlation to detect spectro-astrometric signatures that are only marginally above
the noise. The effect depicted in Fig. 2.1 is only caused by the spatial separation of the
two components, hence, those signatures are called *spatial*. In contrast, non-zero radial
velocities induce *kinematic* signatures: the Doppler effect leads to a blue/red shift of the
SEDs. Even if the components have identical rest-SEDs the Doppler shift will lead to
a non-zero difference SED and, thus, to the signatures plotted in Fig. 2.2. Obviously,
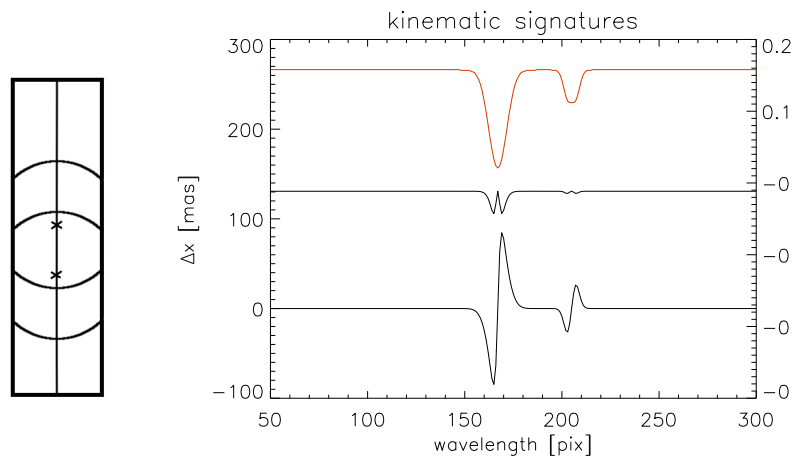


Figure 2.2: Same as Fig. 2.1 but for two components with identical rest-SEDs and radial system
velocities larger than zero. One component has positive, the other negative radial velocity.

kinematic and spatial signatures can easily be distinguished. An important question is
whether it is possible to discern different source configurations by the spectro-astrometric
signatures alone, e.g., does a binary star have $\mathcal{C}(\lambda)$, $\mathcal{W}(\lambda)$ different from those of a star that
is surrounded by a disk. As the spectro-astrometric signatures are directly correlated with
the difference spectrum of the target, different source configurations will often be easily
distinguishable. It will turn out that both spectro-astrometric quantities, $\mathcal{C}(\lambda)$ and $\mathcal{W}(\lambda)$,
have to be considered for the interpretation of observed data as well as for the removal of
instrumental artefacts, cf. Sect. 2.6 and Chap. 4. A problem is that the signatures in $\mathcal{W}(\lambda)$
in many cases seem to have smaller amplitudes than those in $\mathcal{C}(\lambda)$, cf. Figs. 2.1 and 2.2. As
the theoretical spatial resolution limit is worse in $\mathcal{W}(\lambda)$ compared to $\mathcal{C}(\lambda)$, the detection
of features in $\mathcal{W}(\lambda)$ can be difficult and there may only be usable information on $\mathcal{C}(\lambda)$. In
fact, there are several source configurations which lead to larger amplitudes in $\mathcal{W}(\lambda)$, e.g.,
two similar spots on different hemispheres on a stellar disk, cf. Sect. 4.3.2. Such a two-
spot configuration even leads to no features at all in the $\mathcal{C}(\lambda)$ spectrum for identical spots.
Because the detection of features in $\mathcal{W}(\lambda)$ requires larger S/N ratios, it may be difficult to
detect such signatures at all. The same problem occurs for a single spot which is located
right at the centre of the stellar disk: this only leads to features in $\mathcal{W}(\lambda)$. The concept of
spectro-astrometry, nevertheless, allows to detect various astronomical phenomena on very
small spatial scales. As a longslit spectrograph images a one dimensional cut through the
target, one needs to obtain exposures at various position angles to get 2D-information on
the source. Depending on the target properties, observing time constraints may prevent
a good sampling of the source. Finally, it is important to realize that a rotation of the
spectrograph with respect to the target by 180° leads to a change in sign of $\mathcal{C}(\lambda)$ and $\mathcal{W}(\lambda)$
for target-inherent features but there is no such change for instrumental artefacts. This
property is important when significant instrumental artefacts are present, cf. Sect. 2.6.

## 2.4 Position/width spectrum extraction

The reliable extraction of the spectro-astrometric signatures from the longslit spectra is a critical and important issue for the analysis of the data. The errors associated with that procedure need to be estimated precisely in order to determine the total error in the centroid/width spectra. The latter is important, e.g., when fitting models to observed data.

### 2.4.1 Profile fitting

Even for a point source, the extent of a longslit spectrum in the spatial direction on the detector will be non-zero due to seeing effects and/or light diffraction. Thus, some functional form can be fitted to the spatial profile in order to determine its centroid position and width. Random processes can often be described by a Gaussian distribution. Whether this is a valid description for the spatial profile has to be tested for each case individually because there may be instrumental influences that lead to other profile shapes. Assuming the spatial profile to be Gaussian and considering that a CCD-detector discretely records the longslit spectrum in equally sized pixels, the formal error in determining $\mathcal{C}(\lambda)$ and $\mathcal{W}(\lambda)$ can be derived as follows. The general derivation for the two-dimensional case can be found in Condon (1997). Here, the most important steps for the one-dimensional are sketched.

A Gaussian with peak amplitude $A$, central position $x_0$ and width $\sigma$ is defined as

$$P(x) = A \cdot \exp\left(-\frac{(x - x_0)^2}{2\sigma^2}\right).$$

The profile $P$ is assumed to be sampled by $N$ pixels with intensities of $a_i$ where $i = 1, \ldots, N$. If the error distribution is Gaussian and its root-mean-square deviation (rms) $\mu$, then the best fit to the discrete sampling will minimise the $\chi^2$ measure

$$\chi^2 = \sum_{i=1}^{N} \frac{(a_i - P(x_i))^2}{\mu^2}.$$

For each of the three free parameters $p_j = (A, x_0, \sigma)$, the minimisation of $\chi^2$ is equal to

$$\frac{\partial \chi^2}{\partial p_j} = \frac{2}{\mu^2} \sum_{i=1}^{N} (a_i - P(x_i)) \frac{\partial P(x_i)}{\partial p_j} = 0,$$

the normal equations for this problem.

Only if the errors are small compared to the peak amplitude of the Gaussian ($A \gg \mu$), one can approximate the above conditions by the linear term of the Taylor series

$$a_i - P(x_i) \approx dP = \sum_{k=1}^{3} \frac{\partial P(x_i)}{\partial p_k} dp_k.$$

This condition is fulfilled for high S/N. The linearisation yields

$$\sum_{i=1}^{N} \sum_{k=1}^{3} \frac{\partial P(x_i)}{\partial p_k} \frac{\partial P(x_i)}{\partial p_j} \, dp_k = 0; j = 1, 2, 3.$$

The $3 \times 3$ matrix $\mathbf{E}$ contains the coefficients to the linearised normal equations

$$E_{j,k} = \sum_{i=1}^{N} \frac{\partial P(x_i)}{\partial p_k} \frac{\partial P(x_i)}{\partial p_j} \approx \frac{1}{h^2} \int_{-\inf}^{\inf} \frac{\partial P(x)}{\partial p_k} \frac{\partial P(x)}{\partial p_j} \, dx, \tag{2.2}$$

which can be approximated by an integration over $x$ if the sampling $\{x_i\}$ is uniform (i.e. constant pixel size $h$) and the peak of the profile is completely covered by the data; cf. Kaper et al. (1966) for a proof of the validity of the approximation. For any differentiable function $F(p_1, p_2, p_3)$, its variance is given by

$$\mu^2(F) = \mu^2 \sum_{j=1}^{3} \sum_{k=1}^{3} E_{j,k}^{-1} \frac{\partial F}{\partial p_j} \frac{\partial F}{\partial p_k}.$$

The integrals and, therefore, the matrix $\mathbf{E}$ are easily evaluated as is the inverse matrix $\mathbf{E^{-1}}$. In this way, one obtains

$$\mu^2(A) = \mu^2 E_{1,1}^{-1} \approx \frac{2A^2}{\pi\sigma} \left(\frac{h\mu}{A}\right)^2,$$

$$\mu^2(\sigma) = \mu^2 E_{2,2}^{-1} \approx \frac{2\sigma}{\pi} \left(\frac{h\mu}{A}\right)^2, \tag{2.3}$$

$$\mu^2(x_0) = \mu^2 E_{3,3}^{-1} \approx \frac{2\sigma}{\pi} \left(\frac{h\mu}{A}\right)^2.$$

The S/N in each individual pixel of the profile is $(S/N)_i = P(x_i)/\mu$. Summing quadratically over $i$ and replacing the sum by an integral (as in 2.2), the total S/N of the profile is

$$(S/N)^2 = \frac{\pi\sigma}{h^2} \cdot \left(\frac{A}{\mu}\right)^2. \tag{2.4}$$

Here $N_{\text{eff}} := \pi\sigma/h^2$ can be interpreted as an effective number of pixels within the profile. $A/\mu$ is the S/N at the peak. Thus, (2.3) and (2.4) yield

$$\frac{\mu^2(A)}{A} = \frac{\mu^2(\sigma)}{\sigma^2} = \frac{\mu^2(x_0)}{\sigma^2} \approx \frac{2}{(S/N)^2}. \tag{2.5}$$

The commonly used FWHM is related to the $\sigma$ of a Gaussian by

$$\sigma = \frac{\text{FWHM}}{\sqrt{8\ln 2}}.$$

That can easily be shown by evaluating the definition of the FWHM $:= x_2 - x_1$ where $x_2$ and $x_1$ are those x-values for which the exponential is at half the peak value. Replacing $\sigma$ in (2.5) leads to

$$\frac{\mu^2(A)}{A^2} = 8\ln 2 \frac{\mu^2(x_0)}{(\text{FWHM})^2} = \frac{\mu^2(\text{FWHM})}{(\text{FWHM})^2} \approx \frac{2}{N_{\text{eff}} \cdot (S/N)_{\text{peak}}^2}. \tag{2.6}$$

The requirements of this derivation, which are a large peak S/N, a constant pixel size, a completely sampled peak, small pixels (i.e. $h \ll \text{FWHM}$) and a Gaussian error distribution, are met for many astronomical data sets. Equation (2.6) confirms the intuition that the attainable spatial resolution scales linearly with the S/N. Adaptive optics also increase the resolution as they decrease the width of the PSF which here corresponds to the value of FWHM. Another possible error source is the algorithm used to fit the spatial profile. Because the fitting of a single Gaussian is conceptually simple as no parameter degeneracy and local minima are expected, this is not a serious issue. Nevertheless, two standard fitting routines were tested and their results compared: a Levenberg-Marquardt non-linear least-squares method (`mrqmin`) and a simplex algorithm (`amoeba`), cf. Sect. B.2, both taken from the Numerical Recipes, Press et al. (2002). Differences in the fitted parameters were two orders of magnitude below the values obtained with Eq. (2.6). Hence, algorithm discrepancies are neglected henceforth.

### 2.4.2 Small spatial profile widths

Although the formal errors of Eq. (2.6) are in good agreement with simulations (see below in this section), the requirement of small pixels (i.e. $h \ll$ FWHM) may be violated for some data sets. Depending on the seeing at the time of observing, the quality of adaptive optics' correction and the instrument design, the width of the spatial profile can be smaller than a few pixels or even smaller than a single pixel. Monte-Carlo simulations have been performed to check the influence of S/N and sampling on the fit-accuracy. A Gaussian profile with amplitude $A$, sampled at $N$ pixels (with the peak being at the central pixel) was generated, random Gaussian noise $\mu$ added at a specific S/N, i.e. $A/\mu = (S/N)$. Then, a single Gaussian was fitted and the best-fitting parameters were compared to the input values. This procedure was repeated $10^4$ times for the same parameter set. The median values of the $10^4$ values of $A, x_0, \sigma$ serve as an estimation for the fitted parameters. The standard deviations represent the errors within them. First, these simulations were performed for fixed $A, x_0, \sigma$ and $N$ but the S/N was varied in order to verify the validity of equation (2.6). Figure 2.3 shows both the predicted values (solid line) and the simulated ones (data points). They are clearly in good agreement with each other. As a second step, another set of simulations was performed for fixed $A, x_0, \sigma$ and high S/N but, this time, the number of sampling points $N$ was varied. As can be seen from Fig. 2.3, the fit accuracy does not depend on $N$ as long as the pixel size is small compared to the width of the profile (i.e. $N/\sigma > 1$). This is again in good agreement with Eq. (2.6). As a conclusion
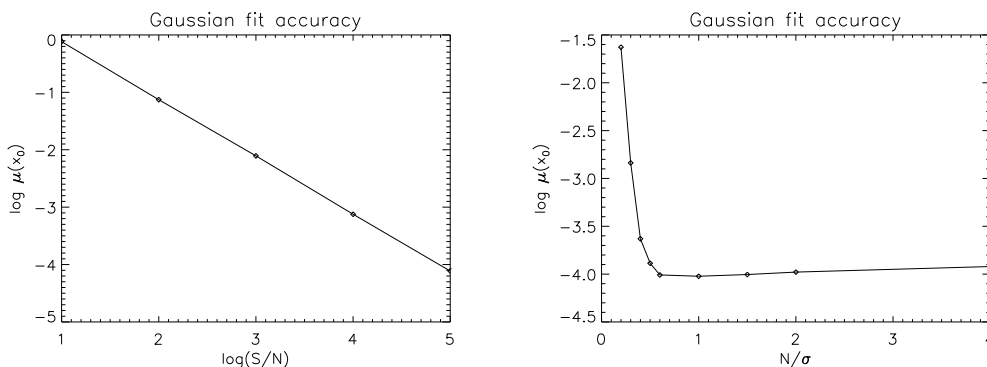


Figure 2.3: The data points show the standard deviation of $10^4$ Monte-Carlo simulations, see text. The left panel features simulations with variable S/N whereas in the right one the pixel sampling was varied. The values obtained with Eq. (2.6) are shown as a solid line in the left graph.

one sees that the width of the spatial profile is not important as long as it is not below about 1.4 pixels sampling the FWHM (equivalent to 0.6 pixels per $\sigma$ in Fig. 2.3). At lower values, the accuracy declines steeply. The same applies equivalently to the accuracy of the width of the profile. Apart from the influence on the spatial resolution small profile widths negatively affect some steps of data reduction, cf. Chap. 3.

### 2.4.3 Non-Gaussian profiles in Gaussian fitting

If the spatial profile is a priori known to have a non-Gaussian shape, a different functional form may be fitted for. However, in most cases, the assumption indeed is Gaussian, but (small) deviations hereof cannot be ruled out. One then needs to know to what extent such deviations influence the fitting process. Again, Monte-Carlo simulations were conducted to investigate this. All parameters $A, x_0, \sigma, N$ and S/N were now kept constant, but a constant value was added to all data points with $x \leq x_0$. In this way an asymmetric

profile was created. The degree of asymmetry was varied. Although in reality, there could be other distortions of the spatial profile, this scenario shows important points

- there is a deviation of the fitted parameters from the input values,

- this deviation is small for realistic profiles ($< 1\,\%$),

- this deviation is *constant* as long as the profile shape is constant.

The last point is the most important one. Since spectro-astrometry uses centroid and width *variations* with wavelength only, a constant offset does not influence the results at all. As long as the shape of the spatial profile is constant with time and wavelength there is no impact of a non-Gaussian profile on spectro-astrometry when using Gaussian fitting. Naturally, that holds only if the deviations from a Gaussian are not too large.

### 2.4.4   M-estimators

If $\rho(x_i, \Theta)$ is a probability density function of data parameterised by $\Theta$, the minimisation of $\sum_{i=1}^{n} \rho(x_i, \Theta)$ is called M-estimation and the solutions thereto are called M-estimators. The class of M-estimators in statistics is large, and many standard statistical estimators can be shown to be M-estimators.

Another way to extract the centroid and width spectra from the longslit spectrum is to evaluate standard statistical estimators of the spatial profiles. The most simple is the *weighted arithmetic mean* to represent the centroid and the *weighted standard deviation* to represent the width

$$\mathcal{C}(x_i) = \frac{\sum_{j=1}^{N} j \cdot P(x_j)}{\sum_{j=1}^{N} P(x_j)}, \tag{2.7}$$

$$\mathcal{W}'(x_i) = \left( \frac{\sum_{j=1}^{N} P(x_j) \cdot |j - \mathcal{C}(x_i)|}{\sum_{j=1}^{N} P(x_j)} \right)^{1/2}. \tag{2.8}$$

Here $\mathcal{C}(x_i)$ and $\mathcal{W}'(x_i)$ are the centroid position and width of the profile of the $x_i$th wavelength bin. $N$ is the number of pixels of the spatial profile that have been used to extract both quantities. The weights $P(x_j)$ are the intensities of the individual pixels. Since the number of sampling points $N$ is relatively small, the *biased* estimator $\mathcal{W}'(x_i)$ should be replaced by the unbiased weighted standard deviation $\mathcal{W}(x_i)$

$$\mathcal{W}(x_i) = \left( \frac{\sum_{j=1}^{N} P(x_j)}{\left( \sum_{j=1}^{N} P(x_j) \right)^2 - \sum_{j=1}^{N} P(x_i)^2} \cdot \sum_{j=1}^{N} P(x_j)|j - \mathcal{C}(x_i)|^2 \right)^{1/2}. \tag{2.9}$$

The above transition from the biased towards the unbiased estimator is equivalent to the transition of the denominator in the simple standard deviation from $N$ to $N-1$ and avoids a systematic over- or underestimation of the true values (it should be emphasised that the formulas shown above are only *estimators* of the (weighted) standard deviation).

Although both statistical quantities are widely used in astronomy they are not robust to outliers. I am, however, confident that outliers have been removed beforehand by the bad pixel detection, cf. Sect. 3.2. Nevertheless, I compare the results obtained with these non-robust estimators to those of robust estimators. This allows to check for undiscovered residual outliers. The theoretical background on robust statistics can be found e.g. in Huber (1981), Hampel et al. (1986) and Rousseeuw and Leroy (1987) and is too extensive

to be presented here. As a robust estimator of location I use Tukey's biweight, see again Huber 1981 for details. It can be roughly outlined as follows: The function $\zeta(z)$ is defined for $|z| \leq a$ by

$$\zeta(z) = z \left( 1 - \frac{z^2}{a^2} \right)^2, \tag{2.10}$$

and it is zero otherwise. Here, it is $z = (x - T_n)/S_n$ where $x$ is the data sample and $S_n$ a robust estimator of scale. The value of $T_n$ for which $\sum_i \zeta_i = 0$ is the desired result. The determination of the biweight works iteratively. If one chooses $S_n$ to be the median absolute deviation[1], the denominator is an estimator of the standard deviation of the sample. The parameter $a$ in Eq. (2.10) determines the shape and cut-off of the weighting function, see Fig. A.1 in the appendix. M-estimators with such weighting functions are called *redescending*.

I here use both the non-robust estimators and Tukey's biweight to extract the centroid and width spectra for simulated and real data. Analysing the results I find that robust estimators indeed are far better if no bad pixel detection has been performed beforehand. However, after bad pixel correction there is virtually no longer any difference. The comparison of the M-estimator results with those of the Gaussian fitting is depicted for a representative CRIRES exposure in Fig. 2.4. Although both methods in principle yield
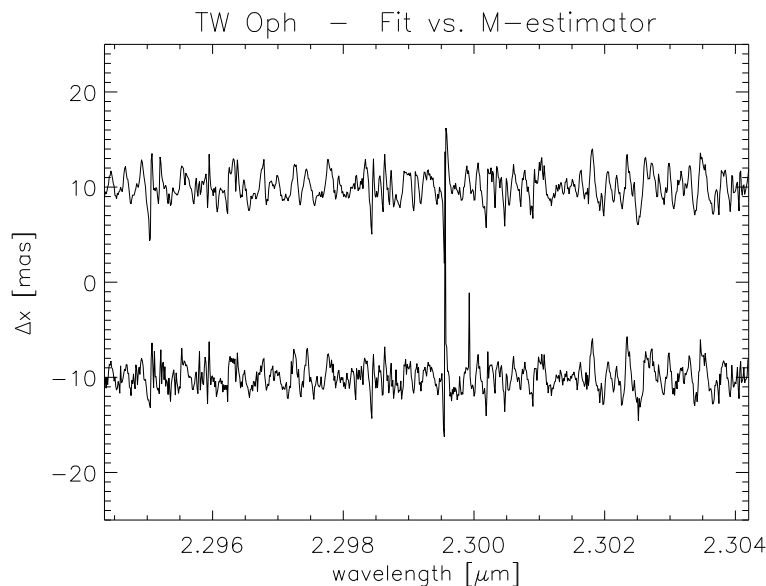


Figure 2.4: $\mathcal{C}(\lambda)$ extracted from a CRIRES TW Oph exposure using Gaussian profile fitting (upper curve) and Tukey's biweight (lower curve). The features in the spectrum are visible in both cases but the pixel-to-pixel scatter is larger for the M-estimator measure.

the same results, Gaussian fitting has a lower scatter in the pseudo-continuum between the CO lines. Thus, henceforth, all results presented in this thesis have been obtained by Gaussian fitting.

### 2.4.5   Summary position/width spectrum extraction

The extraction procedure of the spectro-astrometric signatures is thoroughly treated in this section because it is crucial to quantify any error which can occur. However, it turned out

---

[1]which is defined by $\mathrm{MAD} = 1.4826 \cdot \mathrm{med}_i \left( |i - \mathrm{med}_j(j)| \right)$

that the error associated with the extraction itself is negligible and that spatial resolution is theoretically limited by the PSF width and by the S/N. Outliers in the spatial profiles, i.e., bad pixels, need to be removed before the extraction to achieve optimal results. Gaussian fitting is used for spectro-astrometric extraction as the noise in $\mathcal{C}(\lambda)$ and $\mathcal{W}(\lambda)$ is lower than in case of M-estimator usage. Some spectro-astrometric studies on different object types have been published so far, cf. Sect. 2.10. Gaussian profile fitting, e.g. (Whelan et al., 2005), and a simple weighted mean, e.g. (Pontoppidan et al., 2008), have been used for extraction. However, no serious discussion on the performance of the methods has been conducted there. Massa and Evans (2008) only state that they compared Gaussian fitting with the weighted mean and that they found no relevant differences. Though limited in significance with respect to different extraction methods, those publications do not contradict our findings.

## 2.5   Simulating spectro-astrometric signatures

Any scientific analysis of the extracted spectro-astrometric spectra requires the comparison of the observed spectra with simulations, e.g., to constrain the physical models that possibly induce those signatures. Section 2.2 introduced the basic principle of object mapping. With this it is easy to calculate the centroid position and profile width for arbitrary object configurations. Brannigan et al. (2006) were the first to simulate spectro-astrometric signatures of a binary source. I improved this method to be able to simulate arbitrary object configurations. Seeing and diffraction are ignored and, thus, the system consists of two point sources. They are assumed to have intensities $I_1$ and $I_2$ and identical SEDs $f(\lambda)$. Then, with Eq. (2.1), the centroid displacement $\mathcal{C}$ is given by

$$\mathcal{C}(\lambda) = \frac{\Delta x}{2} \cdot \frac{I_1 f(\lambda + \Delta\lambda(y)) - I_2 f(\lambda - \Delta\lambda(y))}{I_1 f(\lambda + \Delta\lambda(y)) + I_2 f(\lambda - \Delta\lambda(y))} \tag{2.11}$$

with $\Delta\lambda(y) = K\,\Delta y$. In the next step I allow for different SEDs of the two components (i.e. $f_1(\lambda)$ and $f_2(\lambda)$) and abandon the point source assumption. Instead, intensity distributions $I_1(x,y)$ and $I_2(x,y)$ replace the constant intensities. The former, in fact, are multiplications of the constant intensity of the target component with the PSF: $I_1(x,y) = I_1 \cdot \mathrm{PSF}(x,y)$. The coordinates $(x,y)$ are the spatial and dispersion direction in the slit plane, respectively. The width of the PSF summarises the atmospheric seeing as well as the influence of adaptive optics. The slit width of the spectrograph is considered indirectly by setting a maximum value for $\mathrm{d}y$. This generalisation leads to

$$\mathcal{C}(\lambda) = \frac{\sum_{i=1}^{2} \int \int x\, I_i(x,y)\, f_i(\lambda + \Delta\lambda(y))\, \mathrm{d}x\, \mathrm{d}y}{\sum_{i=1}^{2} \int \int I_i(x,y)\, f_i(\lambda + \Delta\lambda(y))\, \mathrm{d}x\, \mathrm{d}y}. \tag{2.12}$$

The integration performs a continuous summation over $(x,y)$ in the slit plane whereas the summation adds up the contributions of the two components. Any target configuration can be thought of as composed of $N$ point sources, each with its own intensity and SED. Thus, in Eq. (2.12), one can replace the upper summation limit with $N$. Because the SEDs $f_i(\lambda)$ do not have an analytic functional form, the integral cannot be evaluated analytically. A proper replacement of the integrations with summations allows for a discrete calculation of the position spectrum. The impact of velocity fields can be integrated by using appropriately modified SEDs, e.g., by applying the Doppler shift.

Although perfectly viable, I use another method to obtain the spectro-astrometric signatures caused by an astrophysical source: first, a two-dimensional long-slit spectrum is constructed. Then, the same extraction procedure can be applied to the simulated data

which is used on observed data, see Sect. 2.4:

First, the source is constructed as described above: $i = 1, \ldots, N$ point sources with intensities $I_i$ and spectral energy distributions $f_i(\lambda)$. A single point spread function $\text{PSF}(x, y)$ is supplied. If necessary a velocity field $v(x, y)$ is included by modifying the individual SEDs. The intensity of each point source is convolved with the PSF. For each point in the slit plane, the wavelength shift due to its off-centre position, cf. Eq. (2.1), is evaluated. Equivalently to Eq. (2.12), for each $x$-value, the product $I_i(x, y) \cdot f_i(\lambda + \Delta\lambda(y))$ is evaluated and then summed over $i$ and integrated over $y$ yielding the long-slit spectrum component $L(x, \lambda)$ – with $(x, \lambda)$ being the spatial and dispersion direction in the detector plane. This has to be repeated for each wavelength bin of the input SEDs. Photon shot noise[2] is then added to every pixel at the desired S/N. For a simple binary source the difference spectrum (i.e. the difference of both SEDs) can be cross-correlated to $\mathcal{C}(\lambda)$ and $\mathcal{W}(\lambda)$ to detect signatures which are only slightly above the noise level. For more complex sources the SED extracted from the simulated longslit spectrum should be used for cross-correlation. This SED is the replacement for the difference spectrum mentioned before. The spatial profile of the simulated data is determined by a weighted projection of the 2D-PSF onto the spatial axis. The integration over $x$ in Eq. (2.12) actually performs the transition from the two-dimensional long-slit spectrum to the one-dimensional position spectrum $\mathcal{C}(\lambda)$. This is realised here by the extraction procedure.

**Discussion:** Both methods to simulate spectro-astrometric signatures are equivalent and, hence, yield identical results. Nevertheless, I use the second one for one advantage: since the procedure to extract $\mathcal{C}$ and $\mathcal{W}$ can identically be applied, any systematic error equally affects both simulated and observed data. The simulations do not include any instrumental effects such as, e.g., tilted and/or distorted spectra. Thus, these effects need to be removed from the observed data before comparison with simulated data, cf. Chap. 3.

## 2.6   Instrumental artefacts

This section deals with instrumental artefacts in $\mathcal{C}(\lambda)$ and $\mathcal{W}(\lambda)$ and methods to remove those features in order to possibly attain the full theoretical resolution limit.

### 2.6.1   Origin, shape and amplitudes

If a truly point-like object is observed, no spectro-astrometric signatures are expected to occur. Thus, $\mathcal{C}(\lambda)$ and $\mathcal{W}(\lambda)$ should be equal to zero for all $\lambda$. This is indeed true as long as the PSF is symmetric with respect to the spatial axis in the slit plane. Using the simulations described in Sect. 2.5 allows for a study of non-symmetric cases. First, the PSF is simply changed to an elliptical 2D-Gaussian which is inclined to the spatial axis by $\phi$. The centre of the PSF is chosen to be at $x_c$. Hence, one half of the PSF ($x \leq x_c$) is offset from the slit centre to one side resulting in, e.g., a redshift of the SED according to Eq. (2.1). The part corresponding to $x \geq x_c$, in turn, then leads to a blueshift. This translates to a redshift (blueshift) in the longslit spectrum for the lower (upper) part of the spatial axis. This effect can also be regarded as a tilting of the spectral lines with respect to the spatial axis on the detector, i.e., the line of constant wavelength is no longer orthogonal to the dispersion direction. The impact on $\mathcal{C}(\lambda)$ and $\mathcal{W}(\lambda)$ is obvious: at each spectral feature a P-Cygni-like profile appears in the centroid and a W-like feature in width. Figure 2.5 illustrates this. The parameters have been chosen such that the artefacts

---

[2]Photon shot noise means that the noise is proportional to the square root of the signal. This distribution is a Poisson distribution and approaches a normal distribution for large signal amplitude.
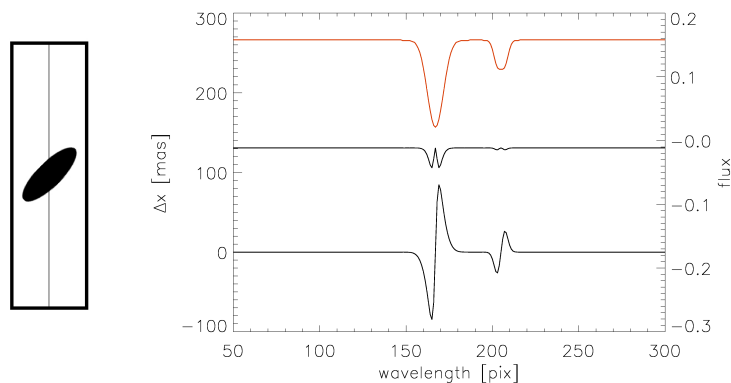
Figure 2.5: Spectro-astrometric artefacts (right panel) simulated for a point source with an elliptical PSF (left panel). In the right subplot, the curves are plotted equivalently to Fig. 2.2. See text for details.

exactly match the target-induced kinematic features of Fig. 2.2. This shows that artefacts and real signatures may be similar or even identical – see next section. Such artefacts always occur if the PSF is asymmetric with respect to the spatial slit axis. The exact shape and amplitude of the artefacts, however, will vary with the PSF. Furthermore, the optical setup of the instrument, the PSF width and the slit width influence the amplitude of the artefacts. Equation (2.1) confirms this because $K$ (instrumental characteristic) and $dy$ are responsible for the amplitude of the artefacts. The larger the slit width the larger $dy$ can get – at least as long as the seeing is larger than the slit width. Depending on these parameters, the amplitudes of the artefacts can exceed the target-induced signatures. Practically, any real telescope and instrument does not have a perfectly symmetric PSF. Aberrations can be caused by the telescope optics itself (e.g. astigmatism leads to elliptical PSFs) or can be a result of active/adaptive optics, cf. Brannigan et al. (2006). If the latter is the cause, the PSF will even be time dependent and the artefacts will also change with time. Since it is obvious that artefacts need to be removed before a useful analysis of centroid and width spectra can be conducted I now discuss the procedure in detail.

### 2.6.2 Countermeasures

The problem of spectro-astrometric artefacts has been realised before by several authors, cf. Bailey (1998) and particularly Brannigan et al. (2006). However, so far there have been only two suggestions to avoid and/or remove artefacts:

First, the usage of a slit width significantly smaller than the PSF width reduces the amplitude of the artefacts simply because the maximum of $dy$ in Eq. (2.1) is restricted to smaller values than for larger slit widths. The downside of this is the loss of light and, hence, a smaller S/N which leads to a lower spatial resolution. Second, the subtraction of position spectra obtained at anti-parallel slit orientations is supposed to remove artefacts. Real spectro-astrometric signatures change sign when rotating the spectrograph by 180° (with respect to the object on the sky) whereas artefacts do not. Thus, such a subtraction would in principle remove any instrumental artefacts as long as these remain constant. In fact, the last point is the critical one: exposures which are taken non-simultaneously may well have different artefacts. The internal conditions of the spectrograph can change with time (e.g. mechanical or thermal changes), the seeing amplitude varies and the shape of the PSF can change, particularly with active/adaptive optics. Thus, one would need to obtain exposures contemporaneously at anti-parallel slit angles. This requires special

instrumentation which does not yet exist, but which is currently developed in another project in my research group (Wiedemann G., private communications). In this work we, therefore, use the anti-parallel subtraction method only as a first-glance-tool. It also is a means to monitor the changes in observing conditions with time. Finally, taking exposures at anti-parallel slit angles does not waste observing time as the extracted $\mathcal{C}(\lambda)$ and $\mathcal{W}(\lambda)$ can be co-added (after changing the sign) to increase the S/N.

I here present a new procedure with the aim of reaching the full S/N-limited spatial resolution. The basic assumption is that any instrumental effect can be condensed into the PSF. That means that whatever happens to the incident light beam on its way to the detector can be described by an effective PSF, but see Sect. 3.2.3.4 on image distortion for an exception.

**The method:** Some spectro-astrometric spectra $\mathcal{C}(\lambda)$ and $\mathcal{W}(\lambda)$ are supplied. The artefacts in both quantities are to be removed. First, a true point source with an input SED is assumed as well as some PSF. The corresponding $\mathcal{C}(\lambda)$ and $\mathcal{W}(\lambda)$ spectra are simulated as described in the previous section. Then, the PSF configuration is varied and the simulated signatures are compared to the initial ones. The PSF of the best-fitting scenario is the best description for the instrumental profile. The artefacts which are obtained using the best-fitting PSF are subtracted from the initial artefacts. As a measure for the goodness-of-fit, the $\chi^2$ measure

$$\chi^2 = \frac{1}{N} \sum_{i=1}^{N} \left( \frac{(\mathcal{C}_{\mathrm{sim}}(i) - \mathcal{C}_{\mathrm{init}}(i))^2}{\sigma_{\mathcal{C}}^2} + \frac{(\mathcal{W}_{\mathrm{sim}}(i) - \mathcal{W}_{\mathrm{init}}(i))^2}{\sigma_{\mathcal{W}}^2} \right) \tag{2.13}$$

is evaluated, compare also Sect. B.2. The total number of wavelength bins is denoted by $N$, $\mathcal{C}_{\mathrm{sim}}$ contains the simulated artefacts and $\mathcal{C}_{\mathrm{init}}$ contains the initial artefacts in $\mathcal{C}$. The same applies to the $\mathcal{W}$-quantities. The denominator $\sigma$ is the total error of the numerator. In case of simulated data the error is given by Eq. (2.6). When dealing with observed data there may be additional error sources, cf. Chap. 3. The individual error contributions are summed quadratically to yield $\sigma$. Because the PSF is two-dimensional a parametrisation has to be chosen for the fitting algorithm. The number of possible configurations is way to large without a parametrisation. When working with real data one chooses the observed SED as input SED to the artefact simulation. If simulated data is processed, of course, the input SED has to be used. After the subtraction of the simulated artefacts, the source modelling can be performed, see the next section.

**Discussion:** Several points of this procedure can be criticised. It is not strictly true that any instrumental influence can be summarised by an effective PSF. The SED extracted from an observed longslit spectrum will likely be used to simulate the artefacts. This SED is, however, not identical to the true target SED as it was shown that the impact of asymmetric PSFs can also be interpreted as a tilting of the spectral lines. In fact, the artefact fitting algorithm would have to vary both, the PSF *and* the input SED, even if the changes in the SED would only be small. Fitting both quantities is not viable since the number of free parameters is so large that any $\mathcal{C}(\lambda)$ and $\mathcal{W}(\lambda)$ can be "corrected" to a zero line. Because the difference between the extracted and the true SED does depend on the unknown PSF it is unclear which constraints should be applied to the SED fitting process. As consequence, the program code does not fit for the true SED at all and only varies the PSF. Furthermore, the parameterisation of the PSF during fitting is critical. Without a priori information about the PSF shape, an elliptical parameterisation is used with the free parameters being the PSF width $P$, the angle of the ellipse with respect to the slit axis $\phi$ and the ratio of the major to the minor axis $a/b$. The intensities are assumed to obey a Gaussian form in both axes $a$ and $b$. A more flexible approach is to use a central

circular PSF of Gaussian shape and smaller circular satellite Gaussians in the vicinity. The position of the satellites and the intensities of all PSF components are then varied during the fitting process[3]. The latter can easily lead to a large parameter space requiring enormous computing time. Hence, a limitation of two satellites is used here. The choice of parameterisation should also be done depending on the shape of the input artefacts in both $\mathcal{C}(\lambda)$ and $\mathcal{W}(\lambda)$. Furthermore, the initial assumption of a point source can be invalid. The aim of a spectro-astrometric study will most likely be to detect a structure within the target. The best way to avoid this problem is to use only telluric lines for the fitting of the instrumental profile. If there are not enough telluric lines the point source assumption can still give good results if the true signatures are of different shape than the artefacts, e.g., in case of spatial signatures as in Fig. 2.1. On the contrary, kinematic signatures may be similar or even identical in shape to artefacts and can, thus, completely mislead the fitting procedure. The usage of a gas absorption cell can also provide the lines that are necessary for the removal process. In the worst case, the anti-parallel subtraction method is the only remaining possibility to reduce artefacts.

**Results:** The code is tested with simulated longslit spectra: some SED and PSF configuration are chosen together with an arbitrary S/N. The simulated $\mathcal{C}(\lambda)$ and $\mathcal{W}(\lambda)$ (containing artefacts) are used as input to the removal algorithm. Ideally, the initial PSF configuration should be recovered and there should not be any residual artefacts after subtraction. The result is perfect for high S/N for both an elliptical PSF and a central circular PSF component with two lower intensity satellite circular components, see Fig. 2.6. The strong gradients in the $\chi^2$-landscape guarantee that the fitting algorithm
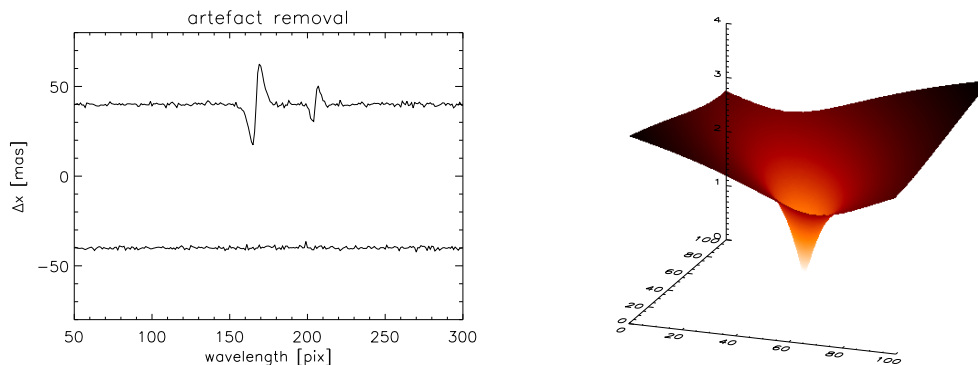


Figure 2.6: The left plot shows $\mathcal{C}(\lambda)$ before and after artefact removal. A point source was used together with an elliptical PSF. The right plot images the $\chi^2$-landscape of the removal procedure for the $a/b$, $P$ sub-parameter space, i.e., for constant $\phi$. The units on the x- and y-axis are arbitrary. The z-axis shows the logarithm of the $\chi^2$ value which is as low as 0.4 for the best-fit. The two missing sub-parameter space plots look very similar with respect to the strong convergence towards the correct solution. The S/N was 100 and the noise can be seen in the $\mathcal{C}(\lambda)$ spectra. After removal, there is no residual artefact above the noise level.

does reliably converge, see Sect. B.2 for the algorithms which were used. The residual artefacts are practically identical to zero for signal-to-noise ratios above ten. The results are almost identical for a two-satellite configuration together with a two-satellite parameterisation. More interesting is the case for which a wrong parameterisation is chosen, e.g., an elliptical PSF whereas the true PSF is a two-satellite configuration. In reality,

---

[3]leaving ten free parameters for two satellites, namely width and intensity for the central and satellite components (i.e. 6 parameters) and, additionally, distance to the central component and position angle for each satellite (i.e. 4 parameters)

the true PSF configuration will often be unknown. One expects that as long as the chosen parameterisation is similar to the true PSF the results will be satisfactory. That is indeed true, e.g., an elliptical parameterisation leads to good removal results if the true PSF has a bright circular central Gaussian and one satellite along the major axis of the ellipse. Figure 2.7 points out the problems when using in inadequate parameterisation. The left subfigure only uses $\mathcal{W}(\lambda)$ to evaluate the $\chi^2$-measure and suggests a very good fit



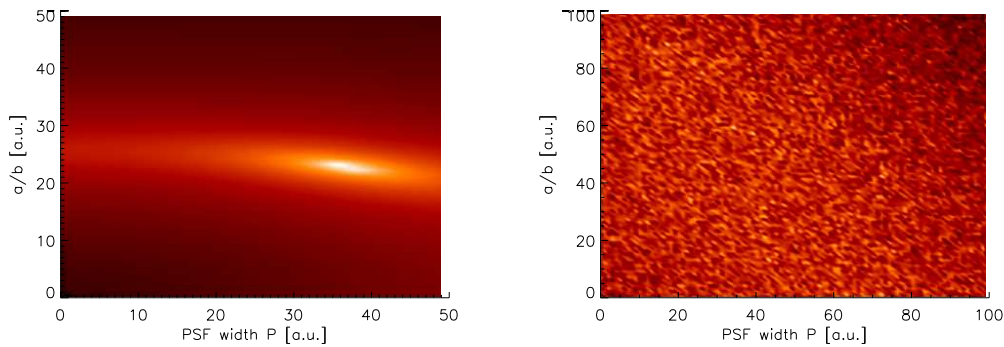Figure 2.7: As in Fig. 2.6, the $\chi^2$-landscape is shown for an elliptical parameterisation and a two-satellite input PSF. Here, brighter regions symbolise lower $\chi^2$-values with white colour standing for an almost perfect fit. The left subfigure depicts the case that only $\mathcal{W}(\lambda)$ is used to evaluate the $\chi^2$-value. The right plot shows the results for the same scenario but uses both, $\mathcal{C}(\lambda)$ and $\mathcal{W}(\lambda)$. Both plots show the same parameter space, the units on the axis are arbitrary.

whereas the full calculation (Eq. 2.13) reveals that the parameterisation is utterly useless. The explanation for this is that two different phenomena may lead to similar $\mathcal{C}(\lambda)$ but have completely different $\mathcal{W}(\lambda)$ or vice versa. This emphasises the need to always use both quantities $\mathcal{C}(\lambda)$ and $\mathcal{W}(\lambda)$ when judging the goodness of artefact removal and source modelling.

**Summary:** It was shown that the removal of instrumental artefacts in $\mathcal{C}(\lambda)$ and $\mathcal{W}(\lambda)$ is feasible. A parameterisation of the PSF configuration is necessary. The choice of an advantageous parameterisation is critical and the most difficult step as the true PSF is often unknown for real data. A structured source featuring kinematic signatures can complicate the removal procedure or even render it useless if one relies on the spectral features of the target itself. Therefore, the presence of telluric lines in the spectrum is important because they are only affected by instrumental effects. Gas cell reference lines serve the same purpose as telluric lines: they contain the instrumental profile and are of advantage if no telluric lines are present and the source is expected to result in kinematic signatures. However, the usage of a gas cell does not improve the artefact removal compared to the usage of telluric lines because the instrumental profile will most likely be constant over the wavelength range of a detector chip. The application to real data will be discussed in Chap. 4. The presence of artefacts and residual artefacts even after the removal procedure emphasises that it is not possible to give a reliable error bar on the spectro-astrometric quantities. A possible estimator on the error is the rms-amplitude of $\mathcal{C}(\lambda)$ and $\mathcal{W}(\lambda)$ in a continuum region of the spectral energy distribution[4].

---

[4]but note, that the S/N is lower in spectral absorption lines compared to the continuum

## 2.7   Source modelling

The final step in the spectro-astrometric analysis is the modelling of the source configuration. After the removal of instrumental artefacts, ideally, only real signatures caused by the target are left. Simulating various source configurations allows for an identification of the best-fitting scenario. The problem here is similar to the one in Sect. 2.6.2: The goodness-of-fit is again evaluated by a $\chi^2$-measure and one also needs to restrict oneself to a certain class of source configurations. One simply cannot test for any possible configuration. First, one tries to simulate scenarios that are expected a priori, e.g., spots on a stellar surface. If, however, the observed signatures differ significantly from the simulated ones, other configurations should be considered, e.g., a disk around the star.

There is an important problem in constraining the source configurations, i.e., *model degeneracy*. This means that two or more different target configurations lead to identical $\mathcal{C}(\lambda)$ and $\mathcal{W}(\lambda)$. Two different kinds of degeneracy have to be distinguished. First, there is the *principle* degeneracy which means that the method of spectro-astrometry itself is responsible for the indistinguishability and, thus, the different scenarios cannot be disentangled by spectro-astrometry alone. Second, there is the *observational* degeneracy. Here, the observing scheme is the cause: since the data at a single slit orientation only probes structures in one dimension, depending on the source structure, a certain minimum number of slit orientations is necessary to ensure a detection. Using less orientations results in a model degeneracy. Another example for observational degeneracy is the lack of sufficient wavelength coverage. Two different phenomena may have nearly identical difference spectra in a limited wavelength range. However, it is more unlikely that there are no significant differences when considering a larger wavelength range. This stresses the importance of a careful planning of the observing runs.

The process of source modelling is illustrated here with the example of stellar surface spots, as this will be the application in Chap. 4: Synthetic model spectra are calculated with the parameters of the target star without spots. Then, model spectra at lower/higher effective temperature are obtained to represent cool/hot spots. The spectro-astrometric signatures are evaluated using our code with an appropriate geometric model of the spotted star. This geometry is then varied and the best-fit to the observed $\mathcal{C}(\lambda)$ and $\mathcal{W}(\lambda)$ spectra at all observed position angles describes the most likely true configuration, within the limits set by possible model degeneracies. The parameter set, i.e. effective temperature, surface gravity, mass, chemical abundances, turbulence velocities etc., of the initial background atmosphere is either known beforehand or has to be obtained by fitting synthetic spectra to the observed data. In practice, there is the problem that the observed SED is a combination of the SEDs of the different components of the target; for the example case, the full-disk SED is observed and there is no way to observe the SED of the star without spots (if there are spots on the surface). Thus, the fitting of the observed SED with synthetic spectra needs to heed this issue: in the above case, an ansatz would be to fit the observed SED by a linear combination of two synthetic models with different stellar parameters, as, e.g., effective temperature. This would, ideally, yield the temperature of the stellar background atmosphere, the spot temperature and the total spot coverage factor – assuming that all spots do have the same temperature. Then, the best-fitting pair of SEDs is used within the simulation of the spectro-astrometric signatures, varying the spot geometry. When studying this procedure in detail, there are several problematic issues: the above ansatz may not be strictly valid as, e.g., spots caused by convection cells may have different SEDs compared to standard stellar atmospheres at lower/higher effective temperature; furthermore, the synthetic spectra even may not describe the spotless target star correctly. These model uncertainties directly translate into uncertainties in the best-

fitting source configuration. For example, very precise synthetic spectra of cool (super-) giants are not yet available, cf. Lançon et al. (2007a), as the physical processes taking place in their atmospheres are very complex. In order to account for these problems, a simplified method of source modelling was applied to the giant star data in Chap. 4: a single synthetic spectra was fitted to the observed SED, varying only the effective temperature and the surface gravity, using reasonable values for the other free parameters. Since good agreement with the a priori known effective temperature was achieved, this value was used for the background atmosphere on which cool/hot spots were placed. Using various spot geometries, spectro-astrometric signatures were then simulated in order to fit the observed $\mathcal{C}(\lambda)$ and $\mathcal{W}(\lambda)$ quantities.

Despite all of the above problems, the *detection* of structure within an astronomical object is possible with spectro-astrometry, even if the correct source configuration cannot be deduced reliably.

## 2.8   Computational issues

Parts of the data reduction software and all of the spectro-astrometric analysis code has been developed in the course of this thesis and was written in C. A short overview of the different modules of the C-code and some algorithms which have been applied is given in the appendix. Numerical stability was easy to ensure for all parts of the code. More problematic is, first, the amount of computing time required by the artefact removal procedure and, second, to guarantee the convergence of the various fitting processes if the code is to be applied semi-automatically to large data sets.

The fitting of the instrumental profile to remove artefacts from observed data requires large amounts of computational time for complex PSF parameterisations. The processing of a single exposure requires about an hour on a single Pentium 4 CPU. This time consumption was especially critical during the development phase of the code. As the data set used in this thesis consists of nearly 500 exposures, the total time consumption is large. Future observations which use the proposed NDIT=1 mode on bright targets will result in thousands of exposures. To achieve the current efficiency of the code, several calculation intensive parts were parallelised using the GPL-licensed parallelization standard *OpenMP*. It allows to distribute the work-load of, e.g., `for`-loops to different CPU cores or different CPUs using shared memory. Communication of different threads with each other is not possible with OpenMP. Since all spectro-astrometric analysis code was programmed from scratch, the implementation of OpenMP was easy and resulted in a scale factor of approximate 0.85 on Intel dual-core and quad-core CPUs. The scale factor describes the acceleration of the code for multiple CPUs: if the factor is one, two CPUs will need half the time of a single CPU; if the factor is zero, two CPUs will need as long as a single CPU. Some parts of the code could manually be distributed to separate computers. The individual results were then recombined at the end. This procedure ensured a scaling factor of one and allowed to use more than the four CPU cores of a standard quad-core computer. The overview $\chi^2$-landscapes, cf. Sect. 2.6.2, had to be calculated in this way as they are computationally very expensive. The processing of the individual exposures could also easily be distributed over several computers.

The second problematic issue is due to the fact that the exposures of a data set may vary significantly in several characteristics. The flux level can vary because of a changing sky transparency; changes in the read-out electronics may cause bad columns to change between exposures, etc. Such problems required some manual fine tuning of the input parameters of the code to enable the processing of the complete giant star CRIRES data set. This will be time-consuming for large data sets and, thus, a better robust automation

of the code will be necessary.

## 2.9   Summary on simulation results

In this thesis, spectro-astrometry is applied to the detection of stellar surface structures, cf. Chap. 4. The detection limits on cool/hot spots on the individual targets are listed in that chapter. Here, a more general image on the capabilities of the method is presented. Even though only the special case of spots on a stellar surface is evaluated, the set of possible configurations is large. Thus, some important sub-cases are studied here. First, a single spot scenario is considered. The slit of the spectrograph can always be oriented along the direction of the spot which leads to spectro-astrometric signatures of maximum amplitude in this direction and to no signatures at all in the perpendicular direction. Without loss of generality, the longitude of the spot also can be kept constant for the simulations as a change in longitude can be compensated by a rotation of the slit and a variation of the latitude[5] of the spot. To compare the signatures of a spot at different distances from the centre of the stellar disk requires the consideration of the azimuthal orthographic projection: an observer at the Earth only observes the projection of a stellar sphere to his detection plane. Thus, the area of the spot appears to be smaller at higher latitudes until it reaches zero for a very small spot at a latitude of $90°$. It can be shown that the apparent area $A_{ap}$ correlates with the true area $A_{tr}$ for a latitude of $\lambda$ as $A_{ap} = A_{tr} \cdot \sin(\lambda)$. This is only valid for very small areas for which the assumption $\lambda = $ const. is true over the whole area. As this relation is simple it is easy to transform projected area to true area. For convenience, in the following, only projected areas are considered. This motivates the definition of the *spot coverage factor e* as the projected percentage of the stellar disk which is covered by spots. Figure 2.8 depicts the *relative detectability* of spectro-astrometry
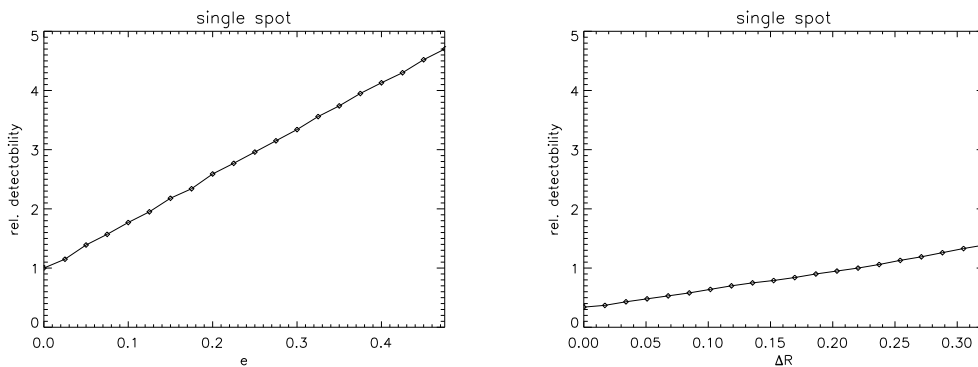


Figure 2.8: Relative detectability of a one spot scenario with respect to the reference configuration of $e = 0.1$ and $\Delta R = 0.2$. In the left plot, the spot size is varied, in the right plot, the distance of the spot centre to the centre of the stellar disk (measured in stellar radii) changes.

for the single spot case. *Relative* means that an initial spot configuration is defined to have a detectability of 1.0 and the limit for other spot configurations is compared to that value. The reference detection limit can then be calculated individually for different parameters as, e.g., signal-to-noise ratios and spectral contrast of the spot SED with respect to the background atmosphere SED. Figure 2.8 shows the detectability over spot size as well as

---

[5]Throughout this work, the *latitude* is counted from the centre of the stellar disk, regardless of the true equator of the star. The same applies to the *longitude*.

over the distance of the centre of the spot to the centre of the stellar disk[6]. The curve plotted in the figure was obtained by considering $\mathcal{C}(\lambda)$ and $\mathcal{W}(\lambda)$. Those detectability values do consider that spatial spectro-astrometric amplitudes for spots are smaller in $\mathcal{W}(\lambda)$ than in $\mathcal{C}(\lambda)$ and that the S/N-limit also is worse for $\mathcal{W}(\lambda)$.

Considering more complex spot configurations is not possible in a general way because the set of configurations is too large. The results of the simulations on one interesting case are depicted in Fig. 2.9: two spots are placed on the stellar disk; one in the northern
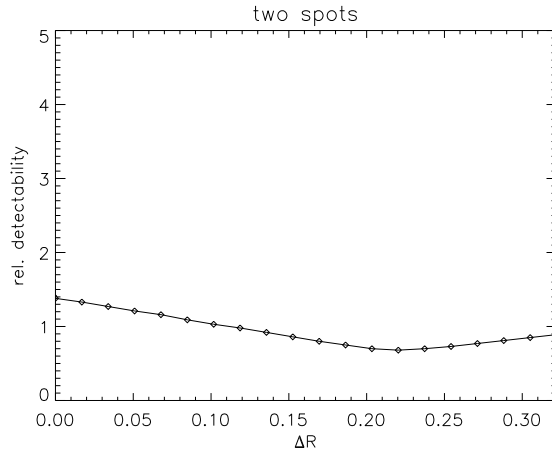


Figure 2.9: Relative detectability for a two spot scenario with the same reference scenario as in Fig. 2.8. The two spots reside at a longitude of zero and on different hemispheres. One spot is fixed, the position of the second one is varied.

hemisphere and one in the southern hemisphere. Both reside at a longitude of zero degree, the latitude of one spot is fixed and the latitude of the other spot is varied. Both spots have identical size and spectral contrast. If only the position spectrum is evaluated, two spots of identical parameters at contrary latitude, i.e., $\phi$ and $-\phi$, do not lead to any features. However, there are features in the width spectrum which are larger than for a single spot. This allows to detect such a two-spot scenario and to distinguish it from a single spot scenario, cf. Sect. 4.3.2. However, a detection of features showing up only in $\mathcal{W}(\lambda)$ is more difficult than detecting features in $\mathcal{C}(\lambda)$ because of the S/N-limitation, cf. Eq. (2.6).

## 2.10 Other work

During the last decade, several publications have appeared on spectro-astrometric studies of different astronomical objects. I present here a summary on those works which are the most important ones.

### 2.10.1 Binary detection

The modern concept of spectro-astrometry was first introduced by Bailey (1998). He proposed to use a CCD-equipped longslit spectrograph to measure the wavelength-dependence of the position spectrum. He noted the appearance of instrumental artefacts and suggested

---

[6]In these simulations, the stellar disk was taken to be two-dimensional with circular spots. However, for increasing $e$-values, the spot shape was changed in the way that for $e = 0.5$, one hemisphere of the star is completely covered by a spot and the other hemisphere is spot-free.

to obtain exposures at anti-parallel slit orientations to get rid of any instrumental effects. He observed a sample of 19 pre-main-sequence binaries at four position angles of which two were orthogonal and two the corresponding anti-parallel ones. The Hα emission line was used as spectro-astrometric indicator. The data has an average rms noise level of 5 mas and the author was able to confirm almost all previously known binaries in the sample with separations down to 100 mas. This work demonstrates the capability of spectro-astrometry to resolve binaries but also points out that the binary separation can only be determined with the position spectrum alone if the spectral energy distributions of both components are known.

Takami et al. (2003) studied several pre-main sequence stars with spectro-astrometry for binarity and outflows. They found various binary stars and some targets with monopolar and bipolar outflows which are not uncommon for pre-main sequence objects. The authors mainly followed the suggestions of Bailey (1998) to ensure the quality of the spectro-astrometric quantities. As the seeing was way larger than the slit width, artefacts were of no importance to their data after anti-parallel subtraction. However, the spatial resolution only reached several tens of milli-arcseconds.

## 2.10.2   Outflows

VLT/UVES data were used by Whelan et al. (2005) to detect an outflow from a ρ Ophiuchi brown dwarf. Oxygen I and Hα emission lines were used as tracers of spectro-astrometric signatures. The $1\sigma$ error of the centroid position is about 15 mas due to the low brightness of the target. The detection is $3\sigma$-significant but the kinematic shape of the feature is not clear. The authors do not perform a real modelling of the signatures and also do not discuss the possibility of artefacts being responsible for the features. This would be especially interesting as the slit width was chosen to be *larger* than the seeing.

## 2.10.3   Disks

Kinematic spectro-astrometric signatures are caused by velocity fields. Stellar disks are a possible origin of such features and a closer investigation allows to determine the size, orientation and inclination of a disk with spectro-astrometry. This was aimed at by studies of Oudmaijer et al. (2008) and Pontoppidan et al. (2008). The first work tried to find disks around two bright Be-stars and reached a rms-noise level in the position spectrum of about 0.4 mas. Despite the good data quality, signatures in the position spectrum could not be found. The latter work presents observations on three protoplanetary disks with a dust-gap. Molecular gas was detected in these gaps for all three disks by modelling kinematic spectro-astrometric signatures in the position spectrum. Anti-parallel subtraction was performed by the authors to get rid of instrumental artefacts. From the publication, it is not entirely clear whether or not artefacts could entirely be removed and whether the signatures attributed to the target are in deed real. However, the authors state that they could determine the orientation and inclination of the disks with a precision of about $1° - 2°$.

## 2.10.4   Instrumental artefacts

A first analysis of instrumental artefacts in spectro-astrometric position spectra was conducted by Brannigan et al. (2006). They made a simple two point source simulation in order to show that asymmetric PSFs lead to artefacts in the position spectrum. The authors find that the shape of the artefacts differ from the target-induced signatures of a binary and that the amplitude of artefacts diminish for decreasing slit width. They

recommend to obtain exposures using a slit width smaller than the seeing width and to take longslit spectra at anti-parallel slit orientations.

### 2.10.5 Remarks

The above summary shows that important scientific results have been obtained with the technique of spectro-astrometry in the last decade. It was proven that the detection of binary stars, stellar outflows and of circumstellar disks is possible. However, none of the cited publications uses the width spectrum to constrain the target models, if a model process is done at all. This is particularly important as it is shown in this work that the best-fitting models obtained only with the position spectrum are not necessarily correct, cf. Chap. 4. The investigation of instrumental artefacts is very often neglected in spectro-astrometric publications and the authors in some cases fail to convincingly show that the detected signatures are target-induced. All authors apply the anti-parallel subtraction method and do not systematically study the behaviour and variations of artefacts. This emphasises that there is potential left to be exploited for future spectro-astrometric studies, even with the currently achieved noise levels.

# Chapter 3

# CRIRES giant star data set & Data reduction

This chapter describes the data set on the giant stars RS Vir and TW Oph and the data set on $\alpha$ Centauri A as well as the data reduction procedure that should be applied before and after extracting spectro-astrometric signatures. The chapter is structured as follows: section 3.1 describes the target selection criteria, some basic target properties and the observing procedure. The section on the data reduction process, Sect. 3.2, discusses a spectro-astrometry-suited method to detect bad pixels and analyses the following reduction steps with respect to their impact on the spectro-astrometric quantities: longslit spectrum trace correction, sky background subtraction, flat fielding, detector non-linearity and image distortion corrections as well as wavelength calibration.

## 3.1 CRIRES giant star data set

The scientific goal of this work with respect to the application of spectro-astrometry to astronomical targets is the detection of surface structures on cool giant stars. With this intention the observations were planned and performed as described below.

### 3.1.1 Instrument and target selection

The detection of structure in astronomical sources with spectro-astrometry requires the spectral energy distributions of the different regions of this structure to differ significantly. Projected to our case of cool/hot spots on a background stellar atmosphere this means that it is important for the spots to have significantly different SEDs (in contrast to the atmosphere). The lines of the $^{12}C^{16}O - \Delta\nu = 2$ band transitions at $\lambda \approx 2.3\mu m$ are very temperature sensitive. The cooler a spot the deeper the CO absorption lines. Furthermore, the lines are numerous. This allows for a discrimination of spots of different temperature and for the application of cross-correlation to increase spatial resolution. Thus, an instrument was required which operates in the near infrared (NIR), features high spectral resolution and ideally is connected to a large telescope with adaptive optics. The latter helps to maximise the attainable spatial resolution, see Sect. 2.4. The VLT/CRIRES spectrograph is the instrumentation of choice for performing spectro-astrometric observations in the near-infrared: It allows for NIR, high spectral resolution spectroscopy ($\approx 1.0 - 5.0\,\mu m$ at $R \leq 100,000$) in conjunction with an adaptive optics system at a $8.2\,m$-VLT telescope. Target selection was performed according to some simple criteria. The stars have to (a) be late spectral type giants or supergiants (i.e. K-, M- or C-type), (b) have a large apparent

Table 3.1: Some basic parameters of the targets: spectral type, effective temperature, distance, apparent diameter, variability type, photometric variability period, maser emission.

|              | TW-Oph    | RS Vir           | References  |
|--------------|-----------|------------------|-------------|
| SpT          | C5.5      | M6–M8            | (a), (b)    |
| $T_{eff}$ [K] | 2450      | $2160 \pm 133$   | (c), (d)    |
| D [pc]       | 280–450   | 360–700          | (e)         |
| d [mas]      | 11        | 8                | (f)         |
| $\xi$ [km/s] | 2.2       | —                | (g)         |
| C/O          | 1.2       | 1.0              | (h)         |
| var.type     | SRb       | Mira             | (a), (b)    |
| period [d]   | 185       | 354              | (a), (d)    |
| maser        | –         | $H_2O$, OH, SiO  | (b)         |

(a) Sloan et al. (1998); (b) Herpin et al. (2006); (c) Bergeat and Chevalier (2005)
(d) Van Belle et al. (2002); (e) Perryman et al. (1997); (f) Richichi et al. (2005)
(g) Lambert et al. (1986); (h) Eglitis and Eglite (1995)

diameter and (c) be observable from the VLT-Paranal site. A large diameter leads to large spectro-astrometric signatures. Furthermore, the objects should (d) not be strongly veiled by dust lest surrounding material influences the spectro-astrometric spectra of the stellar disk. If the targets are chosen to be (e) very bright, very high S/N can be reached in very short integration times. I searched the CADARS (Pasinetti Fracassini et al., 2001) and CHARM2 (Richichi et al., 2005) databases for any star matching all of the above criteria. Both catalogues together contain any star for which the apparent diameter to date has been measured[1]. The resulting complete set of candidate targets contains some 66 stars and includes stars with apparent diameter of more than 8 mas. Another strong restriction for target selection is placed by the minimal integration time of the CRIRES instrument. This limits the maximum brightness of observable targets since the detector saturates for brighter stars, as CRIRES does not have neutral density filters to dim the light beam. In a few cases the wavefront sensor of the adaptive optics also places such a brightness limit lest the avalanche photo diodes of the sensor take damage from overexposure. Respecting all of the constraints above, I initially aimed at stars with an apparent diameter of $15 - 30$ mas. However, after it turned out that for technical reasons the true minimal exposure time is 1.0 s instead of 0.1 s, I had to limit the attainable targets to diameters of $6 - 12$ mas. The probability that surface structures can be detected on these smaller stars is naturally smaller as well. In the future, the huge brightness of targets will probably no longer be problematic as additional neutral density filters are expected to be available. Table 3.1 lists some basic properties of the two objects which were eventually chosen as targets. Both stars are cool giants. TW Oph has an increased C/O-ratio and, hence, falls into the category of carbon stars. It is semi-regularly variable with a period of 185 days. RS Vir in contrast is a Mira-variable star at a period of 354 days and has water-, OH- and silicon oxide maser emission in the surrounding dust/gas envelope – see the references given in the table legend. Both stars are asymptotic-giant-branch (AGB) stars and are slightly veiled at optical wavelengths. However, their evolution is not yet very advanced as they are very bright in the near-infrared. No high mass loss rates have been detected,

---

[1] I only considered objects whose diameters have been determined by *direct* methods such as interferometry and lunar occultation, excluding methods like spectrophotometry, as they are more likely to deliver reasonable results.

cf. Herpin et al. (2006); Bergeat and Chevalier (2005). Both targets are single stars and are not known to show any peculiarities which could affect the spectro-astrometric signatures of the stellar surfaces. The two stars RS Vir and TW Oph were the optimal targets for spectro-astrometry with CRIRES at the time of the observations and were the stars with the largest apparent diameters of all target candidates which met all constraints placed by the instrument. Hipparcos and Tycho photometric observations (Perryman et al., 1997; Høg et al., 2000) of the two objects exist in the form of sparsely sampled time-series. It allows to identify the stated periods but it cannot trace the impact of surface spots on the photometric target brightness. The southern position of the targets on the sky (Dec $\approx -20°$) prevented photometric observations with the Oskar-Lühning-Telescope of our institute. Since the time scale of changes of surface features on supergiants can vary strongly, very long term photometric observations would be required to detect surface features photometrically. The interpretation of such data would be difficult as photometric variability is caused by various stellar phenomena. Thus, photometric observations are not expected to be a useful addition to spectro-astrometric data.

### 3.1.2 Observations

I obtained four hours of service mode observing time at the VLT/CRIRES facility in period P79 (April–September 2007). With this time budget I decided to observe two giant stars at four position angles each. These are $0°, 90°, 180°$ and $270°$, thus yielding information at two truly different (and orthogonal) slit orientations and at two anti-parallel ones. Since the main goal of the observations was an investigation of the technique of spectro-astrometry (i.e. not a purely scientific application) I decided in favour of the anti-parallel orientations rather than using four independent orientations. The latter would have allowed to place stronger constraints on the best-fitting spot models, whereas the former allowed to compare the artefact removal algorithm to the anti-parallel subtraction method, see Sect. 2.6. Along with the targets TW Oph and RS Vir two standard stars were observed to identify telluric absorption lines in the targets' spectra. Stars with very few spectral lines in the wavelength range in question are optimal to achieve this. Hence, I chose the two B-type stars HD 173300 (for TW Oph) and HD 121263 (for RS Vir) to serve as reference. They are close to the corresponding targets on the sky (minimising telescope movements) and at the same airmass, meaning that light traverses the same path length through the Earth's atmosphere. The reference stars have apparent diameters of less than one milli-arcsecond and have not been reported to consist of multiple components. As a consequence there is no spectro-astrometric signature to be expected. Time constraints restricted us to observe the reference stars at only one arbitrary slit orientation. Because of the brightness of all targets, very high S/N could be obtained in short integration times. However, the greatest part of observing time was consumed by the overheads that resulted from the change in position angle by using the image derotator of CRIRES. Thus, I had to plan observations in the way that all exposures at a specific position angle were performed consecutively[2]. To be able to compare the SEDs of the target and the standard star, both were exposed to yield similar S/N. As an important issue in planning spectro-astrometric observations direct averaging of individual exposures by the instrument software should be avoided. A standard practice is to co-add NDIT[3] exposures

---

[2]Recently the instrument software supports quick derotator changes with overheads of just a few seconds in contrast to six minutes when our observations were performed. This allows for exposing at alternating position angles. The latter could, to some degree, improve the quality of the anti-parallel subtraction method.

[3]The integration time of a single exposure is called DIT in ESO terms. The number of co-added exposures to yield a single FITS-file is named NDIT. Thus, the total integration time per FITS-file is

Table 3.2: Short summary on the service mode observing run on TW Oph and RS Vir, ESO programme ID 079.D-0710. Numbers are with respect to individual exposures except where stated otherwise.

|                          | TW Oph      | RS Vir         |
|--------------------------|-------------|----------------|
| date                     | 2007-07-26  | 2007-04-23/25  |
| total integration time   | $0.75\,h$   | $0.75\,h$      |
| slit orientations        | 4           | 4              |
| max. S/N at continuum    | 1000        | 750            |
| max. CO-line depth       | 85 %        | 75 %           |
| seeing [arcsec]          | 0.60-1.2    | 0.7-1.2        |
| PSF FWHM width [arcsec]  | 0.21-0.7    | 0.25-0.7       |

Table 3.3: Some basic parameters of $\alpha$ Centauri A: spectral type, effective temperature, mass, metallicity, rotation period, distance, apparent diameter.

|                                         | $\alpha$ Centauri A     |                       |                     |          |
|-----------------------------------------|-------------------------|-----------------------|---------------------|----------|
| SpT, $T_{\text{eff}}$, $M/M_\odot$      | G2V                     | $5810 \pm 50\,\text{K}$ | $1.105 \pm 0.0070$  |          |
| Fe/H, $T_{\text{rot}}$, D, d            | $0.22 \pm 0.05$         | $22\,\text{d}$        | $1.33 \pm 0.01\,\text{pc}$ | $8\,\text{mas}$ |
| $\log(g)$                               | 4.3                     |                       |                     |          |
| References                              | Eggenberger et al. (2004) |                     |                     |          |

immediately after integration such that only a single FITS-image is written. Usually that is done to enhance the S/N of the FITS-files and to keep the number of images low. However, in the case of spectro-astrometry such a procedure has a drawback: because atmospheric conditions change on short time scales, as a result, exposures that were taken at different seeing qualities and artefact amplitudes are averaged. If, in contrast, every exposure is registered individually one can select those with minimal artefact amplitudes to obtain better spatial resolution[4]. The co-addition of extracted spectro-astrometric quantities is anyway possible later-on. For the observations of the two giant stars I applied a NDIT of ten but would now recommend to change it to one for further observations as there is no advantage in using a NDIT of more than one. A summary of the observations is given in Tab. 3.2.

### 3.1.3   $\alpha$ Cen data

In the course of another project in my working group, VLT/CRIRES data on $\alpha$ Centauri A has been obtained at six different position angles in the M-band[5]. This data is suitable for spectro-astrometric analysis. See Tab. 3.3 for some basic parameters. Although that target is no giant star but a solar-like G2V star it has an apparent diameter of $8\,\text{mas}$ because its distance to the sun is only $1.3\,\text{pc}$. Thus, the detection of large surface spots on $\alpha$ Cen is possible. The star has been observed in the fundamental $CO - \Delta\nu = 1$ band transitions at $\lambda \approx 4.7\mu m$. With this data spectro-astrometry could be tested in the M-band. Spectra were taken at six almost equally spaced slit orientations. The average

---

$T = \text{NDIT} \cdot \text{DIT}$.

[4]As discussed later on, cf. Sect. 4.3, artefacts do indeed vary significantly between exposures taken less than a minute apart. A likely reason is that the actual AO-influenced PSF varies from exposure to exposure.

[5]The aim of this other project is to determine the spin orientation of the star.

S/N is 120 per exposure in the continuum. The sky background is much stronger than in the K-band and there are several atmospheric emission lines. The corresponding results are also presented in Chap. 4.

## 3.2 Data reduction

### 3.2.1 Bad pixel detection and masking

As it has already been discussed in the previous chapter, bad pixels can affect the fitting procedure used to evaluate $\mathcal{C}(\lambda)$ and $\mathcal{W}(\lambda)$ and impair those two quantities seriously. Here, real bad detector pixels and pixels affected by cosmic ray hits are both summarised by the term *bad pixel*. Thus, a removal or at least a masking of bad pixels is required. *Masking* means that bad pixels are detected and the corresponding spatial profile is indexed in a so-called bad profile mask. If the pixel cannot be corrected for, one can choose to ignore such profiles in the following extraction and analysis process. I will show how the detection algorithm works and whether a correction of bad pixels works successfully.

The standard procedure of bad pixel detection is *not* used here[6]. Instead, first, strong outliers are removed: the median count value over the full spatial profile is evaluated and any pixel that deviates by more than three standard deviations is marked as bad. Then, pixels have to be detected which differ only slightly from the linear behaviour. For that I take advantage of the facts that the spatial profile of the long-slit spectrum varies only slowly with wavelength and that only pixels lying inside the region used for fitting are relevant. If the former is true, it allows us to compare each spatial profile with a template profile. The template should be formed by averaging a sufficient number of profiles that are a) known to be free of bad pixels and b) taken from a small range in wavelength to avoid changes in the spatial profile. In short, the detection procedure works as follows: first, an initial template profile is formed. The algorithm then loops over all spatial profiles. If the profile currently under investigation, henceforth *current profile*, deviates significantly from the template, it is rejected and marked as *bad*. Otherwise it is considered *good* and the template constituent that is farthest away from the current profile is replaced with the current profile. Then the loop continues to the next profile. This procedure ensures a dynamic template, i.e., it adapts to a slow change of the spatial profile with wavelength. This overview lacks important details:

a) Finding sound profiles as constituents of the initial template profile is critical and difficult for real data. If one simply chooses to average the first $N$ profiles of a longslit spectrum the risk of bad pixels influencing the initial template is too large. Instead, one draws $N$ profiles randomly from the first five to ten times $N$ profiles and form an average profile. This procedure is repeated a number of times. Then, the two most deviating average profiles are removed and one of the typical average profiles is taken as initial template[7].

b) Comparing or averaging two or more profiles requires them to have identical centroid positions with respect to the sampling pixels. Differences in the centroid can either be caused by spectro-astrometric signals or by tilted longslit spectra[8]. Because of the targeted accuracy in spatial resolution, it is important to register the profiles to sub-pixel accuracy,

---

[6]Usually one uses two flat field exposures of vastly different exposure level. One is divided by the other to check for non-linearly behaving pixels.

[7]This procedure is only necessary if the choice of the initial template profile has to be done automatically. Choosing $N$ profiles manually will lead to the best initial templates. However, when dealing with large amounts of exposures this is impracticable.

[8]Most longslit spectra are significantly tilted with respect to the detector rows or columns.

see below. A cross-correlation algorithm is used to obtain the optimal shift: for each trial shift, the $\chi^2$ measure is evaluated for the difference of the current profile and the template profile. The shift with the smallest $\chi^2$ value is then applied to the profile.

c) One judges a profile to deviate significantly from the template if at least one pixel of the current profile deviates by more than three $\sigma_{\rm pix}$ from the template profile. Here, $\sigma_{\rm pix}$ is the standard deviation of each template pixel which is evaluated by summing over the template's constituents.

**Detection method:** detecting bad pixels in this way relies on the ability to register profiles to subpixel accuracy. There are two obstacles in reaching this aim. First, a bad pixel does already influence the procedure of finding the optimal shift. If the shift eventually applied is offset from the true one, one or even several good pixels can be judged to be bad and vice versa. Nevertheless, that method still is very successful in detecting bad *profiles* rather than bad *pixels* because the true shift will be found if there is no bad pixel. Hence, *good* profiles will be recognised as such. If one ignores the bad profiles in the analysis of the spectro-astrometric signatures, any influences are avoided. If, however, many bad pixels are present, this profile masking can strongly reduce the number of useful wavelength bins. The second obstacle is the shifting procedure itself. Because of the finite pixel sampling of the spatial profile, sub-pixel shifting is necessary. Gaussian shifting[9] cannot be used even if the basic profile is Gaussian since any outlier would first affect the fitting procedure and second, of course, the outlier itself could not be shifted at all with this method. Naturally, (linear) interpolation is also utterly useless in this case.

Thus, I always applied *Fourier transform shifting* in this work when sub-pixel shifting was necessary, see e.g. Stone et al. (2001). It is a method of image registration frequently used in many fields of science, e.g., satellite imaging and medical imaging (computer tomography and magnetic resonance imaging). The basic idea is that a shift in spatial coordinates corresponds to the multiplication of a complex phase in frequency space. If $f(x)$ and $F(\omega)$ represent a continuous function and its Fourier transform, respectively, then

$$f(x - x_0) = F^{-1}\left(F(\omega) \cdot e^{-j\omega x_0}\right), \tag{3.1}$$

with $F^{-1}$ being the inverse Fourier transform. In the case of two-dimensional images the procedure is equivalently done with the Fourier transform in two dimensions. The above relation is exactly true for continuous functions only. Real images, however, are neither continuously sampled nor free of noise. If the sampling rate of the profile is too low, aliasing occurs in frequency space and leads to artefacts in the shifted image – compare Stone et al. (2001) for more details. I applied the procedure to the spatial profiles of longslit spectra and found that it works very well without noticeable artefacts in the shifted profiles. This is to be expected as long as the profiles do not contain any high-frequency information[10]. The spatial sampling rate needs to be large enough to contain all relevant frequency information. Noise in the profiles has to be very low because noise contributes to the high-frequency region. I performed a simple test to quantify the behaviour of the shift algorithm with respect to profile shifting: two ideal Gaussian profiles with centroids at $x_1$ and $x_2$, respectively, were created at a given S/N and spatial sampling. The Fourier transform method was then used to shift one of the two profiles to the centroid position of the other. Finally, the difference profile was used to evaluate the quality of the shifting procedure. The spatial sampling as well as the S/N were varied. I found that the procedure introduces *shifting noise* at an amplitude of less than one percent if the S/N of the data

---

[9]Fitting a Gaussian to the profile and evaluating the function at the points $x_i^{'} = x_i + \Delta x$, where $\Delta x$ is the shift, to obtain the shifted profile

[10]*High-frequency*, here, means frequencies larger than the Nyquist frequency.

is above 10 for usual profile sampling. Hence, shifting noise can be generally neglected for our data – in case of very small profiles it may become a serious issue. In the latter case also other problems occur, cf. Sect. 2.4.

**Interpolation method:** In principle interpolation over bad pixel is feasible and can be used to reliably replace those pixels. Simple linear interpolation using both adjacent pixels is insufficient if the profile is not extremely oversampled because its shape is distorted. A better approach is to use the value of the best-fitting Gaussian as replacement, excluding the bad pixel before fitting. A third method replaces the bad pixel by the corresponding pixel value of the template after scaling it to the current profile's amplitude and shifting it to a common centroid position. Both methods, theoretically, work well; the first under the premise that the profile is Gaussian. The critical point is whether the bad pixel detection routine correctly found the bad pixels. As discussed above, it may well be that a *profile* is identified as bad but the bad *pixel* within this profile cannot be identified correctly. Of course this renders an interpolation over the pixel impossible. The situation becomes even worse if more than one bad pixel is present in a spatial profile.

**Summary:** The bad pixel treatment can be summarised as follows. Bad profiles/pixels are first detected by comparing each spatial profile of the longslit spectrum to a dynamic template profile. Since it is unclear how reliable the detection of individual bad pixels works I proceed as follows: bad pixels are replaced by the corresponding value of the scaled and shifted template profile *and* bad profiles are marked as such in a bad profile mask. This allows for a later crosscheck for coincidences of features in $\mathcal{C}(\lambda)$ and $\mathcal{W}(\lambda)$ with entries in the bad profile mask. A subpixel shifting algorithm is vital for the above steps to work properly. I implemented a Fourier transform based algorithm and tested it to work well under most conditions which are relevant for bad pixel detection. I performed the detection algorithm on the raw longslit spectra, i.e. before the flatfielding and before the A–B background subtraction, see below. Both bad pixel masks are then added to yield the A–B pair mask. If flatfielding is applied to the pair spectrum or to the individual A- and B-spectra, the detection code is rerun after the flatfielding to check for additional bad pixels induced by the flatfield exposure.

**Simulated & CRIRES data:** First, several simulated longslit spectra of varying S/N and bad pixel content were processed by the algorithm. Later, the code performance was evaluated for the real CRIRES data set. The detection of strong outliers works perfectly and removes hot/cold pixels as well as large amplitude cosmic ray hits. For the simulated data, the input bad pixel were compared to the detected ones. Under realistic conditions the algorithm performed very well. *Realistic* here means that S/N and spatial profile are within usual parameters. Although the possible scenarios are numerous I summarise the findings for Gaussian or Gaussian-like profiles: a) the spatial profile needs to be sampled by at least six pixels (covering 95% of its area) for the code to succeed in most cases; b) bad *profiles* are always detected if the count value of the bad pixel is at least some percent above/below the true value of the pixel, i.e., if the pixel was not a bad pixel, and c) if the amplitude of the bad pixel exceeds some level, but remains below the median cut-off level, the determination of the shift will be affected such that only the profile as a whole is found to be bad. The values of both levels vary, depending on the exact scenario. However, it is important to estimate the impact of undetected bad pixel on the spectro-astrometric quantities. If a typical value of three percent is assumed for the lower level and one bad pixel in a Gaussian profile, this translates into an uncertainty in the centroid position of about 1/1000 pixel. This value was obtained for very high S/N in order to avoid noise contributions. For various simulation scenarios about 97% of bad pixels/profiles were detected if the bad pixel amplitude exceeded three percent. If a similar performance is

achieved for real data, residual bad pixels are of no concern. Those only lead to spurious false peaks in $\mathcal{C}(\lambda)$ and $\mathcal{W}(\lambda)$ and, hence, can be identified because of missing correlation with the targets SED. Application of the code to the CRIRES data set yields an average detection rate of 15 per detector chip. There are 1024 pixels in total per chip in dispersion direction giving a bad pixel fraction of roughly 1.5%. The pixel scale in spatial direction is 84 mas per pixel. The influence of undetected bad pixels can be completely neglected assuming the above 1/1000 pixel uncertainty.

### 3.2.2   Trace correction

Another reduction step which has to be implemented to meet the requirements of spectro-astrometry is the detection of the longslit spectrum's trace. The term *trace* designates the absolute position of the spectrum on the detector in spatial direction. Spectro-astrometrically speaking, it is identical to the centroid position. The main contribution to the trace, however, results from the longslit spectrum being tilted and/or curved with respect to the detector rows and columns. The trace is important in standard spectrum extraction in order to optimally extract the one dimensional spectrum of the target. When reducing data for later spectro-astrometric analysis, the trace needs to be corrected for, too. Otherwise, the comparison of different exposures and the comparison of observed and theoretically modelled data is impossible. In principle, one can try to describe the trace with the help of the grating equation and knowledge about the instrumental setup. This is not done in the following as spectro-astrometric analysis requires the correction of the trace to be much better than the desired spatial resolution. This is much easier and instrument-independent to achieve by the following procedure: first, the $\mathcal{C}(\lambda)$ and $\mathcal{W}(\lambda)$ are extracted, see Chap. 2, for all $\lambda_i$ with $i = 1, \ldots, M$ where $i$ denotes the $i$th pixel of the detector and $M$ the number of pixels in the dispersion direction. Then, for each $i$, the $N$-average values $\bar{\mathcal{C}}_{i,N}$, where

$$\bar{\mathcal{C}}_{i,N} = \frac{1}{2N} \sum_{j=1}^{N} \left[ \mathcal{C}(\lambda_{i-j}) + \mathcal{C}(\lambda_{i+j}) \right], \qquad (3.2)$$

are evaluated. The final centroid ($\mathcal{C}_{\mathrm{f}}$) values are then obtained by $\mathcal{C}_{\mathrm{f}}(\lambda_i) = \mathcal{C}(\lambda_i) - \bar{\mathcal{C}}_{i,N}$. The same is done for the width spectrum $\mathcal{W}(\lambda)$. The choice of $N$ is critical as there is always a trade-off between optimal trace removal and the conservation of the spectro-astrometric signatures. The smaller the value of $N$ the more accurately the true value of the trace could be estimated if there were no small-scale variations in the centroid position. The larger the value of $N$ the less such variations influence the determination of the trace but the less accurate the trace position can be obtained. Spectro-astrometric signatures indeed are variations in the centroid position and do directly influence the determination of the trace. Hence, $N$ should be chosen to be much larger than the expected maximum width of those signatures. If $N$ is chosen too small, spectro-astrometric signatures will be changed by the trace removal procedure.

The trace correction method was tested using different data sets obtained with different instruments and proved to yield excellent results. Figure 3.1 depicts one example of $\mathcal{C}(\lambda)$ extracted from a CRIRES spectrum of TW Oph with and without trace correction. Only a spectrum which contains lines of vastly different width could result in failure of the above method because then $N$ cannot be chosen optimally for narrow and broad lines at the same time.
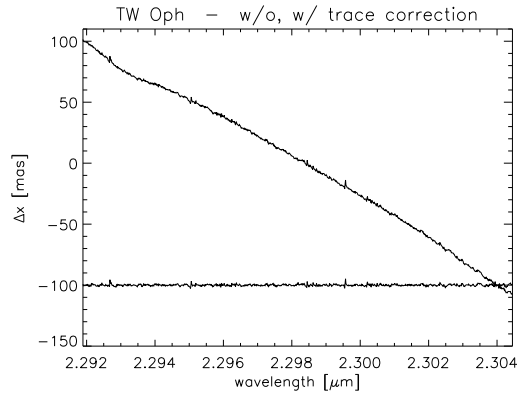
Figure 3.1: The graph contains the position spectrum $\mathcal{C}(\lambda)$ extracted from a raw longslit spectrum of TW Oph. The upper curve represents the spectrum before, the lower one after trace correction. The former shows a strong tilt and some curvature that is completely removed in the latter. The scale of the spatial axis is milli-arcseconds with a pixel scale of the detector of 87 mas. The scale parameter is $N = 20$.

### 3.2.3 Standard data reduction

In this section I discuss the data reduction steps which are commonly used when working with longslit spectra. Each step is questioned whether or not it is improving the quality of the extracted spectro-astrometric signatures.

#### 3.2.3.1 Background subtraction

It is common practice to record longslit spectra in so-called *nodding cycles*. This means that the telescope is moved slightly between different exposures. The spectra, thus, are recorded at different positions on the detector. A common nodding scheme is ABBA, which means that two different positions A and B are used in the denoted order. Thereafter, the scheme is repeated until the desired number of spectra has been obtained. By subtracting A from B exposures, or vice versa, an effective removal of the background is achieved as long as the background itself does not vary on small spatial scales and if it does not vary faster with time than the time spacing of the two exposures. For the near-infrared data used in this work this requirement was well met. Hence, the A–B subtraction was applied for all exposures.

A good background subtraction is important for the extraction of the centroid/width spectra lest the background influences the Gaussian fitting process. Thus, the subtraction has to be done either before the extraction process, e.g., via A–B, or during the fitting process itself by fitting a Gaussian plus a low-order polynomial. For the data sets used here, the A–B method was applied and an additional polynomial fitting of the spatial profile was found to increase the background subtraction quality not at all. A disadvantage of the A-B subtraction is that it increases the number of bad pixels which fall into the target's spectrum as bad pixels from the background region of the B exposure are subtracted into the spectrum region of A and vice versa.

#### 3.2.3.2 Flatfielding

The individual pixels of a detector chip are non-uniform in sensitivity. To compensate for this, a homogeneously illuminated field is recorded with the same instrument configuration

as is used for the science exposures. This is done by either obtaining sky exposures during dusk and/or dawn or by observing a uniform area in the telescope dome which is lit by a lamp. Such a flatfield exposure documents the sensitivity of the pixels. By normalising it to one and then dividing it into the science exposure, the sensitivity deviations are ideally removed. The ins-and-outs of flatfielding are not discussed here since I take them to be common knowledge in the astronomical community[11]. Flatfielding is also expected to improve the quality of the extracted $\mathcal{C}(\lambda)$ and $\mathcal{W}(\lambda)$ spectra. Non-uniform pixel sensitivity leads to distortions of the spatial profile and, hence, affects the profile fitting procedure directly. This problem is corrected by flatfielding.

Flatfield images were obtained during daytime calibration time with the same instrument configuration as used while observing the targets. This procedure was necessary to maximise on-target observing time. Because flatfields are not expected to vary on short time scales the time difference between calibration and science exposures is non-critical. No significant differences could be found between flatfields obtained in April and June 2007 supporting this assumption. I used dome flatfields exposed with and without lamp illumination and median-combined the individual images. Lamp response was removed by fitting and subtracting low-order splines to spatially collapsed flatfields. To test if and how strong an improvement can be seen in the relevant quantities $\mathcal{C}(\lambda)$ and $\mathcal{W}(\lambda)$ is extracted for longslit spectra of the data set before and after flatfield processing. Although only marginal, there is, on average, a lower noise in the spectro-astrometric quantities after flatfielding. The improvement varies from exposure to exposure and is about one to three percent.

### 3.2.3.3   Detector non-linearity and odd-even effect

The detectors of the CRIRES instrument suffer from non-linearity and the so-called *odd-even* effect. The latter means that every other pixel row or column has an offset in count value from the mean, see Fig. 3.2 for a raw CRIRES longslit spectrum. The amplitude of the effect is different for each of the four detector chips. It depends on the count level and, hence, the integration time of the exposure. The non-linearity is significant above $4000\,\mathrm{ADUs}$ (analog-digital-unit). According to the ESO Online CRIRES material[12] both
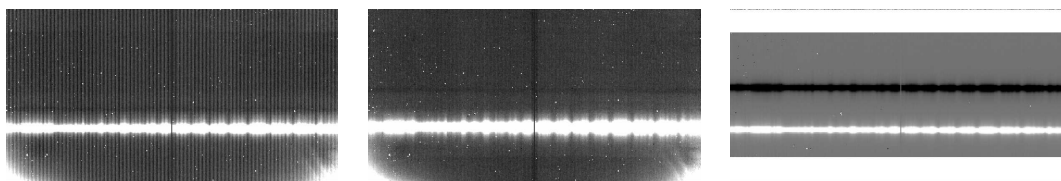


Figure 3.2: The left graph shows a raw CRIRES longslit spectrum with a strong odd-even effect. In the middle panel, the non-linearity correction has been applied. The A-B subtraction has then been performed to obtain the right image. For the latter, the grey scale had to be adjusted.

effects can be minimised. Therefore, flatfield exposures of increasing integration time have to be obtained. Then, a second order polynomial is fitted for each pixel individually, $I(x,y) = A(x,y) + B(x,y) \cdot \mathrm{DIT} + C(x,y) \cdot \mathrm{DIT}^2$. Assuming that the non-linearity gradually vanishes with decreasing intensities the true signal is $I_{\mathrm{true}} = B \cdot \mathrm{DIT}$. Thus, after the determination of the coefficients A, B and C, the correction can be applied. For integration

---

[11]The *ins-and-outs* are, e.g., lamp response correction and slit illumination correction. Each of these topics can be quite tricky depending on the instrument. However, no unusual problems occurred when dealing with the CRIRES data.

[12]http://www.eso.org/sci/facilities/paranal/instruments/crires/tools/

times longer than two seconds the odd-even-effect can be removed almost completely. For integration times shorter than two seconds, as mostly used in this work's data sets, the origin of the non-linearity is different, namely the final reset time of the detectors. Hence, according to ESO, the correction does not work properly. Nevertheless, I applied the procedure and found a significant improvement even for one second exposures, cf. Fig. 3.2. SEDs extracted from the raw longslit spectra clearly show the odd-even effect. After the correction the amplitude is significantly smaller. Finally, the A-B background subtraction further diminishes that amplitude. Still more important is that no residual impact of the non-linearity and odd-even effect can be seen in the $\mathcal{C}(\lambda)$ and $\mathcal{W}(\lambda)$ spectra.

### 3.2.3.4  Image distortion

Slit curvature is one reason why the longslit spectrum can show significant distortions. Aberrations in the telescope and/or instrument optics are another source of this effect. Fitting a two-dimensional polynomial to the longslit spectrum of a calibration lamp or gas cell is a common way to correct for such distortions. Often this step is combined with wavelength calibration, cf. Sect. 3.2.3.5. Applying the fit to that spectrum and all other calibration and science frames removes the distortions if these can be represented by a polynomial, or whatever functional form has been fitted for. The closer the wavelength region is sampled by lamp/cell lines the better the correction will work. Figure 3.3 shows a VLT/ISAAC raw lamp spectrum with obvious image distortions before and after the correction. Image curvature/distortion directly affects the spectro-astrometric quantities
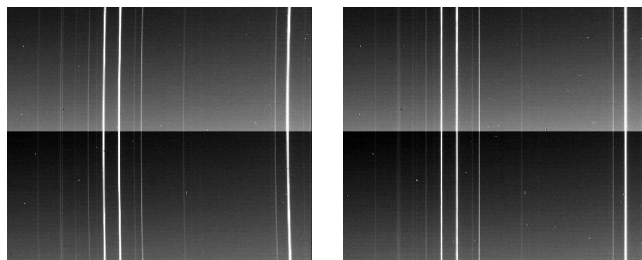


Figure 3.3: On the left is a VLT/ISAAC Thorium-Argon-lamp raw longslit spectrum. The emission lines visualise the image distortions. The latter are easy to identify when comparing the image with the right subfigure that shows the same exposure after distortion correction.

such that one needs to consider the impact on the analysis process. Curved spectral lines, as shown in Fig. 3.3, demonstrate that points of constant wavelength no longer are perpendicular to the columns or rows of pixels of the detector. Hence, the spatial profile would have to be evaluated at a curved path across the detector. Because of the discrete sampling of the detector plane this is impossible. The fitting of a profile along detector columns/rows, which is necessary to extract $\mathcal{C}(\lambda)$ and $\mathcal{W}(\lambda)$, thus does not yield the true spectro-astrometric quantities. On a first glance it seems to be reasonable to correct for such distortions and then start the extraction procedure. The quality of this procedure depends both on the magnitude of the distortions and on the number and density of lamp/cell lines.

Image distortions induce spectro-astrometric artefacts. This can easily be understood if one assumes curved spectral lines and locally approximates them by tilted straight lines. As shown in Sect. 2.6, tilted spectral lines are also a result of, e.g., elliptical PSFs and lead to the characteristic artefacts discussed there. Therefore, another possibility to account for image distortions is to omit the above procedure and, instead, try to remove those artefacts together with PSF-induced artefacts. Because the success of the removal algo-

rithm strongly depends on the correct choice of PSF-parameterisation I prefer to perform distortion correction beforehand as it is unclear how distortions affect the PSF-shape. If the distortions are strong and/or vary strongly over the detector this requires a dense sampling of the wavelength range with lamp/cell lines. In case of weak distortions these conditions can be relaxed. If the correction procedure is successful spectro-astrometric artefacts are already diminished before the artefact removal procedure.

**CRIRES data:** Image curvature/distortion is close to non-detectable for data obtained with the CRIRES instrument. Fitting polynomials to lamp longslit spectra yields that distortions are less than 0.2 pixels over the whole spatial direction which consists of 512 pixels. Lamp exposures only contain few spectral lines and no gas cell was available at the time of observations. Hence, I decided to omit distortion correction completely. The amplitude of any distortion-induced artefacts are small compared to PSF-induced artefacts. I conclude that even if the former cannot be removed by artefact simulations they do not limit the attainable spatial resolution.

### 3.2.3.5   Wavelength calibration

A spectrograph maps the incident light to the detector dispersing it in wavelength. Ideally this mapping is linear in wavelength and light of a specific wavelength is always mapped to the same point on the dispersion axis. In reality, this aim cannot be achieved and the mapping is neither linear nor constant in time. Depending on the required accuracy, different measures have to be applied in correcting the dispersion relation. A reference lamp exposure is often used to fit the relation if medium accuracy is sufficient. Radial velocity (RV) detection of extra-solar planets requires very high accuracy which can be achieved by using a gas cell as reference. The latter often features numerous nearly equally distributed lines over the whole detector. The wavelengths of these lines should be known to high accuracy from laboratory measurements. In contrast to the lamp the gas cell lines are superimposed on *each* exposure and can thus account for temporal changes. Again, this is important for RV measurements as the changes in wavelength of spectral lines between different exposures are targeted at. Any effect which is not intrinsic to the observed object affects such measurements, e.g., mechanic/thermal effects within the spectrograph, the Earth's rotation and revolution etc., and needs to be removed. If sufficiently strong and numerous, telluric lines may also be used for wavelength calibration. Apart from turbulence/wind these emission lines also have a constant wavelength. For some details on the topic of precise RV measurements in general and the calibration accuracy of CRIRES in particular see Seifahrt and Käufl (2008).

If a spectro-astrometric analysis of longslit spectra is aimed at, the issue of wavelength calibration is easier because there is a fundamental difference to RV measurements: performing the latter, one is interested in the shift in wavelength of spectral lines. A possible target-intrinsic shift in radial velocity in most cases is both neither expected nor of any interest in terms of spectro-astrometry. Here only the comparability of, e.g., $\mathcal{C}(\lambda)$ and $\mathcal{W}(\lambda)$ between different exposures and of those quantities with theoretical models is required. In other words, the distances between different spectral lines need to remain constant, i.e., the functional form of the dispersion relation needs to remain constant. An additive shift in wavelength is irrelevant. The inter-line distances change far less between exposures compared to the shift. As a consequence, one can use absorption/emission lines in the target spectrum to relatively calibrate the dispersion relation. This guarantees a comparability of data obtained at different slit orientation and/or epoch. The procedure is illustrated for the case of our CRIRES data set.

**CRIRES data:** I first extracted the $\mathcal{C}(\lambda)$ and $\mathcal{W}(\lambda)$ spectra and then applied the wave-

length calibration. The dispersion relation is first determined by fitting third order poly-
nomial splines to a lamp spectrum which has been obtained during daytime calibration
time. The fitting and application of the dispersion relation is performed with the IRAF[13]
package. This package also allows to determine the wavelength-independent shift between
different exposures. Furthermore, the dispersion relation is also obtained by using the
strongest $CO - \Delta\nu = 2$ lines. I finally evaluated the precision to which the distance
between two spectral lines remains constant after calibration. Randomly, pairs of lines
and two exposures were selected and the distance of the line pairs determined for both
spectra. Then, the shift between the two distances is taken as a measure of the accuracy
of the calibration. If, e.g., an observed spectrum is to be fitted by a model, the best-fit is
determined by minimising the difference spectrum. Thus, it is important to investigate the
implications of residual wavelength calibration errors on difference spectra. Such errors
lead to artefacts in the difference spectra[14]. The amplitude of those artefacts can be easily
estimated by subtracting a spectrum from a wavelength-shifted version of itself. The value
of the shift here is identical to the calibration accuracy just obtained. Performing several
simulations using typical spectro-astrometric signatures and wavelength calibration accu-
racies one arrives at the calibration-artefact amplitudes. For the giant star data set, the
average calibration-artefact amplitude is $0.07$ mas with the individual values lying within
$[0.03, 0.10]$ mas. Considering these values, it is obvious that wavelength calibration errors
do not limit the precision of spectro-astrometry at the levels reached in this work; compare
the results in Chap. 4.

---

[13]Image Reduction and Analysis Facility of the National Optical Astronomy Observatory (NOAO)

[14]These artefacts are totally unrelated to the spectro-astrometric artefacts discussed before and only
result from subtracting two identical spectra which are slightly shifted with respect to each other.

# Chapter 4

# Surface structure of cool giant stars

The aim of this chapter is twofold. First, the methods discussed in Chaps. 2 and 3 are tested and applied to real astronomical data sets. Second, the scientific results are presented for the giant star data set on TW Oph and RS Vir and for the M-band observations of the solar-like $\alpha$ Centauri A. The M-band data has been analysed, mainly, to study whether the performance of spectro-astrometry in this wavelength region is similar to the K-band case. The chapter is organised as follows: Sect. 4.1 states some details on the synthetic model spectra which are used in the source modelling process. A short summary on the data reduction steps that were applied prior to the spectro-astrometric analysis is given in Sect. 4.2. Some common properties of the giant star data set are presented in Sect. 4.3. The application of the artefact removal procedure, the analysis of target-induced spectro-astrometric signatures and the source modelling process is discussed individually for each target in Sects. 4.3.1, 4.3.2 and 4.4.

## 4.1 Synthetic `PHOENIX` spectra

An in-depth study of synthetic spectra of giants and supergiants and a comparison of synthetic and observed spectra is beyond the scope of this work. Further theoretical studies are needed to investigate this subject in detail, compare e.g. Lançon et al. (2007a) and Lançon et al. (2007b). Hence, standard synthetic LTE-models like those of the GAIA grid, Hauschildt et al. (GAIA), were used to compute the spectra which are needed to constrain the spot geometry or the upper limits on spot coverage. As even the best-fitting model spectra[1] do not match the observed data perfectly, cf. Fig. 4.7 and Fig. 4.12, the deduced geometries are affected by these differences. However, the uncertainties induced by the synthetic spectra do not dominate the total model uncertainty due to the limits placed on accuracy by the limited number of slit orientations and the residual instrumental artefacts. The giant models apply a micro-turbulence velocity of $\xi = 2\,km\,s^{-1}$ which is a common value for giant stars. It is, hence, often used if the micro-turbulence has not been determined for a specific target. For RS Vir, there is no such measurement, whereas observations of TW Oph yield evidence for a value of $\xi = 2.2\,km\,s^{-1}$, cf. Lambert et al. (1986). Solar metallicity was assumed for the models but with a modified ratio of C/O of 1.2 for TW Oph and 1.0 for RS Vir, cf. Eglitis and Eglite (1995). The former value

---

[1]Here, the best fit of a synthetic spectrum to an observed one is meant. The goodness-of-fit is judged using the $\chi^2$-measure, cf. Sect. B.2.

has been measured and the latter is a typical value for red giants of Mira-type. The solar photospheric C/O ratio is about 0.50, cf., e.g, Allende Prieto and Lambert (2002). As the $^{12}C/^{13}C$ ratio is as large as 65 for TW Oph, Lambert et al. (1986), the $^{13}CO$ lines are expected to be weaker than those of $^{12}CO$. In general, to date, synthetic spectra of cool (super-) giants and carbon stars do not reproduce observed spectra very well, see Lançon et al. (2007a), in particular at low effective temperatures below 2600 K. As the density in these stellar atmospheres are very low, local thermal equilibrium is unlikely. Non-LTE synthetic models would be needed for a better modelling but consume large amounts of computing time. For more details on the targets and their stellar parameters, see Sect. 3.1. Synthetic spectra were calculated for effective temperatures between 1500 K and 4000 K at steps of 100 K. The surface gravity was set to $\log(g) = -0.5, 0.0, 0.5$ which are typical values for supergiants.

A very different parameter set had to be used for the solar-like $\alpha$ Cen A. Models of the GAIA grid were used to compute synthetic spectra for the $\alpha$ Cen A data set. The effective temperature and surface gravity are known to be 5800 K and $\log(g) = 4.3$, respectively. The a priori known stellar parameters, cf. Tab. 3.3, were used as a starting point to fit the observed SED. Typical temperature contrasts of solar spots were then used to simulate surface structure on $\alpha$ Cen A. In contrast to the case of supergiants, modern synthetic models for main sequence G stars very well reproduce observed data for most of these objects.

## 4.2   Summary on data reduction

The data set on the two giant stars and the one on $\alpha$ Centauri A both have been obtained with VLT/CRIRES, and, therefore, have similar characteristics with respect to data reduction. The difference is that the wavelength of the giant star data set is about $2.3\,\mu m$ and $4.7\,\mu m$ for the $\alpha$ Cen A data. The sky background is brighter in the M-band and varies faster with time and spatial coordinates compared to the K-band. I applied the same reduction steps to both data sets except where stated otherwise.

Data reduction and analysis have been performed separately for each of the four CMOS detectors of the CRIRES instrument. Bad pixel detection/correction, cf. Sect. 3.2.1, was first applied to the raw longslit spectra and then repeated after flatfielding and again after background subtraction. The detections were corrected for, if possible, and registered in a bad profile mask. The masks of the three detection steps were added. The final bad profile mask was used to check features in $\mathcal{C}(\lambda)$ and $\mathcal{W}(\lambda)$ for coincidence with bad profiles. For CRIRES data, the total number of bad pixels/profiles is negligible ($< 1\,\%$) compared to the total number of wavelength points. The first reduction step after the initial bad pixel detection was flat field correction. A master flat field was used which had been constructed by a three sigma clipped median combination of the individual lamp on minus lamp off flat fields, cf. Sect. 3.2.3.2. The frames then were corrected for non-linearity and the odd-even effect, cf. Sect. 3.2.3.3. Image distortions were found to be so small that their impact on the spectro-astrometric quantities is far less than the S/N-limit, cf. Sect. 3.2.3.4. Therefore, a correction was omitted. Because the sky background is spatially flat and does not change on time scales comparable to the time spacing of exposures, the A-B subtraction scheme is perfectly viable, cf. Sect. 3.2.3.1. $\mathcal{C}(\lambda)$ and $\mathcal{W}(\lambda)$ were extracted and corrected for the trace of the spectrum and wavelength calibration was performed, cf. Sect.s 3.2.3.5 and 3.2.2, respectively.

In Chap. 3, the residual errors of the above effects and reduction steps have been estimated and they were found to be smaller than the S/N-limit for the CRIRES data sets. Since the spatial resolution achieved by the analysis, cf. Sect.s 4.3, 4.4, is a factor of about

three lower than the S/N-limit, other contributions dominate the total error budget. Unless there are unrecognised systematic error sources, I conclude that the reason is the imperfect artefact removal.

## 4.3   TW Oph and RS Vir

As in many other applications in this work, the goodness of a fit, in this chapter, also is determined by the $\chi^2$-measure, cf. Sect. B.2.

All data has been obtained using a slit width of $0.2''$ which compares to an average FWHM of the PSF of about $0.28''$. The condition that the slit width should be smaller than the PSF width, cf.Chap. 2.6.2, is not fulfilled. Thus, a simple method to reduce instrumental artefacts was not applied here because the CRIRES instrument did not allow for smaller slit widths than $0.2''$ at the time of observations[2]. The individual exposures of both targets, which consist of NDIT=10 integrations of one second, have continuum signal-to-noise ratios of up to 1000. According to Eq. (2.6), this corresponds to a spatial resolution limit[3] of $\Delta = 0.5$ mas for a FWHM of $0.8$ mas. Co-adding all exposures which have been obtained at a specific position angle, a S/N of about 5000 and 6500 is achieved for RS Vir and TW Oph, respectively. These S/N ratios correspond to a theoretical resolution limit of $\Delta = 0.1$ mas and $\Delta = 0.08$ mas, respectively.

Figure 4.1 shows a typical spatial profile of the data set. The FWHM of the profile shown in
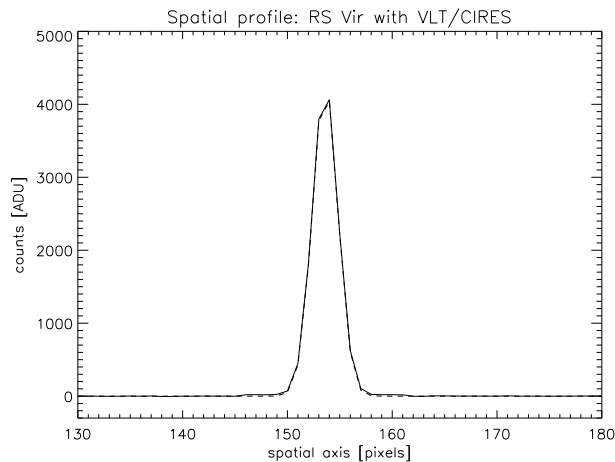


Figure 4.1: A typical spatial profile of the CRIRES data set (solid line), taken from a RS Vir longslit spectrum. The scale of the x-axis is in pixels, the one of the y-axis in counts. The FWHM is 2.9 pixels. Overplotted, but barely distinguishable, is the best-fitting Gaussian profile (dashed line).

the figure is 2.9 pixels, the range of FWHMs over the whole data set is $2.6 - 4.2$, depending on the atmospheric seeing and the performance of the adaptive optics. Comparing these values with Fig. 2.3, it becomes clear that the profile sampling is optimal, and that there are no additional errors because of small profile widths.

The assumption of a Gaussian profile is well justified for the CRIRES data: the best-fitting Gaussian is overplotted in Fig. 4.1. Both profiles, the real one and the fit, can hardly be distinguished from each other. As the S/N of the data is very high, too, all prerequisites

---

[2]Recently, slit widths of down to $0.05''$ may be applied, though at the risk of unforeseen drawbacks as the instrument was not designed for such slit widths.

[3]As discussed in Sect. 2.3, *spatial resolution* means an effective, intensity-weighted spatial resolution.

made in Chap. 2 are fulfilled. Hence, the analysis tools described there are expected to work without restrictions.

After the steps of data reduction and spectro-astrometric extraction, for every exposure of the targets and the telluric standard stars, the extracted quantities of $\mathcal{C}(\lambda)$, $\mathcal{W}(\lambda)$ and $f(\lambda)$, the spectral energy distribution, are available. In the following analysis, only these quantities are used.

Figure 4.2 depicts two raw $\mathcal{C}(\lambda)$ spectra of RS Vir. The time spacing between the exposures
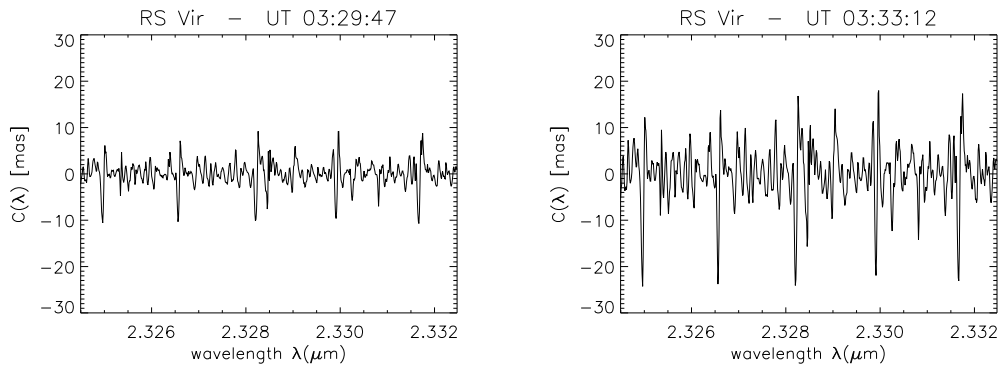


Figure 4.2: Two $\mathcal{C}(\lambda)$ spectra extracted from two exposures which were taken 3.5 minutes apart. The changes in $\mathcal{C}(\lambda)$ are entirely caused by the varying artefacts.

is about 3.5 minutes. The signatures which can be seen are dominated by instrumental artefacts. Since possibly underlying target-intrinsic features are not expected to change significantly on such short time scales, any changes in $\mathcal{C}(\lambda)$ are only caused by changing artefacts. These changes are induced by varying atmospheric conditions and/or a varying degree of adaptive optics correction. This clearly shows the need to correct for the artefacts individually for each exposure. Because here the shape of the artefacts remains almost constant and only the amplitude changes, it is expected that the effective PSF also remains constant, and that the changing width of the seeing is responsible for the changes in $\mathcal{C}(\lambda)$, cf. Sect. 4.3.1.

As described in Sect. 2.6.2, target-intrinsic kinematic spectro-astrometric signatures may influence the artefact removal algorithm. In this case, a strong improvement of the removal success can be achieved if a sufficient number of telluric lines is present in the spectra and if only those are used as input for the removal algorithm. Cool or hot spots on stellar surfaces lead, in contrast, to purely spatial signatures and, hence, telluric lines are not absolutely necessary for the analysis conducted here. Nevertheless, a comparison was done between the removal procedure performed only with telluric lines and the procedure performed without telluric lines, see the next two sections. As a first step, the spectrum of the standard stars have been inspected to identify telluric lines, see Fig. 4.3. Both spectra are identical with the exception of very few weak lines. Since the SED of the two B-type stars is flat in the wavelength region shown in the figure, any absorption line is a telluric line of the Earth's atmosphere. The number of telluric lines on the other three detectors is small. However, it is still sufficient in order to find some lines that are not strongly blended with the CO-lines in the giant star spectra. Under the assumption that the effective PSF of the instrument does not vary strongly within the wavelength range covered by one detector, there is no need for a uniform distribution of the telluric lines. This assumption is later-on shown to be valid, cf. Sect.s 4.3.1, 4.3.2 and 4.4. The principle idea here is that if the best-fitting effective PSFs obtained for the four detectors of a single exposure match well, the instrumental profile is proven to be nearly constant
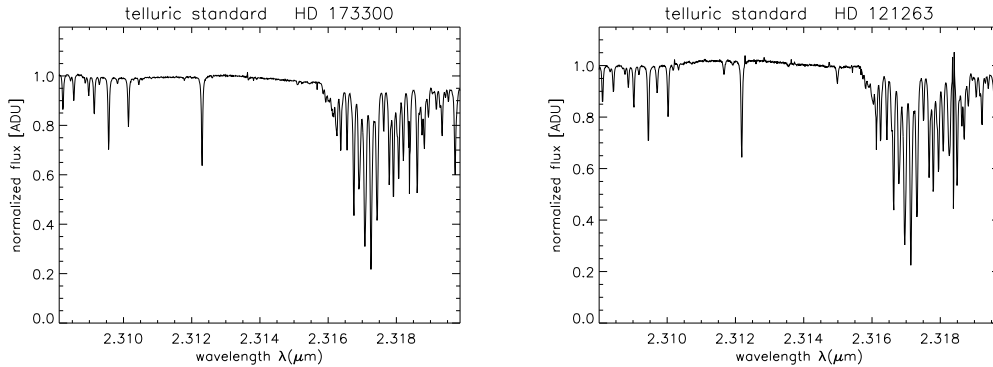
Figure 4.3: Normalised SEDs of the telluric standard stars HD 173300 (left plot) and HD 121263 (right plot). As both stars are of spectral type B, the stellar SEDs are flat in this wavelength region. Hence, any spectral absorption line is a telluric line of the Earth's atmosphere. Most of the lines visible here are caused by methane; some of the lines at the lower wavelength side are from water.

over the wavelength region of interest. Furthermore, it is of advantage that telluric lines do not need to be removed from the target longslit spectrum for the spectro-astrometric analysis. This is true because telluric lines only lead to instrumental artefacts in $\mathcal{C}(\lambda)$ and $\mathcal{W}(\lambda)$ but do not contribute at all to those two quantities after the artefact removal. Telluric lines, nevertheless, need to be removed from the extracted SED of the target in order to find the best-fitting synthetic model atmosphere spectrum.

In the following two sections, the artefact removal and the source modelling, see Sects. 2.6.2 and 2.7, respectively, are discussed for RS Vir and TW Oph individually. No formal errors are given for the spectro-astrometric quantities as well as for the deduced best-fitting source configurations because residual instrumental artefacts and model uncertainties due to the synthetic spectra and few slit orientations do not allow to formally determine the errors.

### 4.3.1 Results on RS Vir

#### 4.3.1.1 Artefact removal

A plot of a raw $\mathcal{C}(\lambda)$ and $\mathcal{W}(\lambda)$ spectrum is shown in Fig. 4.4, upper left panel. Both quantities were obtained by averaging the quantities of all individual NDIT=10-exposure at the position angle of 0°. The average spectra are plotted in Fig. 4.4. This is done to better visualise the different performance of the three artefact removal procedures as the equivalent plots for individual exposures are quite noisy. Strong signatures are clearly visible in $\mathcal{C}(\lambda)$ and $\mathcal{W}(\lambda)$ at each line of the target's SED and at each telluric line. Thus, these signatures are instrumental artefacts with an amplitude in the absorption lines of about 10 and 15 mas in $\mathcal{C}(\lambda)$ and $\mathcal{W}(\lambda)$, respectively, for the averaged quantities. The amplitudes vary for the individual exposures over the whole data set between 13 and 35 mas in $\mathcal{C}(\lambda)$ and 15 and 40 mas in $\mathcal{W}(\lambda)$. The average values are 15 and 22 mas for $\mathcal{C}(\lambda)$ and $\mathcal{W}(\lambda)$, respectively. In contrast, the S/N-limited spatial resolution is 0.5 and 1.1 mas for $\mathcal{C}(\lambda)$ and $\mathcal{W}(\lambda)$, respectively, for individual exposures, and 0.1 and 0.2 mas for the total S/N per slit orientation over the whole data set, for $\mathcal{C}(\lambda)$ and $\mathcal{W}(\lambda)$, respectively. A perfect artefact removal would, hence, reduce the noise[4] of the spectro-astrometric quantities to the corresponding S/N-limited levels.

---

[4]Here, the term *noise* is only true if the S/N-limited resolution is achieved. Otherwise, it denotes the instrumentally induced variations which act as a resolution limit.
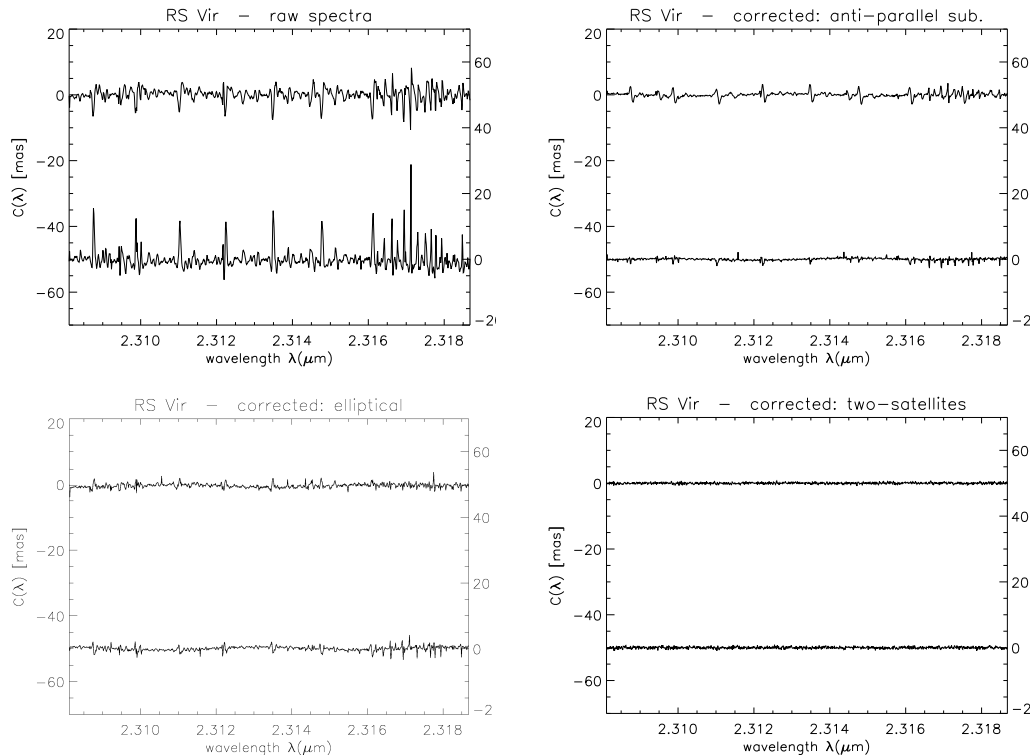
Figure 4.4: Raw $\mathcal{C}(\lambda)$ (upper curve) and $\mathcal{W}(\lambda)$ (lower curve) spectra of RS Vir at a position angle of 0°. The upper left plot shows the state before artefact removal. The same quantities after artefact correction using anti-parallel subtraction, an elliptical PSF parameterisation and a two-satellite-parameterisation are depicted in the upper right, lower left and lower right, respectively.

Using an elliptical PSF parameterisation, the removal algorithm yielded corrected $\mathcal{C}(\lambda)$ and $\mathcal{W}(\lambda)$ spectra as shown in Fig. 4.4, lower left subplot. As there remain kinematic-like signatures at the positions of target and telluric spectral lines, these are residual artefacts, though at smaller amplitude of about 4 and 3 mas for $\mathcal{C}(\lambda)$ and $\mathcal{W}(\lambda)$, respectively, for the individual exposures. Since the amplitudes of signatures of surface spots are expected to be similar to these residuals, this performance is not satisfactory. Executing the removal process for each exposure of the data set, one can study whether the best-fitting PSF configuration changes from frame to frame, cf. Tab. 4.1. The angle $\phi$ is measured with respect to the slit axis and, hence, is not corrected for different slit orientations. From the values given in the table, it is obvious that the width of the effective seeing (i.e., $P$) varies the strongest, whereas the variations in the orientation of the ellipse $\phi$ and of the eccentricity $a/b$ are limited. This points out that the instrumental profile itself does not change much with time but the atmospheric seeing does. The variations of $\phi$ and $a/b$ may be caused by a changing degree of wavefront correction by the adaptive optics. This has been reported in several studies, as e.g. in Brannigan et al. (2006). Mechanical flexure and thermal expansion of the telescope/instrument system also affect the instrumental profile. There is no dependency of the PSF parameters on slit orientation or time. As the parameters neither vary strongly between the four detectors of an exposure nor between the data of the three target stars of this work, these PSFs seem to really represent the instrumental profile. Experimental analysis of archival data obtained with other instruments [5] yielded significantly different PSF configurations which strengthen this interpretation. The table

---

[5]Data of these instruments were tested: VLT/ISAAC, VLT/UVES, HST/STIS.

Table 4.1: A sample of best-fitting PSF parameters for the elliptical scenario for some individual exposures of RS Vir at position angles of 0°, 90°, 180° and 270°.

| exp., PA | $\phi\,[°]$ | $a/b$ | $P\,['']$ | $\mathcal{C}(\lambda)\,[\text{mas}]$ | $\mathcal{W}(\lambda)\,[\text{mas}]$ |
|---|---|---|---|---|---|
| #1, 0° | 34.2 | 1.23 | 0.87 | 4.1 | 2.9 |
| #2, 0° | 30.7 | 1.08 | 1.25 | 4.4 | 3.2 |
| #3, 0° | 37.3 | 1.15 | 1.03 | 3.8 | 2.8 |
| #1, 90° | 29.4 | 1.20 | 1.07 | 4.0 | 3.0 |
| #2, 90° | 34.1 | 1.27 | 1.31 | 4.2 | 3.1 |
| #3, 90° | 36.5 | 1.11 | 1.12 | 4.1 | 3.0 |
| #1, 180° | 31.1 | 1.18 | 0.81 | 3.8 | 3.1 |
| #2, 180° | 36.2 | 1.22 | 0.96 | 3.9 | 3.0 |
| #3, 180° | 38.7 | 1.13 | 1.33 | 4.2 | 3.3 |
| #1, 270° | 28.7 | 1.23 | 0.81 | 3.8 | 2.8 |
| #2, 270° | 34.4 | 1.11 | 1.45 | 4.0 | 3.2 |
| #3, 270° | 31.2 | 1.27 | 1.10 | 4.4 | 3.3 |

also lists the amplitudes of the residual artefacts after correction. These amplitudes serve as an indicator of the goodness of the removal procedure. Here, the residuals are about a factor of 8 and 3 higher than the S/N-limit for $\mathcal{C}(\lambda)$ and $\mathcal{W}(\lambda)$, respectively. The amplitude of the residuals do not vary strongly, too. An investigation of the fitting process of the artefact removal reveals that convergence is quickly achieved. The whole $\chi^2$-landscape was calculated for a few exposures, cf. 2.6.2. These landscapes confirm that there is one minimum which is by far the smallest $\chi^2$-value of the whole parameter set and convergence is strong, cf. Fig. 4.5.

Repeating the removal algorithm with a two-satellite PSF parameterisation yields much
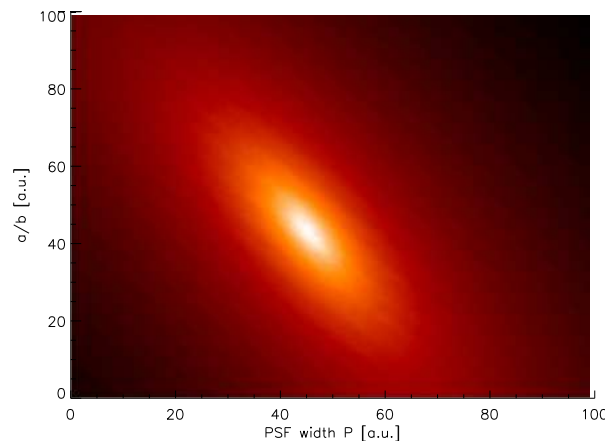


Figure 4.5: $\chi^2$ landscape of the artefact removal with elliptical parameterisation $a/b$, $P$ and $\phi$. The graph shows the results for fixed $\alpha = 42°$. The plot is a zoom on the total parameter space in $a/b$ and $P$.

better results, cf. Fig.4.4, lower right panel and cf. Tab. 4.2. The corrected $\mathcal{C}(\lambda)$ and $\mathcal{W}(\lambda)$ spectra do no longer contain visible features at the positions of spectral lines in the SED. Cross-correlation of the target SED including telluric lines with both spectro-astrometric quantities also does not yield any signs of correlation. The root-mean-square (rms) of $\mathcal{C}(\lambda)$

Table 4.2: Similar to Tab. 4.1 but for the two-satellite scenario: exposure number, position angle, $\phi$ of both satellites, their distances from the central component in milli-arcseconds, the intensities of the satellites relative to the central component, their width, width of the central component, residual rms-amplitude of $\mathcal{C}(\lambda)$ and $\mathcal{W}(\lambda)$ in mas.

| exp., PA | $\phi_1$ [°] | $\phi_2$ [°] | $d_1$ | $d_2$ | $I_1$ | $I_2$ | $w_1$ ["] | $w_2$ ["] | $w_0$ ["] | $\mathcal{C}$ | $\mathcal{W}$ |
|---|---|---|---|---|---|---|---|---|---|---|---|
| #1, 0° | 45.1 | -116.7 | 324 | 397 | 0.51 | 0.35 | 0.23 | 0.34 | 0.93 | 1.9 | 2.8 |
| #2, 0° | 40.9 | -119.9 | 330 | 388 | 0.48 | 0.37 | 0.30 | 0.46 | 1.24 | 1.6 | 2.3 |
| #3, 0° | 41.8 | -112.4 | 317 | 381 | 0.54 | 0.31 | 0.21 | 0.39 | 1.09 | 1.8 | 2.6 |
| #1, 90° | 47.2 | -113.0 | 310 | 382 | 0.47 | 0.32 | 0.25 | 0.33 | 0.98 | 1.5 | 2.1 |
| #2, 90° | 44.1 | -110.5 | 331 | 372 | 0.43 | 0.36 | 0.34 | 0.40 | 1.28 | 1.9 | 2.9 |
| #3, 90° | 42.2 | -115.0 | 315 | 377 | 0.53 | 0.29 | 0.30 | 0.37 | 1.10 | 1.7 | 2.6 |

and $\mathcal{W}(\lambda)$ are 1.7 mas and 2.6 mas, respectively. These values are still a factor of about 3 and 2.5 above the S/N-limit. This means that either the true PSF is more complex than the two-satellite description or that the basic assumption of the removal procedure is not entirely correct. Nevertheless, the performance of the two-satellite parameterisation is good enough to detect surface structures; the artefacts have been reduced by a factor of 8 to 10. The superior performance of the two-satellite parameterisation compared to the elliptical one is due to its greater flexibility in describing PSF configurations. As can be deduced from Tab. 4.2, the two-satellite solutions, too, indicate that the instrumental profile does not change as much with time as the seeing width does. Figure 4.6 images
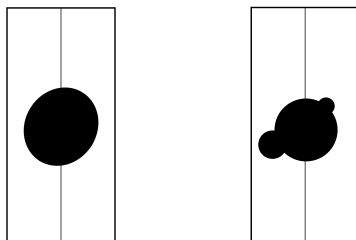


Figure 4.6: The best-fitting instrumental profile (PSF) obtained with the artefact removal algorithm for one exposure of the RS Vir data set. The left subplot shows the result for an elliptical parameterisation, the right one the results for a two-satellite parameterisation. The distances of the two satellites from the central component have been increased for a better visualisation. Compare Tabs. 4.1+4.2 for the specific values of the parameters.

the best-fitting PSF configuration for a single exposure for an elliptical PSF and for the two-satellite scenario. Table 4.2 lists the range of the best-fitting parameters for the two-satellite case over the whole RS Vir data set. Although these parameters do not vary strongly with time, the changes are large enough to necessitate an individual removal run for each exposure. A co-addition of exposures obtained at identical position angles was not performed because differences in the PSF, the trace and in the spatial profile of the longslit spectra might degrade the resulting spectro-astrometric quantities rather than improving them. In order to exploit the full S/N ratio of the combined exposure set, the extracted $\mathcal{C}(\lambda)$ and $\mathcal{W}(\lambda)$ spectra were averaged for each position angle. This procedure reduces the rms-amplitude to 0.27 mas and 0.43 mas in $\mathcal{C}(\lambda)$ and $\mathcal{W}(\lambda)$, respectively. These full-S/N-quantities are plotted in Fig. 4.4. The ratio of this accuracy to the theoretical resolution limit is equal to the ratio of the individual exposures, i.e., about 3. Despite the increased

accuracy, no signatures can be found in the combined spectra. A cross-correlation of the spectro-astrometric quantities with the target SED and with the simulated SEDs of some spot models, did not yield any evidence for features above the noise level. The same result was obtained for the exposures taken at a position angle of 90°. Hence, no surface structure were detected on RS Vir. Upper limits to surface coverage by cool/hot spots can be derived with source modelling in the next section.

Subtracting spectro-astrometric quantities obtained at anti-parallel slit orientations is another way to remove artefacts, cf. 2.6.2. As atmospheric conditions usually change on time scales smaller than the exposure time spacing, cf. Fig. 4.2, the potential of this method is limited. As long as only the seeing width changes with time and the instrumental profile stays constant, the performance of the anti-parallel subtraction can be improved by rescaling the spectro-astrometric quantities obtained at anti-parallel slit orientations to a common amplitude before subtraction. If the resulting spectra were to be used for spectro-astrometric analysis, this rescaling factor had to be considered during source modelling. However, the average performance of anti-parallel subtraction is bad. Even the best results, i.e., using rescaling and choosing the best-matching exposures, cannot achieve the level needed to detect surface features on giant stars. This proves that the PSF and/or instrumental profile does change too much for this method to work even though the changes in absolute figures are not large. Because of this, only more complex parameterisations, as, e.g., the two-satellite one do succeed in reaching the necessary levels of artefact removal. Figure 4.4 allows for a comparison of the different methods with the anti-parallel subtraction depicted in the upper right subplot.

### 4.3.1.2 Source modelling

In order to obtain upper limits on surface structure coverage for RS Vir, various object configurations were simulated using synthetic PHOENIX spectra. More details on those spectra are given in Sect. 4.1. As the first step, the observed SED of RS Vir was fitted with synthetic spectra. The a priori known effective temperature of 2160 K, cf. Tab. 3.1, was used as a starting point, and a micro-turbulence velocity of $\xi = 2\,\mathrm{km\,s^{-1}}$ was assumed. The latter is a typical value for micro-turbulence in giant stars. The surface gravity was varied between $\log(g) = -0.5 \ldots +0.5$. Figure 4.7 depicts the observed SED and the
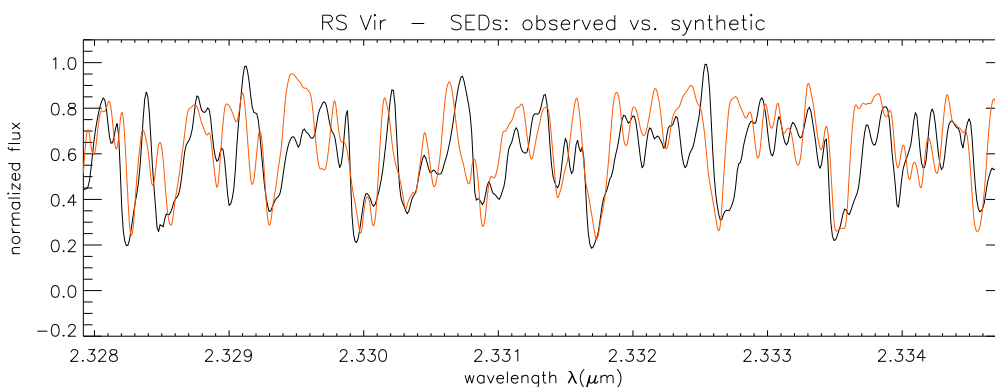


Figure 4.7: Observed and best-fitting synthetic SED of RS Vir. The fitting parameters are $T_{\mathrm{eff}}$ and $\log(g)$, here with values of $T_{\mathrm{eff}} = 2300\,K$ and $\log(g) = 0.0$.

best-fitting model. The overall agreement between the model and the observed spectrum is not good; it is at a similar level for all four detector chips. However, a better agreement could not be achieved with the available models. The best-fitting temperature of 2300 K is

Table 4.3: Here, some single-spot configurations are listed which represent the detection limit of the RS Vir data (subscript *data*). In addition, spot configurations are listed that match the theoretical detection limit of the data with respect to the S/N (subscript *S/N*), cf. Eq. (2.6). Tabulated are the values of the spot coverage factor $e$, the temperature contrast $\Delta T$ and the corresponding amplitude of the features $\mathcal{C}$ and $\mathcal{W}$. The longitude and latitude are always 0° and 30°, respectively.

|            | $e_{\mathrm{data}}$ | $e_{\mathrm{S/N}}$ | $\Delta T$ [K] | $\mathcal{C}$ [mas] | $\mathcal{W}$ [mas] |
|------------|------|------|--------|------|------|
| cool spots | 10   | 4.5  | $\leq$-500 | 0.29 | 0.18 |
|            | 18   | 7.5  | -300   | 0.30 | 0.19 |
| hot spots  | 10   | 4.0  | +500   | 0.27 | 0.17 |
|            | 8    | 3.3  | +800   | 0.29 | 0.19 |
|            | 6    | 2.4  | +1000  | 0.28 | 0.18 |

compatible with the a priori known effective temperature of 2160 K, in particular because the uncertainties of synthetic spectra are large for cool supergiants. The fit was obtained only using CO lines. Had there been data in another spectral range, the significance of the best-fitting parameter set would be higher. Using this parameter set, models with lower/higher effective temperature were calculated. Therewith, the spectro-astrometric signatures of cool/hot spots were simulated placing a single spot at mid-latitudes on the stellar disk. The temperature contrast of the spot with respect to the background atmosphere was varied as well as the size of the spot. The configurations which result in signatures with amplitudes right at the noise level of the observations define the detection limit. Some examples are given in Tab. 4.3. These examples refer to the detection limit of the total S/N per slit orientation. The values of the simulated $\mathcal{C}(\lambda)$ and $\mathcal{W}(\lambda)$ amplitudes stress one problematic issue: the S/N-limited spatial resolution is larger in $\mathcal{C}(\lambda)$ than in $\mathcal{W}(\lambda)$, cf. Eq. (2.6), but the spot signatures are also larger in $\mathcal{C}(\lambda)$ than in $\mathcal{W}(\lambda)$. This reduces the significance of the constraints on the best-fitting spot geometry if the observed features are only slightly above the detection limit. Placing the spot a high longitudes decreases the spectro-astrometric signatures as the visible area of the spot also decreases. Increasing the latitude leads to a slower reduction of the signatures because the increasing distance of the spot from the centre of the disk counters the decreasing visible area of the spot. Figure 4.7 shows that the $^{12}\mathrm{C}^{16}\mathrm{O}$ lines have a depth of about 0.8 because of the very low temperature of RS Vir. Those CO lines saturate in the synthetic models for temperatures lower than 1800 K. Hence, two spot scenarios with different temperatures cannot be distinguished with spectro-astrometry if both spot temperatures are below the saturation temperature because their spectral contrast is identical. The detection limits listed in Tab. 4.3 state that spots having typical sizes of super convection cells on supergiants can be found with the present data set. As consequence, it is concluded that no such structures existed at the time of observations on RS Vir. An optimal artefact removal would both allow to detect small spots and increase the significance of the detection of large spots. More complicated spot configurations using multiple spots lead to other detection limits. As there is a multitude of possible two-(or more)spot configurations, each with its own detection limit, no detailed list of these upper limits was calculated. The list of one-spot limits should be sufficient as a guideline for RS Vir. As a final result on the RS Vir data, detection limits were also calculated for the case that the theoretical resolution limit of Eq. (2.6) was achieved, i.e., the artefact removal worked perfectly. These values also are presented in Tab. 4.3 and allow to assess the optimal performance of spectro-astrometry at the given S/N. More figures concerning the data of RS Vir are given in the appendix.

## 4.3.2 Results on TW Oph

### 4.3.2.1 Artefact removal

In analogy to Sect. 4.3.1, the artefact removal was done using an elliptical and the two-satellite parameterisation as well as using the anti-parallel subtraction. The resulting corrected quantities are depicted for the averaged $\mathcal{C}(\lambda)$ and $\mathcal{W}(\lambda)$ spectra of TW Oph at a position angle of $0°$ in Fig. 4.8. The artefacts in the raw spectra have amplitudes between
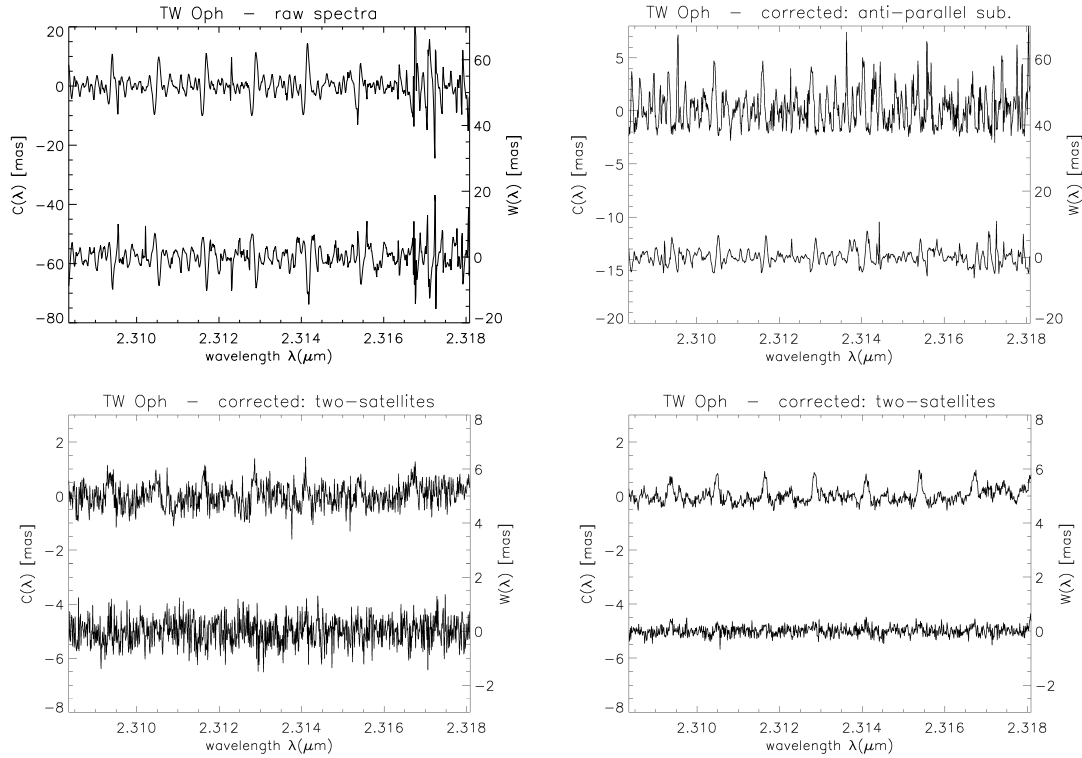


Figure 4.8: Same as Fig. 4.4, but for TW Oph at a position angle of $0°$. The y-axes scales of the plots are not identical in order to better depict the target-induced signatures.

13 and $30\,\mathrm{mas}$ in $\mathcal{C}(\lambda)$ and 15 and $36\,\mathrm{mas}$ in $\mathcal{W}(\lambda)$. The performance of the different removal methods is similar to the case of RS Vir. The residual artefact amplitudes are summarised in Tab. 4.4 for the two-satellite case. They vary between 1.2 and $1.6\,\mathrm{mas}$ in $\mathcal{C}(\lambda)$ and 1.8 and $2.3\,\mathrm{mas}$ in $\mathcal{W}(\lambda)$ for individual exposures. These amplitudes were determined from the residuals in the telluric lines only, as the corrected $\mathcal{C}(\lambda)$ and $\mathcal{W}(\lambda)$ spectra clearly show target-induced signatures which do not appear at the position of the telluric lines. The shape of the features point to a purely spatial origin with no significant velocity field. This means that the radial velocities of the corresponding surface features are small. The best-fitting PSFs for both parameterisations are depicted in Fig. 4.9 for one exposure at a position angle of $0°$. As the target-induced features are of spatial origin, the artefact removal procedure can safely be applied using all spectral lines. A comparison of the results obtained only with telluric lines and the results obtained with all lines did not yield significant differences. The convergence of the PSF-fitting is as strong as in the case of RS Vir; compare Fig. 4.10 with Fig. 4.5. This is important because there is no danger of the fitting procedure getting stuck in a local minimum. The $\chi^2$ distributions over two out of the ten parameters of the two-satellite scenario look similar in the way that there is a strong convergence and no significant local minima. As can be seen from

Table 4.4: Similar to Tab. 4.1 but for TW Oph for the two-satellite scenario: exposure number, position angle, $\phi$ of both satellites, their distances from the central component in milli-arcseconds, the intensities of the satellites relative to the central component, their width, width of the central component, residual rms-amplitude of $\mathcal{C}(\lambda)$ and $\mathcal{W}(\lambda)$ in mas.

| exp., PA | $\phi_1$ [°] | $\phi_2$ [°] | $d_1$ | $d_2$ | $I_1$ | $I_2$ | $w_1$ [″] | $w_2$ [″] | $w_0$ [″] | $\mathcal{C}$ | $\mathcal{W}$ |
|---|---|---|---|---|---|---|---|---|---|---|---|
| #1, 0° | 50.2 | -151.9 | 382 | 320 | 0.54 | 0.34 | 0.17 | 0.35 | 0.81 | 1.2 | 1.9 |
| #2, 0° | 54.8 | -153.1 | 395 | 310 | 0.51 | 0.39 | 0.24 | 0.43 | 1.08 | 1.4 | 2.1 |
| #3, 0° | 51.0 | -155.2 | 379 | 306 | 0.57 | 0.30 | 0.20 | 0.37 | 1.00 | 1.3 | 2.0 |
| #1, 90° | 57.7 | -156.5 | 383 | 316 | 0.42 | 0.26 | 0.30 | 0.51 | 1.24 | 1.6 | 2.3 |
| #2, 90° | 55.0 | -150.8 | 370 | 300 | 0.61 | 0.33 | 0.10 | 0.32 | 0.65 | 1.2 | 1.8 |
| #3, 90° | 51.3 | -149.1 | 389 | 312 | 0.52 | 0.36 | 0.19 | 0.41 | 0.92 | 1.4 | 2.0 |
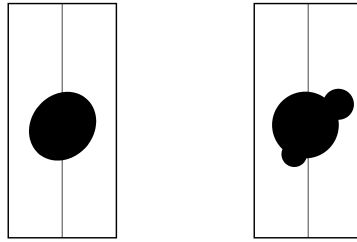


Figure 4.9: The best-fitting instrumental profile (PSF) obtained with the artefact removal algorithm. The left subplot shows the result for an elliptical parameterisation, the right one the results for a two-satellite parameterisation. Compare Tab. 4.4 for the specific values of the parameters.
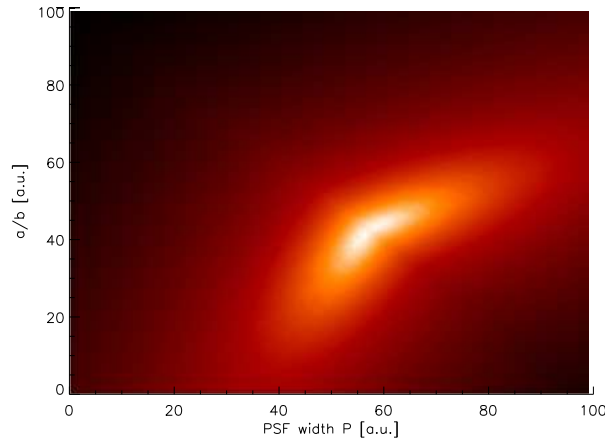


Figure 4.10: $\chi^2$ landscape of the artefact removal with elliptical parameterisation $a/b$, $P$ and $\phi$. The graph shows the results for fixed $\alpha = 52°$. The plot is a zoom on the total parameter space in $a/b$ and $P$.

Tab. 4.4, the instrumental profile changes more with time than in the case of RS Vir but again the variation in the seeing width are larger than those of the other PSF parameters. Similarly to the previous section, the two-satellite removal outperforms the other methods by far with no visible residual instrumental features in $\mathcal{C}(\lambda)$ and $\mathcal{W}(\lambda)$. The average residuals in $\mathcal{C}(\lambda)$ and $\mathcal{W}(\lambda)$ are a factor 2.3 and 2.5, respectively, larger for the elliptical

parameterisation compared to the two-satellite parameterisation. With the latter, the artefacts have been reduced by a factor of 12 and 60 to 1.5 mas and 0.27 mas in $\mathcal{C}(\lambda)$ for individual exposures and the averaged quantities, respectively. The residual noise at the position of the telluric lines is still a factor of 3.5 larger than the S/N-limit which is at 0.5 and 0.08 mas for individual and averaged $\mathcal{C}(\lambda)$, respectively. Experiments with even more complex PSFs did not yield any improvement: as any PSF configuration can be constructed by an N-satellite model, increasing the number of satellites should ultimately lead to a perfect artefact removal, if the basic assumption of the procedure is valid. Because the number of possible 2D-PSF-configurations increases tremendously with increasing N, it is not possible to routinely use values of $N > 2$. An N=3 model was applied to a single TW Oph exposure but with no improvement over the N=2 model. The N=3 run does not achieve a better noise level than the N=2 run. This could mean that the basic assumption, i.e., any instrumental effect can be represented by an effective PSF, is not strictly correct. Processing those exposures of TW Oph which have been obtained at a position angle of 90° leads to a similar quality of artefact removal. In contrast, the corrected $\mathcal{C}(\lambda)$ and $\mathcal{W}(\lambda)$ spectra do not contain any target-induced signatures above the noise level, cf. Fig. 4.11. This points to an orientation of the surface structure along the north-south direction
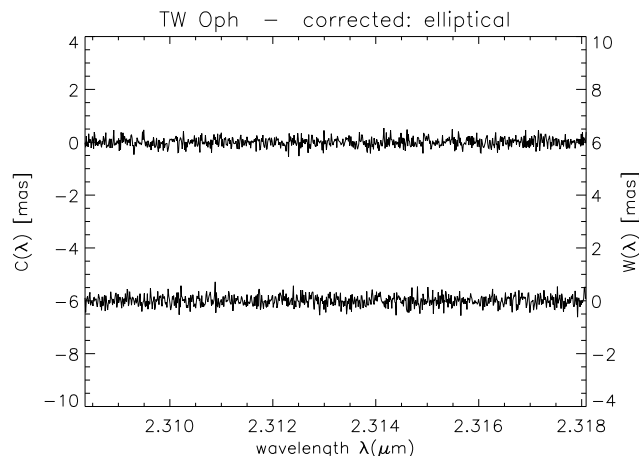


Figure 4.11: Depicted are the artefact-corrected $\mathcal{C}(\lambda)$ and $\mathcal{W}(\lambda)$ spectra for TW Oph which have been obtained at a position angle of 90°. Here, the two-satellite parameterisation was applied. In contrast to the exposures at a PA of 0°, no target-induced signatures above the noise level are present.

on the stellar disk. The spectro-astrometric quantities obtained at the anti-parallel slit orientations of 180° and 270° confirm this assumption: the 180°-spectra do contain target-induced features whereas the 270°-spectra do not.

### 4.3.2.2 Source modelling

The features in $\mathcal{C}(\lambda)$ and $\mathcal{W}(\lambda)$ seem to be of purely spatial origin with an average amplitude of about 1 and 0.4 mas, respectively. Considering the apparent diameter of TW Oph, 10 mas, and assuming an arbitrary contrast of 0.2 in the CO-lines leads to a very rough guess of signatures having amplitudes of 1 mas if a spot were present at mid-latitudes covering 20 % of the visible stellar disk. The source modelling is studied in the following in some detail.

The procedure of source modelling was performed in analogy to that one described for RS Vir in Sect. 4.3.1. The a priori known effective temperature of 2400 K, cf. Tab. 3.1,

was used as a starting point. Again, a micro-turbulence velocity of $\xi = 2\,\mathrm{km\,s^{-1}}$ was assumed and the surface gravity was varied between $\log(g) = -0.5\ldots+1.0$. Figure 4.12 illustrates the observed spectrum of TW Oph along with the best-fitting synthetic model.
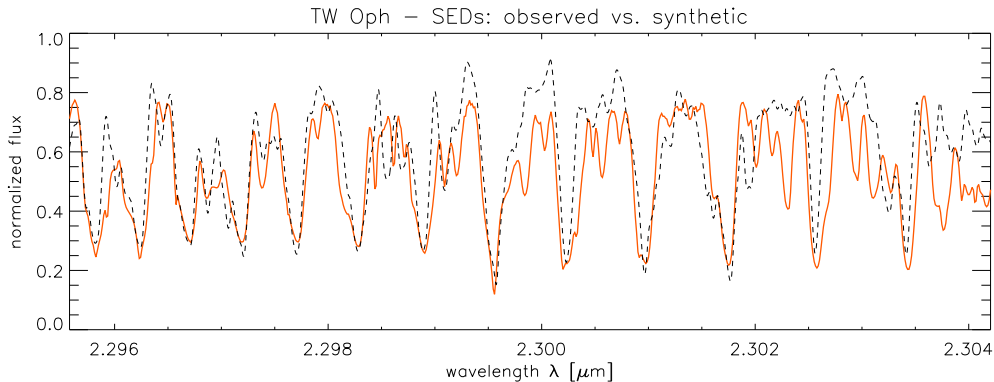


Figure 4.12: Observed (solid line) and best-fitting synthetic (dashed line) spectrum. The goodness-of-fit is similar for the other three detectors. The absorption lines in the observed spectrum which are missing in the synthetic spectrum above $2.302\,\mu m$ are telluric lines.

The parameters of this model are within the general range of stellar parameters for giant stars; specifically: $T_{\mathrm{eff}} = 2400$, $\log(g) = 0.5$, cf. Sect. 4.1. As discussed in Sect. 2.6.2, the procedures of fitting the target-SED and of modelling the source are, in principle, related to each other and quite difficult to conduct: the observed SED cannot be fitted by a single synthetic atmosphere as possibly present spots do influence the total SED. Hence, the SED should better be fitted by a linear combination of two or more synthetic model spectra, representing the background atmosphere and the spot(s). Even this ansatz would not be correct as a synthetic model is necessary which considers such spots as caused by, e.g., giant convection cells. A detailed 3D-model has been devised for Betelgeuse by Freytag et al. (2002). It allows to calculate images of the surface which are formed by convection but it does not provide a stellar spectrum. However, the modelling of supergiant atmospheres is, to date, not very accurate. In addition, a whole model grid covering a range of effective temperature, surface gravity, micro-turbulence velocity, element abundances etc. would be needed to optimally find the best-fitting model for TW Oph. This is beyond the scope of this work. With the models available here, the best-fit was found to be that one shown in Fig. 4.12. A simplified source modelling method was applied: a single synthetic model was fit to the observed SED in order to obtain the parameters of the background atmosphere. The source modelling, then, was done using synthetic models with lower/higher effective temperature as representation of cool/hot spots, keeping the other parameters constant. Figure 4.13 depicts the depth of the $^{12}\mathrm{C}^{16}\mathrm{O}$ lines versus effective temperature of the synthetic models at $2.300\,\mu m$. A simple spot geometry was assumed together with a temperature contrast of the spot(s), and the spectro-astrometric quantities were evaluated for two orthogonal slit orientations. First, a single cool/hot spot was simulated at mid-latitudes as in the case of RS Vir. The temperature contrast and the disk coverage factor was varied, and the goodness-of-fit to $\mathcal{C}(\lambda)$ and $\mathcal{W}(\lambda)$ was determined for both position angles. Figure 4.14 presents the observed, averaged $\mathcal{C}(\lambda)$ and $\mathcal{W}(\lambda)$ of TW Oph at a position angle of $0°$ as well as some of the model position spectra. The graph also illustrates that two-spot configurations do not fit the data, see below in this section. There is a class of best-fitting models and not just a single model. Some examples are listed in Tab. 4.5. This model-degeneracy exists because observations have only been conducted at two orthogonal slit orientations. From the table, it can be seen that different temperature
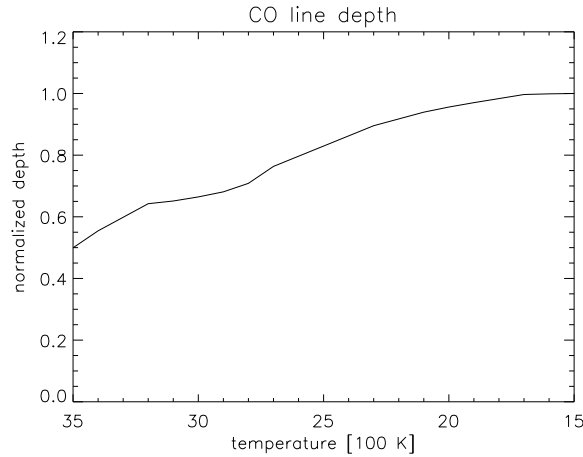
Figure 4.13: Depicted is the average $^{12}$C$^{16}$O line depth of the synthetic models used for TW Oph in the wavelength region of $2.292 - 2.304\,\mu m$.
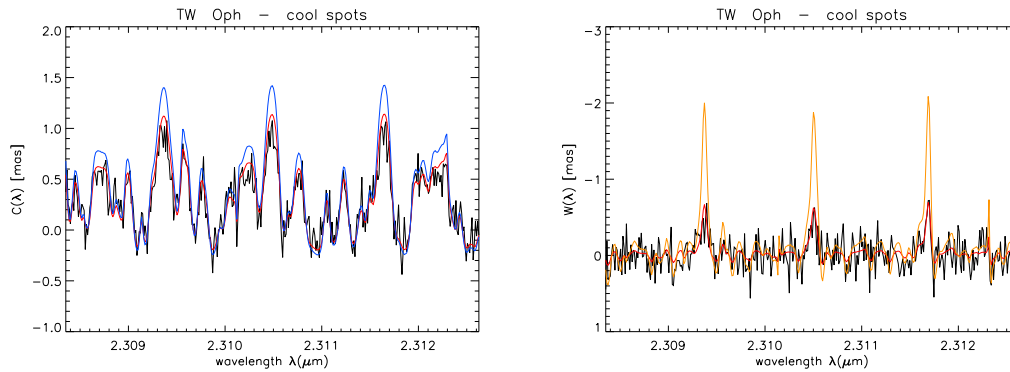


Figure 4.14: On the left, the observed $\mathcal{C}(\lambda)$ (black line) is plotted together with the best-fitting single cool spot scenario of $\Delta T = 500\,\mathrm{K}$, $e = 11\,\%$ (red line) and another sub-optimal scenario of $\Delta T = 600\,\mathrm{K}$, $e = 13\,\%$ (blue line). For a scenario with two identical spots, one on each hemisphere, the $\mathcal{C}(\lambda)$ spectrum alone was fitted for. The result is also identical with the red line. The right panel features the $\mathcal{W}(\lambda)$ of the observed data (black line), the best-fitting one-spot scenario (red line) and the two-spot scenario (orange line). The latter is way off the observed data, ruling out the model.

contrast- and spot size- pairs lead to identical results: e.g., a spot of $e = 11\,\%$ disk coverage with $\Delta T = 500\,\mathrm{K}$ and $e = 19\,\%$ with $\Delta T = 300\,\mathrm{K}$. As the coverage factor is larger for the latter pair, the signatures also are larger. This increase is compensated by the smaller temperature contrast which results in a smaller spectral contrast that is, in turn, accompanied by a decrease in the spectro-astrometric signatures. The longitude of the spot has to be close to zero[6] in order to fit the observations. For non-zero longitudes with respect to the slit orientations applied during observation, signatures would have been detected at both slit orientations. Figure 4.15 visualises some of the best-fitting models. Had there been observations at more than two independent slit orientations, this degeneracy in the best-fitting models could have been resolved. Spots at higher and lower latitudes can lead to good fits of the spectro-astrometric quantities as well. However, the fit quality is not as high as for mid-latitude spots. Spots at very low or even zero latitude can be excluded as

---

[6]if zero longitude is defined to be the middle of the visible stellar disk

Table 4.5: Listed are those single spot geometries which fit the $\mathcal{C}(\lambda)$ and $\mathcal{W}(\lambda)$ spectra of TW Oph best at both position angles simultaneously. The coverage factor, temperature contrast and the resulting average $\mathcal{C}(\lambda)$ and $\mathcal{W}(\lambda)$ feature amplitudes are tabulated. The cool spot scenarios slightly better agree with observations than the hot spot scenarios, see text.

|            | $e$ | $\Delta T$ [K] | $\mathcal{C}$ [mas] | $\mathcal{W}$ [mas] |
|------------|-----|----------------|---------------------|---------------------|
| cool spots | 8   | -800           | 1.09                | 0.62                |
|            | 11  | -500           | 1.01                | 0.60                |
|            | 19  | -300           | 0.97                | 0.59                |
| hot spots  | 20  | +300           | 1.03                | 0.60                |
|            | 12  | +500           | 0.98                | 0.58                |
|            | 9   | +1000          | 1.06                | 0.61                |
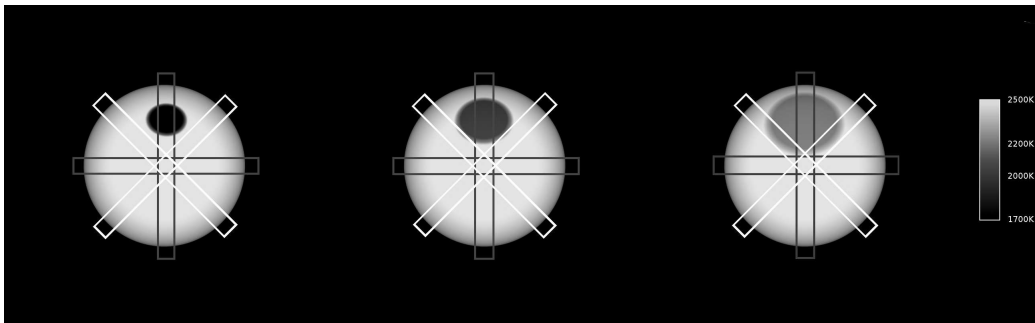


Figure 4.15: Shown are three best-fitting single cool spot models. The grey rectangles illustrate the two slit orientations applied during observing. The two further orientations depicted in white would have allowed for a discrimination of the three scenarios. The temperature scale is given on the far right.

they would not lead to any features in the $\mathcal{C}(\lambda)$ spectra. Stellar magnetic fields that cross the surface of a star induce cool spots. This is the cause for sun spots. In giant stars, however, the existence of similar magnetic fields is not proven. The source of cool and hot spots is more likely to be large-scale convection. Convection brings hotter gas cells from the stellar interior to the surface. The gas cools with time and again reaches the temperature of the background atmosphere. Large-scale convection may also lead to regions that are cooler than the surrounding atmosphere, cf. Dorch (2004); Freytag et al. (2002). The large scale of the convection cells in comparison to the sun is caused by much larger pressure scale heights in the surface layers of the atmosphere, cf. Schwarzschild (1975). For the TW Oph data, hot spots are also a possible solution to the observed $\mathcal{C}(\lambda)$ and $\mathcal{W}(\lambda)$ spectra, though, at a lower level of significance. This, of course, is again depending on the synthetic models. The best hot spot solutions are also listed in Tab. 4.5.

More complex spot configurations were also investigated as possible sources of the observed signatures. It turned out that two or more spots result in poor fits to the observed data. This is not unexpected for two reasons: first, the spots would have to be aligned along the north-south direction on the surface as spectro-astrometric signatures are only detected for this slit orientation; and second, more than one spot leads to either very similar features or very different ones compared to the one-spot scenario. The former is the case if the spots are closely grouped on the surface; then, they cannot be distinguished from the one-spot model because of only two slit orientations. The latter is true if spots

Table 4.6: Here, some single-spot configurations are listed which represent the detection limit of the TW Oph data (subscript *data*). In addition, spot configurations are listed that match the theoretical detection limit of the data with respect to the S/N (subscript *S/N*), cf. Eq. (2.6). Tabulated are the values of the spot coverage factor $e$, the temperature contrast $\Delta T$ and the corresponding amplitude of the features $\mathcal{C}$ and $\mathcal{W}$ for the *data* case. The longitude and latitude are always 0° and 30°, respectively.

|  | $e_{\mathrm{data}}$ | $e_{\mathrm{S/N}}$ | $\Delta T$ [K] | $\mathcal{C}$ [mas] | $\mathcal{W}$ [mas] |
|---|---|---|---|---|---|
| cool spots | 5 | 2.2 | -800 | 0.26 | 0.15 |
|  | 9 | 4.0 | -500 | 0.28 | 0.17 |
|  | 15 | 6.6 | -300 | 0.28 | 0.16 |
| hot spots | 17 | 7.5 | +300 | 0.27 | 0.17 |
|  | 11 | 4.8 | +500 | 0.27 | 0.17 |
|  | 7.5 | 3.3 | +1000 | 0.26 | 0.16 |

are placed, e.g., on different hemispheres; then, the features in $\mathcal{C}(\lambda)$ are weaker and the features in $\mathcal{W}(\lambda)$ stronger than for the single-spot model. If both spots have identical size and temperature contrast, the features in $\mathcal{C}(\lambda)$ will vanish and those in $\mathcal{W}(\lambda)$ will double, cf. Fig. 4.14. This, again, stresses the need to simultaneously fit the $\mathcal{C}(\lambda)$ and the $\mathcal{W}(\lambda)$ spectra to obtain reasonable results. As only single spots fit the data fairly well, multiple-spot models with widely separated spots are unlikely for the TW Oph data.

To explore the full potential of spectro-astrometry, the detection limits of single spots on TW Oph were calculated for the spatial resolution achieved with artefact removal and for the case that the S/N-limited spatial resolution was achieved; cf. Tab. 4.6. The table shows that the full S/N-limited spatial resolution would allow to detect spots as small as 2.5 % of the visible disk. More graphs on the TW Oph data can be found in the appendix. Other scenarios as a source of the observed spectro-astrometric signatures like, e.g., a binary object or a surrounding disk could be excluded. The combination of the shape of the features, their amplitude and their dependence on wavelength is not consistent with most of such source configurations. If there existed a completely different scenario which lead to the same signatures, additional observations at other wavelength could still allow to confirm it or rule it out.

## 4.4 α Cen A

The α Cen A data also have been obtained with the VLT/CRIRES instrument. In contrast to the giant star data, six slit orientations, 011°, 101°, 146°, 191°, 281° and 326° have been applied. The observations were performed in the fundamental CO-line region at 4.6 μm. The sky background is much brighter than in the K-band, limiting the integration time lest the background saturates. A signal-to-noise ratio of about 120 per exposure and 700 in total per slit orientation was achieved on this target, allowing for a theoretical spatial resolution of 4 mas and 0.7 mas in $\mathcal{C}(\lambda)$, respectively, cf. Eq. (2.6).

### 4.4.1 Artefact removal

The removal procedure was applied as described for the giant star data set. The performance is equivalent, too. Figure 4.16 depicts a pair of raw $\mathcal{C}(\lambda)$ and $\mathcal{W}(\lambda)$ spectra as well as the two-satellite corrected ones. Interestingly, the residual noise after artefact
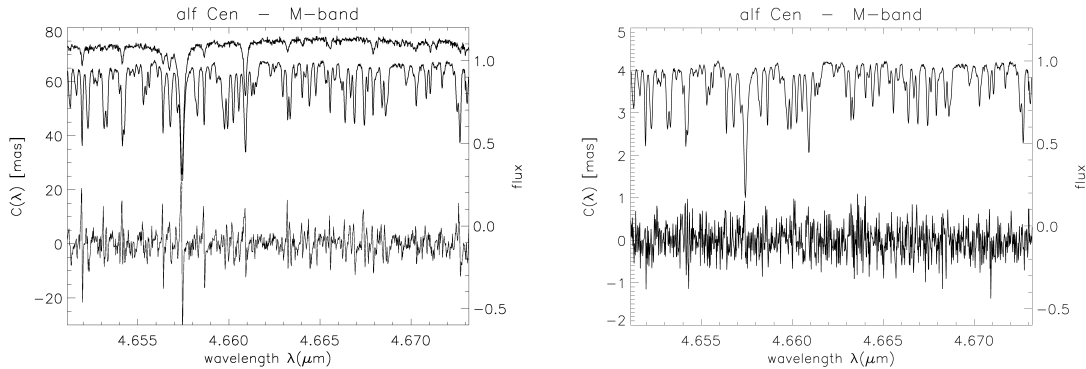
Figure 4.16: The raw $\mathcal{C}(\lambda)$ spectrum is shown in the left panel, lower curve. Also plotted in the the graph are the target SED (uppermost curve) as well as the SED of the telluric standard (below the target SED). The right panel depicts the target SED only (upper curve) and the corrected $\mathcal{C}(\lambda)$ spectrum (lower curve). The latter has been averaged over all exposures at a position angle of $0°$.

correction and averaging is about 1 mas which is almost as good as the S/N-limited value: the factor between theoretical and observational resolution is only 1.4. This accuracy is achieved for all six position angles. Because of the significantly lower S/N, the spatial resolution falls short compared to the giant data set. It remains unclear why the artefact correction here is almost perfect but misses the theoretical limit by a factor of three in case of the giant data set. A possible explanation is that, here, the instrumental PSF is closer to the two-satellite scenario than in the giant star case, but it is unclear why this should be true. The only difference between the two data sets is the wavelength range and the S/N of the data. Figure 4.16 also shows the SED of the telluric standard star. Obviously, there are only few telluric lines in the wavelength range of this detector. For two of the four detectors, the spectra are dominated by strong telluric lines with almost no significant stellar absorption lines. The best-fitting two-satellite PSF is illustrated in Fig. 4.17, and resembles the one obtained for TW Oph and RS Vir. The range of the
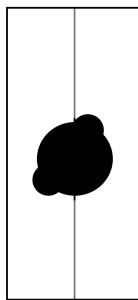


Figure 4.17: Typical PSF configuration obtained with the two-satellite artefact removal procedure for the data of $\alpha$ Centauri A. The distances of the two satellites from the central component have been increased for a better visualisation. Compare Tab. 4.7 for the variations of the PSF-parameters over the data set.

best-fitting PSFs over the whole data set is presented in Tab. 4.7. The similarity of the PSFs between $\alpha$ Cen A and the giant star data as well as the similar range of variations over the data set provide evidence that the instrumental profile does not vary strongly

Table 4.7: Best-fitting PSFs of the artefact removal with the two-satellite method for two out of six position angles. Three exposures for each angle are listed. PSF-parameters are: distance of the satellites $d_i$, their position angle $\phi_i$ w.r.t. the slit axis, their relative intensities $I_i$, their width $w_i$ and the width of the central component $w_0$.

| exp., PA | $\phi_1$ [°] | $\phi_2$ [°] | $d_1$ | $d_2$ | $I_1$ | $I_2$ | $w_1$ ["] | $w_2$ ["] | $w_0$ ["] | $\mathcal{C}$ | $\mathcal{W}$ |
|---|---|---|---|---|---|---|---|---|---|---|---|
| #1, 0° | 27.4 | -133.5 | 366 | 387 | 0.39 | 0.30 | 0.44 | 0.43 | 0.91 | 5.4 | 7.9 |
| #2, 0° | 31.2 | -130.9 | 361 | 380 | 0.38 | 0.34 | 0.55 | 0.58 | 1.32 | 5.6 | 8.2 |
| #3, 0° | 29.7 | -131.5 | 358 | 382 | 0.41 | 0.36 | 0.54 | 0.52 | 1.28 | 5.8 | 8.1 |
| #1, 90° | 32.6 | -129.1 | 357 | 378 | 0.39 | 0.33 | 0.50 | 0.51 | 0.94 | 5.5 | 7.7 |
| #2, 90° | 30.4 | -131.2 | 359 | 384 | 0.36 | 0.31 | 0.46 | 0.47 | 1.11 | 5.4 | 8.0 |
| #3, 90° | 29.2 | -134.6 | 365 | 389 | 0.43 | 0.29 | 0.47 | 0.47 | 1.43 | 5.9 | 8.3 |

with wavelength. These facts also do not help to clarify why the artefact removal performance is better for the α Cen A data. It could be argued that residual artefacts only appear if the S/N exceeds some specific value. However, this argument does not seem to be plausible.

The corrected $\mathcal{C}(\lambda)$ and $\mathcal{W}(\lambda)$ spectra of all exposures, no matter at which slit orientation, lack any features and are, thus, practically identical to the one depicted in Fig. 4.16 – information on the residuals are also given in Tab. 4.7. Cross-correlation of the spectro-astrometric quantities with the target SED confirm that there is no target signature in the data.

### 4.4.2 Source modelling

As there are no features in the spectro-astrometric quantities at any position angle, only upper limits to spot coverage can be evaluated for α Cen A. Synthetic spectra were used to fit the target SED, cf. Sect. 4.1. As starting point, the known stellar parameters were applied. A good fit quality is achieved with these parameters. The comparison of observed and fitted SEDs is given in Fig. 4.18 for one detector. The differences between the two
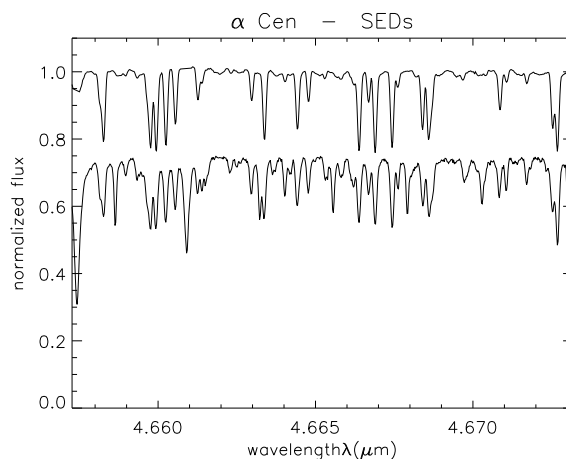


Figure 4.18: The observed SED of α Cen A is depicted by the lower curve, including a few weak telluric lines. The upper curve shows a synthetic model obtained with the stellar parameters of the target.

SEDs is mainly due to telluric lines in the observed SED. Minor differences may result

from differences between the chemical abundances of the model and the true values of the target. Single spot scenarios are then simulated with a temperature contrast that is typical for sun spots, i.e., $\Delta T = 500 \dots 2500\,K$. The sun and $\alpha$ Cen A are of identical spectral type (G2V) and have similar stellar parameters, cf. Sect. 3.1. Hence, spot temperature contrasts are expected to be similar, too. The maximum coverage factors which lead to features in $\mathcal{C}(\lambda)$ and $\mathcal{W}(\lambda)$ which are just below the residual noise amplitude of the data are taken to represent the detection limits. If a single spot is assumed to be at a longitude of zero, i.e., in the middle of the visible disk, and at mid-latitudes, the following results are obtained: a temperature contrast of $\Delta T = 2000\,K$ and a spot size of $e = 16\,\%$ would lead to features at the detection limit of the current data set. A combination of $\Delta T = 1000\,K$ and $e = 29\,\%$ also reaches this limit. If the full S/N-limited spatial resolution of the data could have been reached, the corresponding coverage factors would reduce to $e = 11.5\,\%$ and $e = 21\,\%$, respectively. In addition, spots at lower latitudes, as are common on the sun, are even more difficult to detect as their spectro-astrometric features have smaller amplitudes. If the target indeed behaves similarly as the sun, the non-detection of spots is of no surprise: typical, large sunspot groups do not exceed a coverage factor of about 1%. Thus, spectro-astrometry could only succeed in detecting structures on this particular star if it showed spots much larger than sunspots. Very large spots on solar-like stars have been observed with Doppler imaging, cf. Rice and Strassmeier (2001). However, stars need to be fast rotators to allow for an analysis with the means of Doppler imaging. Fast rotating solar like stars are always very young and, hence, differ significantly from the Sun and $\alpha$ Cen A. This means that a much larger S/N is needed to detect surface features on $\alpha$ Cen A.

If one compares the performance of spectro-astrometry for the two cases of K-band and M-band observations, it is obvious that the method, in practice, works equally well in both wavelength regions.

# Chapter 5

# Summary and outlook

## 5.1 Summary

In this work, it was shown that spectro-astrometry succeeds in attaining spatial resolution at sub-diffraction-limited scales. Theoretically, the resolution limit is placed by the signal-to-noise ratio of the data and the width of the point-spread-function. Observationally, on bright targets, it would be easy to achieve micro-arcsecond resolution if the theoretical limit indeed could be reached. It, however, turned out that instrumental artefacts by far exceed this limit and prevent the detection of structures at these scales. Using the assumption that any instrumental effect can be condensed into an effective PSF, an algorithm was developed to remove these artefacts. Because the instrumental profile has to be described by a two-dimensional PSF, an enormous number of configurations is possible. Thus, an appropriate choice for the parameterisation of the PSF is critical for the success of the removal procedure because of computing time constraints. Although a simple elliptical parameterisation strongly reduces the artefacts, the performance is not sufficient. More complex PSF models like a two-satellite parameterisation proved to achieve a better removal. For the giant star data set, a residual artefact amplitude level of 0.3 mas could be achieved in the position spectrum $\mathcal{C}(\lambda)$. This compares to the S/N-limited value of 0.1 mas and an initial average artefact amplitude of 20 mas. For the data of $\alpha$ Centauri A, the ratio of residual artefact amplitude to theoretical resolution limit is 1.4. In order to reach this level of artefact removal, it is absolutely necessary to consider the width of the spatial profile over wavelength, $\mathcal{W}(\lambda)$, together with the position spectrum $\mathcal{C}(\lambda)$. The width spectrum so far has been ignored in publications on spectro-astrometry. The variations of the instrumental profile with time and wavelength were found to be quite limited. Nevertheless, they are large enough to necessitate an individual removal run for each exposure. The fact that there are residual artefacts significantly above the S/N-limit proves that either the PSF parameterisation was not optimal or that the basic assumption of the removal procedure is not entirely justified (or both). The alternative method of subtracting spectro-astrometric quantities obtained at anti-parallel slit orientations in principle also allows for a removal of instrumental artefacts. However, it was shown that the artefacts strongly vary with time which renders this subtraction method practically useless unless special instrumentation is available, cf. Sect. 5.2.
Since a longslit spectrograph is a 1D-imager, exposures at multiple slit orientations need to be obtained to constrain the physical model of the target. The more slit orientations are probed the better the constraints. The comparison of simulated and observed spectro-astrometric quantities allows to find the underlying source configuration. It was shown that it is important to simultaneously fit $\mathcal{C}(\lambda)$ *and* $\mathcal{W}(\lambda)$ at *all* observed position angles

to reliably deduce the target configuration. The interpretation of the observed $\mathcal{C}(\lambda)$ and $\mathcal{W}(\lambda)$ spectra requires synthetic SEDs of the structures in question. As any uncertainty in the synthetic atmosphere models directly translate into the simulated spectro-astrometric features, the obtained best-fitting source configuration is also affected by those uncertainties. Thus, the better the S/N and overall quality of the observed data, the better the synthetic SEDs need to be in order to exploit the full potential of the data. The two giant stars TW Oph and RS Vir were observed with VLT/CRIRES in the CO first overtone region in the K-band at two independent and orthogonal slit orientations at signal-to-noise ratios of some thousand. In addition, VLT/CRIRES archival data in the fundamental CO region of the solar-like star $\alpha$ Cen A was analyzed for spectro-astrometric signatures. The analysis revealed surface structures on TW Oph. Modelling the signatures with synthetic PHOENIX spectra yielded that a single mid-latitude cool spot with a temperature contrast of 500 K covering 11 % of the visible disk is the most likely interpretation. A single hot spot also is consistent with observations though at a lower significance than a cool spot. Because of the small number of independent slit orientations, there is a set of best-fitting models. Configurations with two or more spots do not fit the data acceptably. The model which was deduced for TW Oph is consistent with previous studies on (super-)giants which have been performed with interferometry or adaptive optics imaging. Upper limits on spot coverage were determined for RS Vir and $\alpha$ Cen A. For RS Vir, the single-spot limit is at a coverage factor of about 10 % for a temperature contrast of 500 K. Spots on $\alpha$ Cen A would need to cover 16 % to 29 % of the visible disk to be detectable with the current data set. This assumes a solar-like temperature contrast of spots of about 2000 K to 750 K, respectively. This means that spots on $\alpha$ Cen A can only be detected by spectro-astrometry if either spots on this star are much larger than on the sun or if the S/N of the data is much higher.

Spectro-astrometry was shown to match the spatial resolutions reached by interferometry, at least for bright targets. The advantage over interferometry is the no special instrumentation is necessary and a single telescope is sufficient.

## 5.2 Outlook

Although spectro-astrometry proved to yield good results, there are still several issues which can be improved during future studies. First of all, a significant improvement of the spatial resolution can be achieved if the instrumental artefacts could be removed completely. To get more information on the instrumental PSF, imaging the 2D-PSF in the slit plane simultaneously with the registration of the longslit spectrum could hint at the general form of the PSF. This would at least record the instrumental influences which take place before the light passes the spectrograph. The usage of a gas absorption cell does not necessarily improve the determination of the instrumental profile for spectro-astrometry. Only if there are no telluric absorption lines and the target is expected to show kinematic spectro-astrometric signatures, gas cell reference lines may lead to better removal results. Current plans to build special instrumentation (Wiedemann, G.; private communications) are expected to solve the problem of instrumental artefacts: if exposures at anti-parallel slit orientations are performed simultaneously and through the same optical path, the removal should become very accurate. Such an instrument will have to split the incoming light, rotate one of the light beams by 180° and disperse both light beams by a single longslit spectrograph. In this way, the full potential of spectro-astrometry could be exploited – however, at the cost of the need for special instrumentation.

To be able to put strong constraints on the best-fitting object configuration, future observations of complex sources should apply as many independent slit orientations as possible.

Observing a target at various wavelength regions also allows confirm or exclude certain underlying source configurations. Furthermore, a more sophisticated approach to modelling the target SEDs with synthetic spectra is necessary. As uncertainties in the synthetic spectra directly translate into an uncertainty in the source geometry, accurate model spectra are required. In particular, very cool giant star atmospheres to date are not yet fully understood.

Observing more objects with shorter integration times (and NDIT=1) will lead to possibly thousands of exposures. As a manual inspection and analysis will virtually be impossible, a better automation of the programmed data reduction and analysis code will be mandatory. Spectro-astrometry will profit in the future from increasing telescope sizes and instrument capabilities. An increasing spatial resolution of a telescope/adaptive optics system directly translates into better spatial resolution in the spectro-astrometric quantities, cf. Eq. (2.6). Furthermore, larger telescopes will increase the S/N on the target which further pushes the attainable spatial resolution.

# Nomenclature

| | |
|---|---|
| (N)LTE | (Non) Local Thermal Equilibrium |
| AGB | Asymptotic Giant Branch |
| APD | Avalanche Photo Diode |
| CADARS | Catalogue of Apparent Diameters and Absolute Radii of Stars |
| CCD | Charge Coupled Device |
| CHARM2 | Catalogue of High Angular Resolution Measurements |
| CMOS | Complementary MetalOxide Semiconductor |
| CPU | Central Processing Unit |
| CRIRES | CRyogenic high-resolution IR Echelle Spectrograph |
| DIT | integration time per exposure |
| ESO | European Southern Observatory; with the full name being "European organization for astronomical research in the southern hemisphere" |
| FITS | Flexible Image Transport System |
| FWHM | Full Width at Half Maximum |
| GAIA | Global Astrometric Interferometer for Astrophysics |
| GPL | General Public License |
| HST/STIS | Hubble Space Telescope / Space Telescope Imaging Spectrograph |
| IRAF | Image Reduction and Analysis Facility |
| ISAAC | Infrared Spectrometer And Array Camera |
| MACAO | Multi-Applications Curvature Adaptive Optics |
| NACO | NAOS-CONICA: Nasmyth Adaptive Optics System – Near-Infrared Imager and Spectrograph |
| NDIT | Number of (DIT-) exposures to be averaged before writing the FITS-file |
| PSF | Point Spread Function |
| RV | Radial Velocity |
| SED | Spectral Energy Distribution |
| SNR, $S/N$ | Signal to Noise Ratio |
| UVES | Ultraviolet and Visual Echelle Spectrograph |
| VLT | Very Large Telescope |

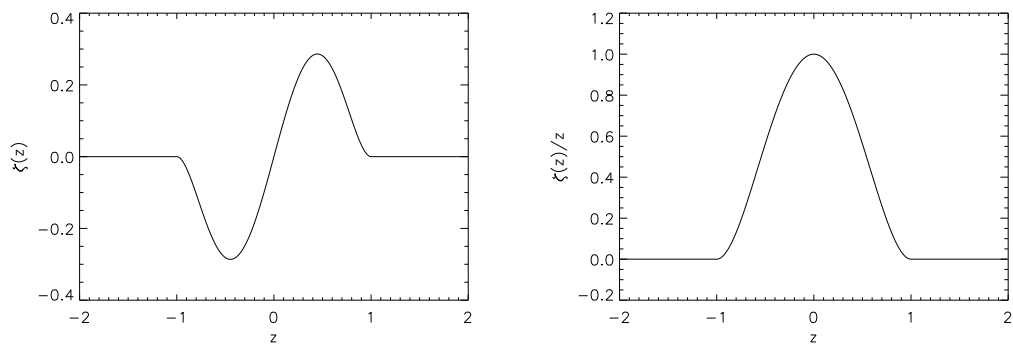# List of Figures

# List of Tables

# Appendix A

# Figures



Figure A.1: The $\zeta$-function (left panel) and the weighting function $\zeta/z$ (right panel) of Tukey's biweight. Here, the cut-off is chosen to be $a = 1$. The weights for $z \geq 1$ are zero. Hence, any data point outside $|z| < 1$ does not contribute at all.
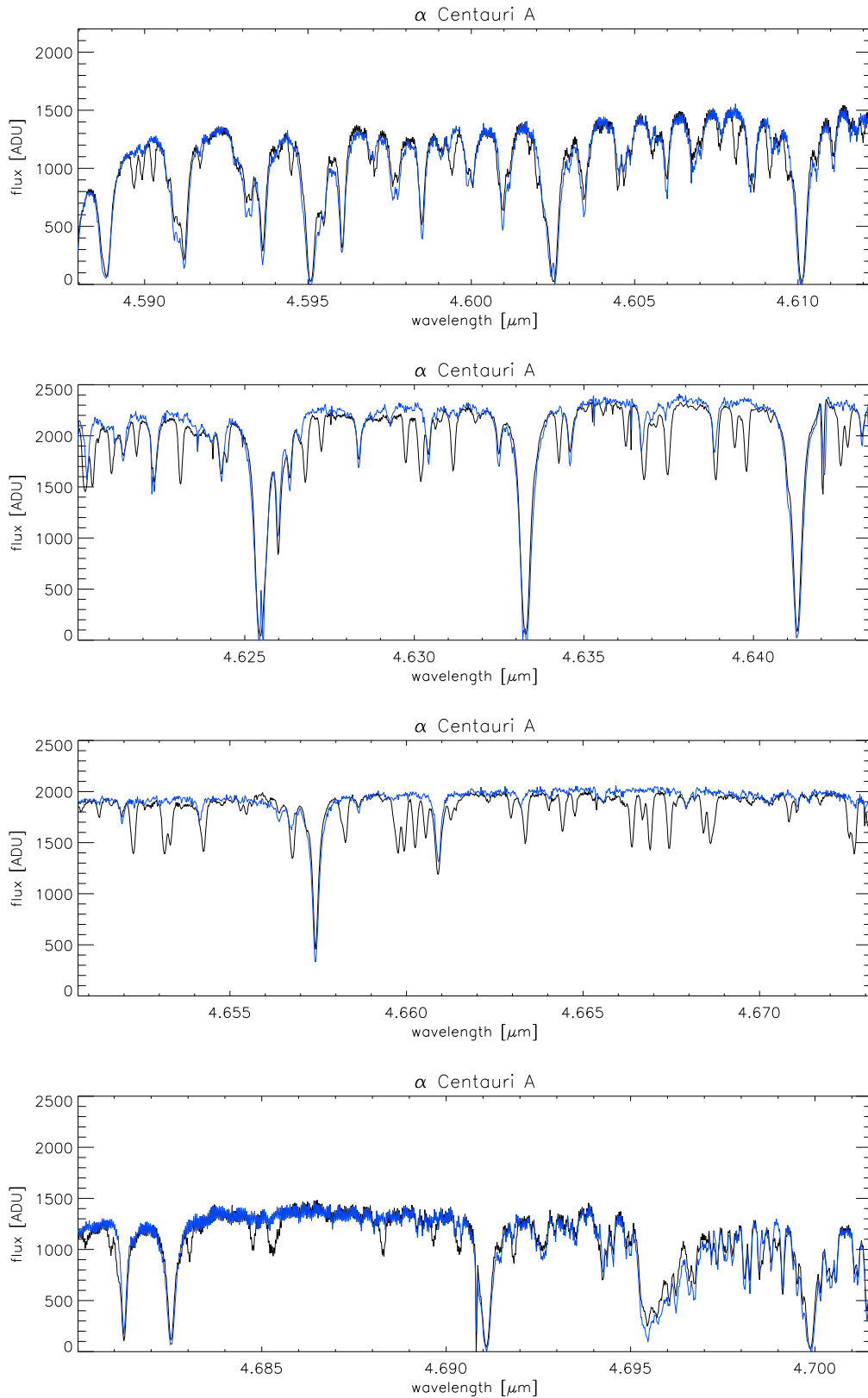
Figure A.2: Spectral energy distribution of $\alpha$ Centauri A in the M-band, detectors one to four of CRIRES. Overplotted is the SED of the telluric standard HR6084.
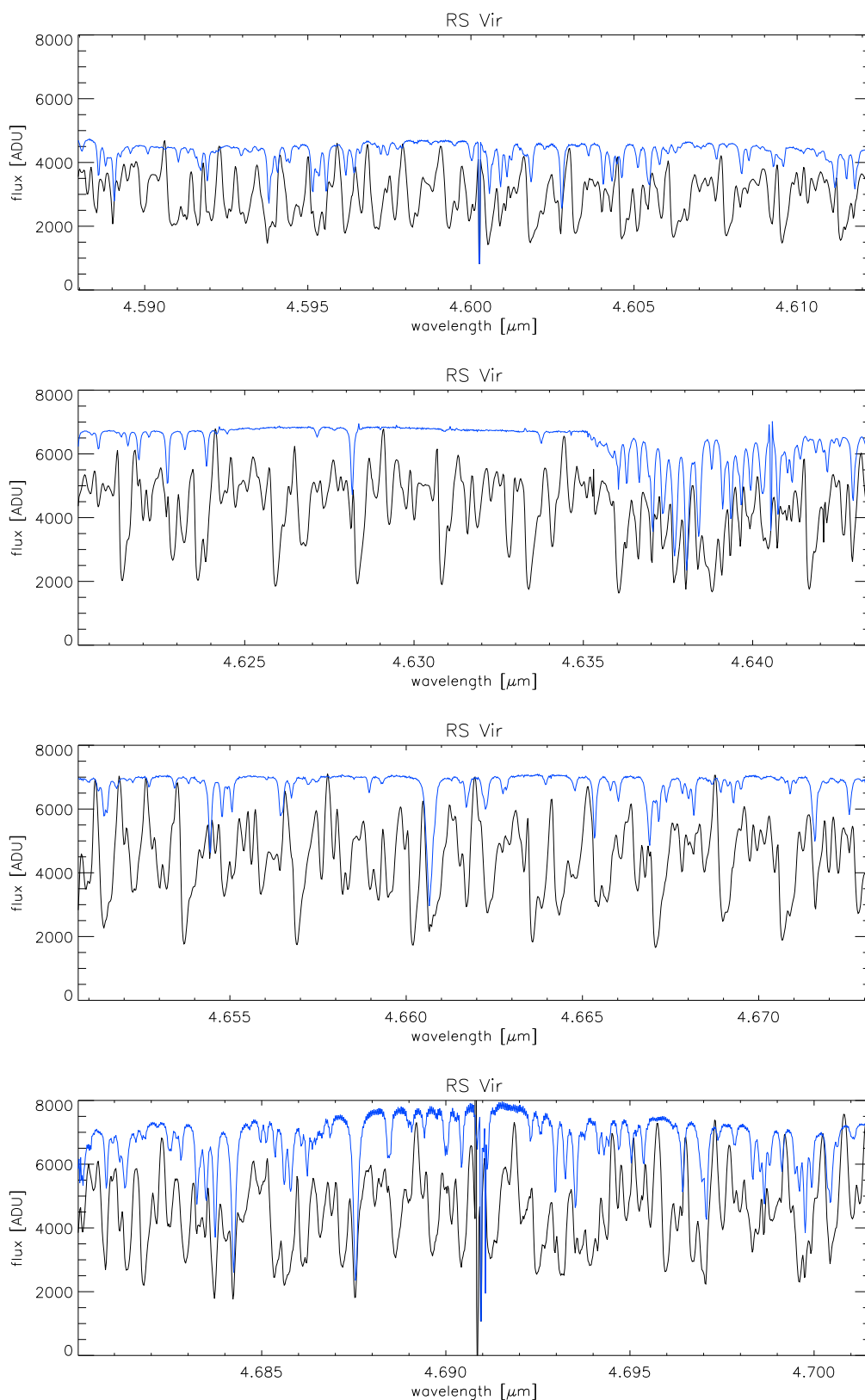
Figure A.3: Spectral energy distribution of RS Vir in the K-band, detectors one to four of CRIRES. Overplotted is the SED of the telluric standard HD121263.
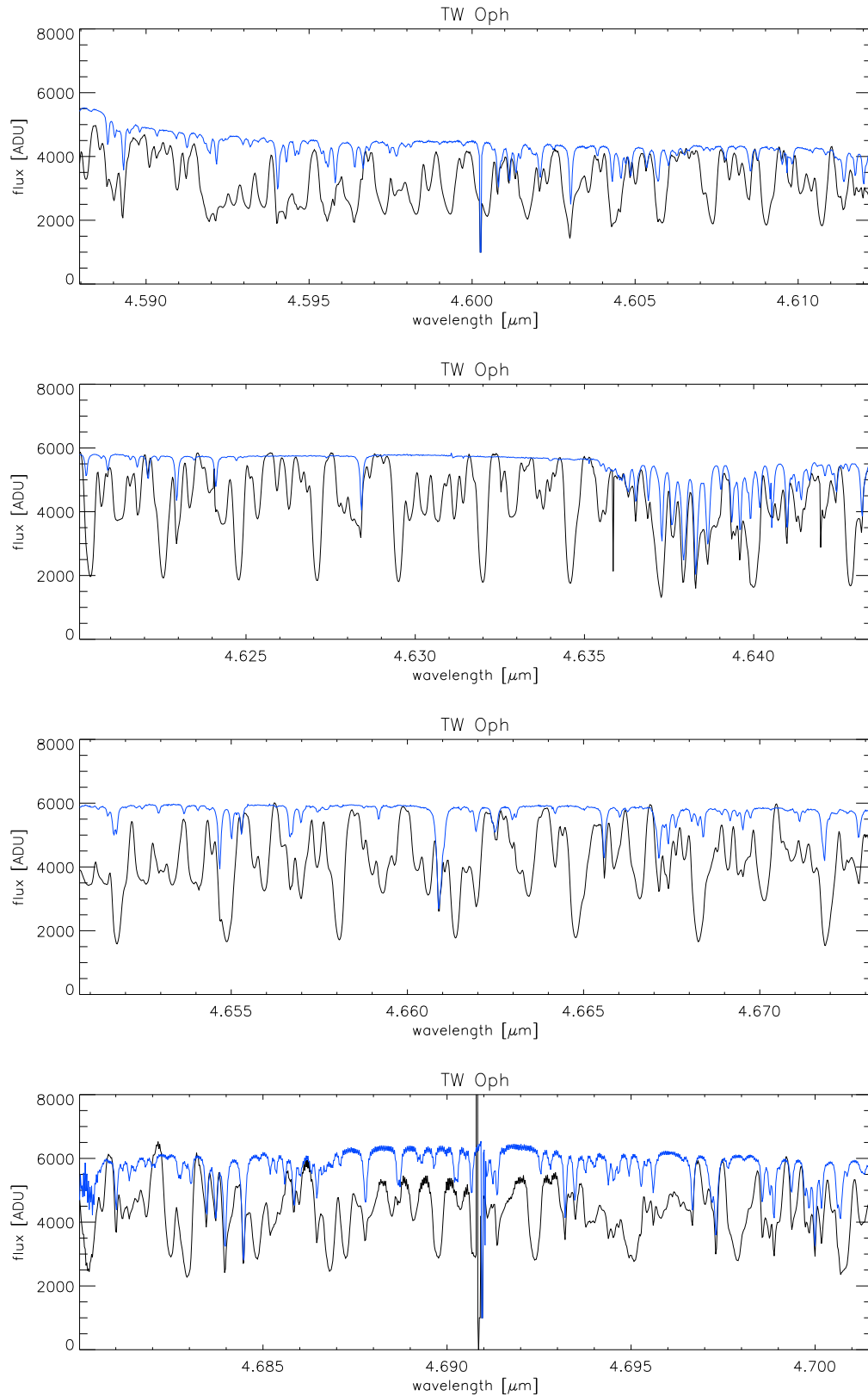
Figure A.4: Spectral energy distribution of TW Oph in the K-band, detectors one to four of CRIRES. Overplotted is the SED of the telluric standard HR173300.

# Appendix B

# Miscellaneous

## B.1  Target candidates

Searching the CHARM2 (Richichi et al., 2005) and the CADARS (Pasinetti Fracassini et al., 2001), cf. Sect. 3.1, catalogues yielded 60 stars with apparent diametre of more than eight milli-arcseconds which are suitable for spectro-astrometry observations. Most of these are M giants and carbon stars. Only a few are K giants and the only maint sequence star is $\alpha$ Centauri. Eighteen objects have apparent diametres of more than $20\,\mathrm{mas}$ and are, thus, primary targets for future spectro-astrometric studies. On these targets, smaller spots and/or spots with lower temperature contrast will be detectable compared to the targets used in this thesis. The current and future status of VLT/CRIRES no longer has the restrictions which prevented observations of the largest stars in the past.

## B.2  Fit algorithms

Here, the fit algorithms used in this work are briefly presented. A full discussion on all techniques and the corresponding algorithms can be found in Press et al. (2002). All methods perform a minimisation of a $\chi^2$ merit function which is defined as

$$\chi^2(\mathbf{a}) = \sum_{i=1}^{N} \left( \frac{y_i - y(x_i; \mathbf{a})}{\sigma_i} \right)^2 \tag{B.1}$$

where

$$y = y(x; \mathbf{a}) \tag{B.2}$$

is the model to be fitted, $y_i$ are the observed data points and $\sigma_i$ are the errors therein. The minimisation yields the best-fitting parameter set $\mathbf{a}$. As the $\chi^2$-measure, here, is only used to determine the best fit and not to quantify whether or not the deviations between a model and observed data are statistically significant at some level, no such significance levels are explicitly stated in this work. Depending on the topology of the N-dimensional space, all methods discussed below may get stuck in a local minimum. For the spectro-astrometric artefact removal and source model fitting, two measures were done to minimise the probability for this problem. First, all $\chi^2$-landscapes, cf. Sect. 2.6.2, were calculated for one exemplary exposure in order to judge how the overall topology looks like. Second, for the same exposure, the algorithm is repeated several times with different starting points.

## B.2.1  Downhill simplex method

The downhill simplex method is an entirely self-contained, purely geometrical strategy of minimisation in multidimensional parameter space. The method does not require derivative evaluations which is advantageous for an application to spectro-astrometric simulations. The efficiency of the downhill simplex is not very good in terms of the number of function evaluations and, hence, computing time. However, it is quite robust and well suited as comparison to the direction set methods which are described in the next section. A *simplex* is defined to be an N-dimensional geometrical figure, thus having $N + 1$ vertices. The algorithm is supplied a starting simplex which can, e.g., be chosen to consist of a starting point $\mathbf{P}_0$ an the $N$ points $\mathbf{P}_i = \mathbf{P}_0 + \lambda \mathbf{e}_i$, with $\mathbf{e}_i$ being the N unit vectors and $\lambda$ being a user-supplied scale length. For each of the $N + 1$ points, the function is evaluated. The downhill simplex then performs one out of several possible steps: reflection, expansion, contraction. In most cases, the algorithm will use the *reflection*, i.e., moving the one point of the simplex with the largest function value through the opposite face of the simplex, conserving the volume of the simplex. This is supposed to lead to a lower value for this specific point. The *expansion* of the simplex in one direction will increase the step size. If a valley floor in the function value space is reached, a *contraction* is performed in the transverse direction in order to move along the valley further downhill.

## B.2.2  Direction set methods

To minimise an N-dimensional function, one can perform a sequence of one-dimensional minimisations. The critical point deciding the effectiveness of a method is how the directions are chosen along which the one-dimensional minimisations are done. All those methods are called *direction set* methods. They are divided into two categories: those which do use gradient information and those which do not. For spectro-astrometric simulations, gradient-independent methods are required. A simple possibility is to chose the unit vectors of the N-space $\mathbf{e}_1, \mathbf{e}_2, \ldots, \mathbf{e}_N$ as the set of directions. However, such a method can be, depending on the topology, be very inefficient as the step size may be very small. Each direction set method has a strategy to identify appropriate directions during the iteration steps to minimise the number of steps needed to find the minimum of the $\chi^2$ function. This work uses *Powell's* method to find those directions. It is described in detail in Press et al. (2002).

## B.2.3  Non-linear model fitting

Now fitting a model is considered for the case that the model depends non-linearly on a set of parameters $a_k, \quad k = 1, 2, 4, \ldots, M$, e.g., fitting a Gaussian to the spatial profile for the extraction of the spectro-astrometric quantities. The best-fitting parameters are determined by minimising the merit function Eq. (B.1). The minimisation procedure needs to be performed iteratively for the non-linear case and an initial starting parameter set needs to be supplied. The basic idea is that the $\chi^2$ function can well be represented by a quadratic form close to the minimum, i.e.,

$$\chi^2(\mathbf{a}) \approx \gamma - \mathbf{d} \cdot \mathbf{a} + 1/2\, \mathbf{a} \cdot \mathbf{D} \cdot \mathbf{a} \tag{B.3}$$

with $\mathbf{d}$ being an M-dimensional vector and $\mathbf{D}$ being an $M \times M$ matrix. If the approximation with a quadratic form were perfect, the minimum $\mathbf{a}_{\mathrm{min}}$ could be reached with

$$\mathbf{a}_{\mathrm{min}} = \mathbf{a}_{\mathrm{cur}} + \mathbf{D}^{-1} \cdot \left( -\nabla \chi^2(\mathbf{a}_{\mathrm{cur}}) \right), \tag{B.4}$$

where $\mathbf{a}_{\mathrm{cur}}$ is the current trial parameter set. As this will not be true, the steepest gradient can be followed downwards iteratively

$$\mathbf{a}_{\mathrm{next}} = \mathbf{a}_{\mathrm{cur}} - \mathrm{C} \cdot \nabla \chi^2(\mathbf{a}_{\mathrm{cur}}), \tag{B.5}$$

where $C$ is a constant specifying the step size. This method needs the gradient of the $\chi^2$ function to be calculable for any parameter as well as the Hessian matrix which is possible as the model itself yields the functional form. The determination of an appropriate value for the step size $C$ is critical and one important aspect of the actual method. One effective and popular one is the *Levenberg-Marquardt* method which is also applied in this work. It extracts information on the choice of the constant from the Hessian matrix, cf. Press et al. (2002) for details.

## B.3 Program code structure

The data reduction was done with IRAF[1]. The standard packages within IRAF were used and combined with appropriate parameter settings to meet the special needs of spectro-astrometry, cf. Chap. 3.
The spectro-astrometric analysis was done exclusively with self-written C-code programs. A detailed description of the different modules is omitted here because it would be quite lengthy and the code is well-documented. Following, only a list is given on the most important modules:

`badprofiles` and `badprofilesexec`
Library and stand-alone executable versions of the badpixel detection/masking and correction algorithm described in Sect. 3.2.1. The executable program takes as input a list of fits-files to be processed and a parameter file. The library version supplies the corresponding procedures for inclusion in any other C-coded program. Here, the input parameters may be passed in the function call or be read from an external file. The program/function outputs the badpixel/badprofile mask and the corrected longslit spectrum.

`SAFittingLib` and `SAFitting`
Library and stand-alone executable versions of the spectro-astrometric extraction algorithm. As input, the program takes a list of fits-files to be processed as well as a parameter file supplying an initial guess on the fit parameters. Optionally, a bad pixel/profile mask may be supplied per fits-file. The code performs the extraction of the position- and width spectra of a longslit spectrum and corrects for the trace, cf. Sects. 3.2.2 and 2.4. Both, the raw and corrected quantities are returned by the program as output.

`simartefactsLib` and `simartefacts`
Library and stand-alone executable versions of the spectro-astrometric core code: here, all spectro-astrometric analysis steps are performed as, e.g., artefact fitting and removal, $\chi^2$-landscape evaluation and source modelling. The most important routine is the one implementing the spectro-astrometric signature simulation itself, using an effective 2D-PSF and a source configuration along with an appropriate number of spectral energy distributions and a velocity field. The code has been parallelised using OpenMP.

---

[1] Image Reduction and Analysis Facility of the National Optical Astronomy Observatory (NOAO)

# Bibliography

Allende Prieto C. and Lambert D.L. (2002). A reappraisal of the solar photospheric C/O ratio. *The Astrophysical Journal*, *573*, L137-L140.

Babcock H.W. (1953). The possibility of compensating astronomical seeing. *PASP*, *65*, 229.

Bailey J. (1998). Detection of pre-main-sequence binaries using spectro-astrometry. *MNRAS*, *301*, 161-167.

Baines D., Oudmaijer R.D., Porter J.M. and Pozzo M. (2006). On the binarity of Herbig Ae/Be stars. *MNRAS*, *367*, 737-753.

Beckers J.M. (1982). Differential speckle interferometry. *OptActa*, *29*, 361-362.

Bergeat and Chevalier. (2005). . *A&A*, *429*, 235.

Böhm-Vitense E. (1992). *Introduction to stellar astrophysics 1-3* (No. ISBN 0-521-34871-4). Cambridge University Press.

Brannigan E., Takami M., Chrysostomou A. and Bailey J. (2006). On the detection of artefacts in spectro-astrometry. *MNRAS*, *367*, 315-322.

Condon J.J. (1997). Errors in Elliptical Gaussian Fits. *PASP*, *109*, 166-172.

Demtröder W. (1999). *Experimentalphysik 2: Elektrizität und Optik* (No. ISBN 3-540-65196-9). Springer.

Demtröder W. (2000). *Experimentalphysik 3: Atome, Moleküle und Festkörper* (No. ISBN 3-540-57096-9). Springer.

Dorch S.B.F. (2004). Magnetic activity in late-type giant stars: Numerical MHD simulations of non-linear dynamo action in Betelgeuse. *Astronomy and Astrophysics*, *423*, 1101-1107.

Eggenberger P., Charbonnel C., Talon S., Meynet G., Maeder A., Carrier F. and Bourban G. (2004). Analysis of $\alpha$ Centauri AB including seismic constraints. *Astronomy and Astrophysics*, *417*, 235-246.

Eglitis I. and Eglite M. (1995). The abundance ratio C/O in the atmospheres of 343 carbon stars. *Astrophysics and Space Science*, *229*, 63-78.

Freytag B., Steffen M. and Dorch B. (2002). Spots on the surface of Betelgeuse - Results from new 3D stellar convection models. *Astronomische Nachrichten*, *323*, 213-219.

Garcia P.J.V., Thiébaut E. and Bacon R. (1999). Spatially resolved spectroscopy of Z Canis Majoris components. *Astronomy and Astrophysics*, *346*, 892-896.

Geballe T.R., Rushton M.T., Eyres S.P.S., Evans A., van Loon J.Th. and Smalley B. (2007). Infrared spectroscopy of carbon monoxide in V838 Mon during 2002-2006. *Astronomy and Astrophysics*, *467*, 269-275.

Gilliland R.L. and Dupree A.K. (1996). First image of the surface of a star with the Hubble Space Telescope. *ApJ*, *463*, L29-L32.

Grave J.M.C. and Kumar M.S.N. (2006). Probing the close environment of massive young stars with spectro-astrometry. *arXiv*, *0612133*.

Hampel F.R., Ronchetti E.M., Rousseeuw P.J. and Stahel W.A. (1986). Robust statistics - The approach based on influence functions. *Wiley*.

Hauschildt P.H. and Baron E. (1999). Numerical solution of the expanding stellar atmosphere problem. *JCAM*, *109*, 41.

Hauschildt P.H. et al. (GAIA). *http://www.hs.uni-hamburg.de/EN/For/ThA/phoenix/index.html*.

Herpin F., Baudry A., Thum C., Morris D. and Wiesemeyer H. (2006). Full polarization study of SiO masers at 86 GHz. *A&A*, *450*, 667.

Høg E., Fabricius C., Makarov V. V., Urban S., Corbin T., Wycoff G., Bastian U., Schwekendiek P. and Wicenec A. . (2000). The Tycho-2 catalogue of the 2.5 million brightest stars. *A&A*, *355*, L27-L30.

Huber P.J. (1981). Robust statistics. *Wiley*.

Kaper H.G., Smits D.W., Schwarz U., Takakubo K. and Van Woerden H. (1966). Computer analysis of observed distributions into Gaussian components. *BAN*, *18*, 465-487.

Lacour S., Meimon, S., Thiébaut et al. (2008). The limb-darkened Arcturus: imaging with the IOTA/IONIC interferometer. *Astronomy and Astrophysics*, *485*, 561-570.

Lambert D.L., Gustafsson B., Eriksson K. and Hinkle K.H. (1986). The chemical composition of carbon stars. I. *The Astrophysical Journal Supplement Series*, *62*, 373-425.

Lançon A., Gallagher J.S., Grijs R., Hauschildt P.H., Ladjal D., Mouhcine M., Smith L.J., Wood P.R. and Förster-Schreiber N. (2007b). Modelling the near-IR spectra of red supergiant-dominated populations. *Stellar populations as building blocks of galaxies, Proceedings IAU Symposium*, *241*.

Lançon A., Hauschildt P.H., Ladjal D. and Mouhcine M. (2007a). Near-IR spectra of red supergiants and giants. *Astronomy and Astrophysics*, *468*, 205-220.

Laverny P. and Mékarnia D. (2004). First detection of dust clouds around R CrB variable stars. *Astronomy and Astrophysics*, *428*, L13-L16.

Law N.M., Mackay C.D. and Baldwin J.E. (2006). Lucky imaging: high angular resolution imaging in the visible from the ground. *Astronomy and Astrophysics*, *446*, 739-745.

Lawrence J.S., Ashley M.C.B., Tokovinin A. and Travouillon T. (2004). Exceptional astronomical seeing conditions above Dome C in Antarctica. *Nature, 431*, 278-281.

Massa D. and Evans N.R. (2008). The angular separation of the components of the Cepheid AW Per. *MNRAS, 383*, 139-149.

Monnier J.D. (2003). Optical interferometry in astronomy. *Rep.Prog.Phys., 66*, 789-857.

Oudmaijer R.D. and Baines D. (2006). Spectro-Astrometry of Herbig Ae/Be Stars. *ASP Conf. Series, 355*.

Oudmaijer R.D., Parr A.M., Baines D. and Porter J.M. (2008). Sub-milliarcsecond precision spectro-astrometry of Be stars. *A&A, 489*, 627-631.

Pasinetti Fracassini, L. E., Pastori, L., Covino, S., & Pozzi, A. (2001, February). Catalogue of Apparent Diameters and Absolute Radii of Stars (CADARS) - Third edition - Comments and statistics. *A&A, 367*, 521-524.

Paufique, J., Biereichel, P., Donaldson, R., Delabre, B., Fedrigo, E., Franza, F., et al. (2004, October). MACAO-CRIRES: a step toward high-resolution spectroscopy. In D. Bonaccini Calia, B. L. Ellerbroek, & R. Ragazzoni (Eds.), *Society of photo-optical instrumentation engineers (spie) conference series* (Vol. 5490, p. 216-227).

Perryman et al. (1997). (Hipparcos). *A&A, 323*, L49.

Pontoppidan K.M., Blake G.A., VanDishoeck E.F., Smette A., Ireland M.J. and Brown J. (2008). Spectro-astrometric imaging of molecular gas within protoplanetary disk gaps. *ApJ, 684*, 1323-1329.

Porter J.M., Oudmaijer R.D. and Baines D. (2004). On the spectroastrometric separation of binary point-source fluxes. *Astronomy and Astrophysics, 428*, 327-337.

Porter J.M., Oudmaijer R.D. and Baines D. (2005). Spectroastrometry: a new method for direct determination of disc kinematics. *ASP Conf. Series, 337*.

Press W.H., Teukolsky S.A., Vetterling W.T. and Flannery B.P. (2002). Numerical recipes in C. The art of scientific computing. *Cambridge: University Press, 1992, 2nd ed.*

Ragland S., Traub W.A., Berger J.-P. et al. (2006). First surface-resolved results with the infrared optical telescope array imaging interferometer: detection of asymmetries in asymptotic giant branch stars. *ApJ, 652*, 650-660.

Rice J.B. and Strassmeier K.G. (2001). Doppler imaging of stellar surface structure. XVII. The solar-type Pleiades star HII314. *Astronomy and Astrophysics, 377*, 264-272.

Richichi A. (1989). Model-independent retrieval of brightness profiles from lunar occultation lightcurves in the near infrared domain. *A&A, 226*, 366-372.

Richichi A., Fors O., Mason E., Delbo M., Stegmaier J. and Finger G. (2007). Life on the fast lane: the burst mode at the VLT at present and in the future. *arXiv:0712.1179*.

Richichi et al. (2005). (CHARM2). *A&A, 431*, 773.

Rousseeuw P.J. and Croux C. (1993). Alternatives to the Median Absolute Deviation. *Journal of the American Statistical Association*, *88*, 1273-1283.

Rousseeuw P.J. and Leroy A.M. (1987). Robust regression and outlier detection. *Wiley*.

Schwarzschild M. (1975). On the scale of photospheric convection in red giants and supergiants. *Astrophysical Journal*, *195*, 137-144.

Seifahrt A. and Käufl H.U. (2008). High precision radial velocity measurements in the infrared. *arXiv*, *0809*, 1435.

Shack R.B. and Platt B.C. (1971). Production and use of a lenticular Hartmann screen. *JOSA*, *61*, 656.

Siebenmorgen R. and Smette A. (2008). ESO VLT/CRIRES User Manual. *VLT-MAN-ESO-14500-3486*, *83.2*.

Sloan G.C., Little-Marenin I.R. and Price S.D. (1998). The carbon-rich dust sequence - Infrared spectral classification of carbon stars. *AJ*, *115*, 809-820.

Stone H.S., Orchard M.T., Chang E.-C. and Martucci S.A. (2001). A fast direct Fourier-based algorithm for subpixel registration of images. *IEEE Transactions on geoscience and remote sensing*, *39*(10), 2235-2243.

Takami M., Bailey J. and Chrysostomou A. (2003). A spectro-astrometric study of southern pre-main sequence stars. *Astronomy and Astrophysics*, *397*, 675-691.

Takami M., Bailey J., Gledhill T.M., Chrysostomou A. and Hough J.H. (2001). Circumstellar structure of RU Lupi down to AU scales. *MNRAS*, *323*, 177-187.

Takami M., Chrysostomou A., Bailey J., Gledhill T.M., Tamura M. and Terada H. (2002). HeI 1.083um emission and absorption in DG Tauri: line excitations in the jet, hot wind, and accretion flow. *ApJ*, *568*, L53-L56.

Thompson A.R., Moran J.M. and Swenson G.W. (2001). *Interferometry and synthesis in radio astronomy* (Thompson A.R., Ed.) (No. ISBN: 047154924). New York: Wiley.

van Belle G.T., Thompson R.R. and Creech-Eakman M.J. (2002). Angular Size Measurements of Mira Variable Stars at 2.2 Microns. II. *AJ*, *124*, 1706-1715.

Whelan E.T., Ray T.P. and Davis C.J. (2004). Paschen beta emission as a tracer of outflow activity from T-Tauri stars, as compared to optical forbidden emission. *Astronomy and Astrophysics*, *417*, 247-261.

Whelan E.T., Ray T.P., Bacciotti F. and Jayawardhana R. (2006). Probing outflow activity in very low mass stars and brown dwarfs. *New Astronomy Reviews*, *49*, 582-589.

Whelan E.T., Ray T.P., Bacciotti F., Natta A., Testi L. and Randich S. (2005). A resolved outflow of matter from a brown dwarf. *Nature*, *435*, 652-654.

Young J.S., Baldwin J.E., Boysen R.C. et al. (2000). New views of Betelgeuse: multi-wavelength surface imaging and implications for models of hotspot generation. *MNRAS*, *315*, 635-645.

# Acknowledgments

The support of several people helped me during the time of my PhD and made the completion of this thesis possible. It is a pleasure for me to thank these people:

- Prof. Dr. Günter Wiedemann for the possibility to do this work, for the fascinating topic of the thesis and for his advice

- Dr. Bringfried Stecklum for being the second referee

- Prof. Dr. Jürgen Schmitt and Prof. Dr. Peter Hauschildt for being the referees of the disputation

- Soeren Witte and Dr. Andreas Schweitzer for their advice on theoretical and practical aspects of synthetic atmosphere models and for the supply with PHOENIX spectra

- Dr. Rainer Wichmann for solving any computer-related problem

- All my office mates (Lars Buntemeyer, Dennis Jack, Anna-Lea Lesage, Marco Mittag, Magnus Schneide, Andreas Seelmann, Ulfert Wiesendahl) for making everyday-office-life as comfortable as it was; Ulfert Wiesendahl for sharing his IDL knowledge

- All people at the administration for their help and friendliness

- My family for their support throughout the time of my studies

- My wife Lisa for everything